TRANSVERSE MODES IN PORRO PRISM RESONATORS

by

LIESL BURGER

Supervisor:

Dr. Andrew Forbes

December 2008

Submitted in fulfillment of the academic requirements for the degree of Master of Science in the School of Physics, University of KwaZulu-Natal, Durban.

ABSTRACT

This dissertation consists of two main sections. The first is a review of laser resonators using spherical mirrors, and incorporates a physical optics numerical model of a Fabry-Perot laser resonator without gain. The output of this model, which includes spot sizes, loss, and transverse mode formation, is compared to the parameters calculated using published analytical results. This comparison serves as a verification of the numerical methods used, as well as a frame of reference for the model of a Porro prism resonator which follows in the second section.

The second section proposes a new method for analysing Porro prism resonators. The analysis incorporates both geometric as well as physical optics concepts, with the prisms modelled as rotating elements with amplitude and phase distortions. This yields expressions for the orientation of the loss at the apex of each prism, and as well as the number of petals in the "petal-pattern" beam structure commonly observed from Porro prism lasers. These expressions are included in a numerical model, which is first used to verify the development of the characteristic petal-pattern. Next, the numerical model is used to investigate the development of the beam structure, in both time and space, in crossed Porro resonators with a range of Fresnel numbers and stability parameters. This leads to some new insight into the transverse modes of these lasers.

PREFACE

The experimental work described in this dissertation was carried out at the CSIR National Laser Centre (Pretoria), while I was enrolled at the School of Physics, University of KwaZulu-Natal (Durban), from January 2007 to November 2008, under the supervision of Dr. Andrew Forbes.

These studies represent original work by the author and have not been submitted in any form for any degree or diploma to any tertiary institution. Where use has been made of the work of others it is duly acknowledged in the text.

Signed: …….

On this ……... day of …….. 2009

DECLARATION 1 – PLAGIARISM

I, **Liesl Burger** declare that

1. The research reported in this dissertation, except where otherwise indicated, is my original research.
2. This dissertation has not been submitted for any degree or examination at any other university.
3. This dissertation does not contain other persons' data, pictures, graphs or other information, unless specifically acknowledged as being sourced from other persons.
4. This dissertation does not contain other persons' writing, unless specifically acknowledged as being sourced from other researchers. Where other written sources have been quoted, then:
    a. Their words have been re-written but the general information attributed to them has been referenced.
    b. Where their exact words have been used, then their writing has been placed in italics and inside quotation marks, and referenced.

    This dissertation does not contain text, graphics or tables copied and pasted from the Internet, unless specifically acknowledged, and the source being detailed in the dissertation and in the References section.

Signed: _____

DECLARATION 2 – PUBLICATIONS

Peer-reviewed journal papers

Litvin, I.A., **Burger, L.** & Forbes, A. (2007) Petal–like modes in Porro prism resonators. *Optics Express* 15 (21) p. 14065-14077

Burger, L. & Forbes, A. (2008) Kaleidoscope modes in large aperture Porro prism resonators. *Optics Express* 16 (17) p. 12707-12714 (* Front cover of Journal)

Burger, L. Litvin, I.A. & Forbes, A. (2008) Simulating atmospheric turbulence using a phase–only spatial light modulator. *South African Journal of Science* 104(2) p. 129-134 (* Front cover of Journal)

International conference papers

Forbes, A., **Burger, L.** (2006) Modeling laser brightness from cross Porro prism resonators. *Proceedings of SPIE* 6290 p. 62900M-1

Litvin, I.A., **Burger, L.**, Forbes, A. (2007) Analysis of transverse field distribution in Porro prism resonators. *Proceedings of SPIE* 6346 p. 63462G-1

Burger, L. & Forbes, A. (2007) A model of the transverse modes of stable and unstable Porro prism resonators using symmetry considerations. *Proceedings of SPIE* 6663 p. 666305-1

Litvin, I.A., **Burger, L.**, De Gama, M.P., Mathye, A. & Forbes, A. (2007) Laser beam shaping limitations for laboratory simulation of turbulence using a phase-only spatial light modulator. *Proceedings of SPIE* 6663 p. 66630R-1

Burger, L. & Forbes, A. (2008) Porro prism lasers: a new perspective. *Proceedings of SPIE* 7070 p. 70700L-1

National conference papers

Burger, L. & Forbes, A. (2007) A numerical model of a simple Porro prism resonator. *52nd Annual Conference of the South African Institute of Physics 2007, University of the Witwatersrand, Johannesburg, South Africa*

Burger, L. & Forbes, A. (2008) Porro Prism Lasers: A new perspective. *53rd Annual Conference of the South African Institute of Physics 2008, University of Limpopo, Polokwane, South Africa*

Signed: _____

CONTENTS

LIST OF FIGURES

LIST OF TABLES

AKNOWLEDGMENTS

I would like to express my gratitude to:

- my supervisor, Dr. Andrew Forbes, for your belief in my abilities and endless encouragement, for your expert direction and for your enthusiasm for both my work and optics in South Africa.
- my colleague Igor Litvin, for your valuable contributions to the team in the early stages of the Porro resonator project.
- the National Laser Centre for the financial support that made my MSc possible, and for allowing me to present my work at SPIE 2007 and SPIE 2008 in the USA.
- Dr. Ted Roberts, for patiently proof-reading, and for useful suggestions.
- my mum, Margaret Haines, a woman of intelligence and determination, for your love, support and encouragement, and for the example you have set throughout my life.
- my children, Paul and Disa, for your love and encouragement, and for understanding that mum sometimes also has homework.
- my husband, Herman, from whom I learned that I can reach my goals in the face of opposition.

LIST OF SYMBOLS

Symbol	Meaning
L	optical resonator length
λ	laser wavelength in a vacuum
R, R_1, R_2	mirror radius of curvature
f, f_1, f_2	lens focal length
g_1, g_2	g-parameters
G_1, G_2	equivalent G-parameters
N_F	effective Fresnel number
a	limiting aperture radius
ω_0	Gaussian laser beam waist radius
ω_1, ω_2	Gaussian laser beam radius on mirror 1 and mirror 2
$\omega(z)$	laser beam radius at position z, calculated using the second-moment method
$R(z)$	wavefront radius of curvature
z_R	Rayleigh range
θ	half-angle divergence
M	ray-transfer matrix of a resonator
M_{mir}	ray-transfer matrix of Fabry-Perot resonator
M_{lens}	ray-transfer matrix of resonator containing lenses
$\underline{u}_0$	initial ray vector
$\underline{u}_p$	ray vector after p round trips through the resonator
λ_1, λ_2	eigenvalues
$\underline{v}_1, \underline{v}_2$	eigenvectors
β_1, β_2	eigenvalues coefficients of expansion

P	periodicity
P_{tot}	Total power
$I(r)$, $I(x,y)$	Intensity distribution
W_x, W_y	Second-moment laser beam radius
M^2	Beam quality factor
T, T_{00}, T_{nm}	Transmission factors
V	round-trip loss factor
α	Porro angle
β	misalignment angle
D/D_0	relative optical axis shift
R_{eff}	effective reflectivity in a Porro resonator
$t(x,y)$	transfer function
$\theta_1(n)$, $\theta_2(n)$	rotation of ray after n reflections
$\phi_1(n)$, $\phi_2(n)$	ray orientation angle after n reflections
N	number of beam sub-divisions or petals

1. INTRODUCTION

The theory of the stimulated emission of radiation from atoms and molecules, as opposed to spontaneous emission, was proposed in 1917 by Albert Einstein. In 1958 the principles of amplification of light were published by Arthur L. Schawlow and Charles H. Townes, and contained the idea of arranging mirrors at each end of a cavity containing a substance that could be excited to emit light, the gain medium. The mirrors would bounce the light back and forth so that all the photons would be moving in the same direction. The first laser, an acronym for Light Amplification by the Stimulated Emission of Radiation, was built in 1960 by Theodore Maiman of the Hughes Aircraft Company (*Friedman* 2000). It consisted of a flashlamp-pumped ruby crystal, with the ends of the crystal silvered to serve as the mirrors of the first laser resonator. Since then lasers have proven to be a powerful tool with a broad range of applications from barcode scanners to nuclear fusion. Their usefulness stems from their ability to generate very high radiation density at remote distances with high precision.

The simplest type of resonator, the planar Fabry-Perot resonator, consists of two plane parallel mirrors separated by some distance. It is extremely difficult to trap light in this way; if the mirrors are not perfectly parallel then a beam of light between them will tend to “walk off” the mirrors and escape at the edges. One way to contain light between two mirrors is to put curvature on one or both mirrors, which, within certain limits (which will be discussed), causes light to be reflected towards the optical axis. This relaxes the alignment tolerances sufficiently to allow lasers to be constructed using even low-gain media, which require a beam to make many round trips through the gain medium in a resonator.

Another approach to dealing with the problem of beam walk-off is to replace the end mirrors of a resonator with Porro prisms, named after the Italian Ignazio Porro, who invented them in 1850. Porro prisms are right-angled prisms, and reflect a ray back parallel to its initial direction even when the Porro prism is misaligned. This property has been shown to be very useful in the design of lasers intended for field use, or in environments where re-alignment is impractical. One exotic example is a Porro prism laser that was an integral component of the MOLA laser altimeter which was sent on an unmanned mission to Mars in 1992. Porro prism lasers have also been used extensively for over 30 years in ranging and target designation systems, primarily for the military.

Previously the Porro prisms making up a Porro prism resonator have been treated as plane mirrors, albeit by taking into account the effects of Porro prisms on the polarisation of light.

This accounts for some of their characteristics, for example that the amount of light coupled out of the resonator can be optimised by changing the azimuthal angle between the prisms, but this approach does not explain the characteristic beam structure which is evident in the laboratory. What is typically observed is that as the azimuthal angle is varied the beam structure changes, having the appearance of a circular pattern of areas of high intensity with low intensity between them at some angles, and a flatter intensity profile with a low intensity area in the centre at other angles. This is illustrated in Figure 1 by images of beams from a Nd:YAG Porro prism laser captured on a CCD camera in the laboratory.

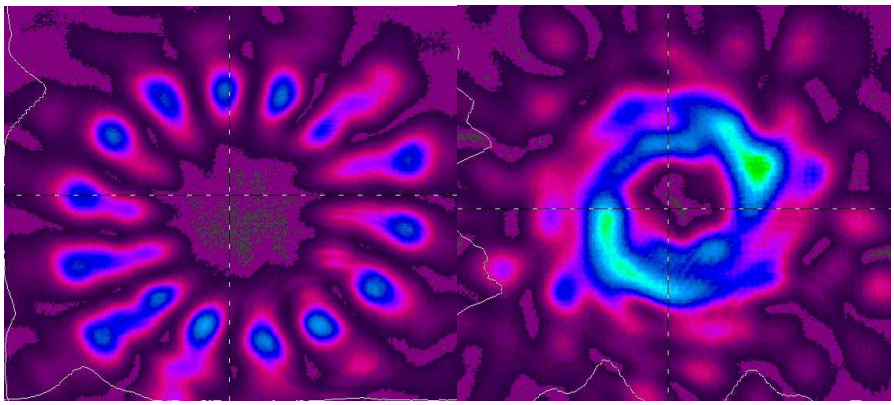

Figure 1 Typical beam intensity distributions from an Nd:YAG Porro prism laser.

The aim of this dissertation is to attempt to explain the beam patterns obtained from Porro prism resonators by means of an analysis of the field in this kind of resonator, and then to verify this by means of a numerical model as well as by experiment.

This dissertation is divided into the following chapters: Preliminary work consists of a review of fundamental laser theory in the balance of Chapter 1. A numerical model of Fabry-Perot resonators is presented in Chapter 2, the results of which are compared to theoretical predictions and is used to validate the modelling methods used. A review of literature on Porro prism lasers is presented in Chapter 3, followed by a discussion of the properties of these systems. Our research is presented in Chapter 4, which includes an analytical and numerical model of a Porro prism resonator which for the first time predicts the beam mode structure produced by these resonators. The beam modes predicted by this model are verified experimentally. The conclusions and suggestions for further work are in Chapter 5.

1.1 Review of relevant theory

Laser beam and resonator theory is covered in numerous excellent textbooks. A comprehensive review article (*Kogelnik & Li* 1966), as well as two textbooks (*Siegman* 1986; *Hodgson & Weber* 2005) were referred to in this section. All other references are noted.

The basic properties of resonators are determined from the first-order properties of the system using ray transfer matrix analysis, which is a purely geometrical approach; although the ray matrix approach can be extended to describe a general optical beam (*Belanger* 1991).

A paraxial ray of an optical system is characterized by its distance x from the optic (z) axis and by its slope x' with respect to that axis. The slope x' is assumed to be small. The path of the ray through a given optical component depends on the optical properties of the component as well as on the input conditions. For paraxial rays the output quantities x_1 and x_1' are linearly dependent on the input quantities (x_0, x_0'), represented in matrix form by:

$$\begin{bmatrix} x_1 \\ x_1' \end{bmatrix} = \begin{bmatrix} A & B \\ C & D \end{bmatrix} \begin{bmatrix} x_0 \\ x_0' \end{bmatrix} \tag{1-1}$$

where the matrix $\begin{bmatrix} A & B \\ C & D \end{bmatrix}$ is the ray transfer matrix of the optical component.

Table 1 gives the ray transfer matrices of a few optical components.

Table 1 The Ray Transfer Matrices of three elementary optical structures in air.

Optical component	**Ray Transfer Matrix**
a homogeneous medium of length d	$\begin{pmatrix} 1 & d \\ 0 & 1 \end{pmatrix}$
a thin lens, focal length f	$\begin{pmatrix} 1 & 0 \\ -1/f & 1 \end{pmatrix}$
a spherical mirror, radius of curvature R	$\begin{pmatrix} 1 & 0 \\ -2/R & 1 \end{pmatrix}$

A sequence of optical components can be handled in the following manner:

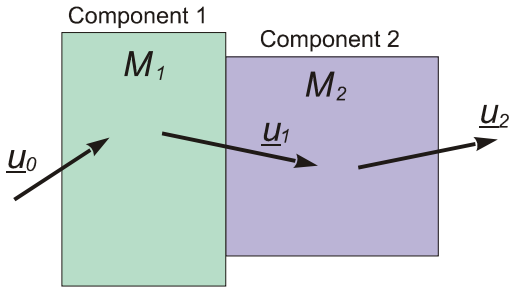

Figure 2 Diagram of a ray passing through a sequence of optical components.

Suppose an input ray $\underline{r}_0$ passes through two optical components with ray transfer matrices M_1 and M_2 respectively, as shown in Figure 2. The first component transforms $\underline{r}_0$ as:

$$\underline{r}_1 = M_1 \underline{r}_0 . \tag{1-2}$$

$\underline{r}_1$ is now the input ray to the second component and gets transformed as:

$$\underline{r}_2 = M_2 \underline{r}_1 = M_2 M_1 \underline{r}_0 .$$

In general, the ray transfer matrix of a ray passing through n optical components is given by:

$$M = M_n M_{n-1} ... M_3 M_2 M_1 \tag{1-3}$$

If $M = \begin{bmatrix} A & B \\ C & D \end{bmatrix}$ is the transformation matrix of a resonator, and $\underline{r}_0$ is any first-order ray with position y and slope y': $\underline{r}_0 = \begin{bmatrix} y \\ y' \end{bmatrix}$.

After one round trip through the resonator the ray is transformed as

$$\underline{r} = M \underline{r}_0 \tag{1-4}$$

After p passes through the resonator the final ray can be found from:

$$\underline{r}_p = M^p \underline{r}_0 . \tag{1-5}$$

This can be simplified using an eigenfunction analysis:

Eigenvectors $\underline{v}_1$ and $\underline{v}_2$ exist which form a complete, orthogonal set, so coefficients of expansion β_1 and β_2 can be found such that any initial ray $\underline{r}_0$ can be expressed in terms of the eigenvectors:

$$\underline{r}_0 = \beta_1 \underline{v}_1 + \beta_2 \underline{v}_2 \tag{1-6}$$

so $$\underline{r}_p = \beta_1 \lambda_1{}^p \underline{v}_1 + \beta_2 \lambda_2{}^p \underline{v}_2 . \quad (1\text{-}7)$$

Scalar eigenvalues λ_i can be found which satisfy the eigenequation:

$$M\underline{r} = \lambda \underline{r} \quad (1\text{-}8)$$

or $$M - I\lambda = 0 . \quad (1\text{-}9)$$

A non-trivial solution (for eigenvectors $\underline{v} \neq 0$) only exists if $\det(M - I\lambda) = 0$

or $$\begin{vmatrix} A-\lambda & B \\ C & D-\lambda \end{vmatrix} = 0$$

which using AD – BC = 1 (assuming $n_2/n_1 = 1$) gives the quadratic equation:

$$\lambda^2 - (A+D)\lambda + 1 = 0 . \quad (1\text{-}10)$$

Letting $$m = \frac{A+D}{2} , \quad (1\text{-}11)$$

we get eigenvalues $$\lambda_{1,2} = m \pm \sqrt{m^2 - 1} . \quad (1\text{-}12)$$

Values of $|m| \leq 1$ give $|\lambda| \leq 1$, which by (1-12) means that $\underline{r}$ remains bounded for all p. Therefore a paraxial ray in a resonator will be periodically refocused, and the resonator is stable. This stability condition can be written as

$$-1 < \tfrac{1}{2}(A+D) < 1. \quad (1\text{-}13)$$

For a stable resonator (1-12) can be rewritten as

$$\lambda_{1,2} = m \pm i\sqrt{1-m^2} , \quad (1\text{-}14)$$

and in this case $\lambda_{1,2}$ is a complex number with multiple cyclic solutions, so:

letting $m = \cos\theta$, $$\lambda_{1,2} = \cos\theta \pm i \sin\theta = e^{\pm i\theta} . \quad (1\text{-}15)$$

By (1-7) this implies that any ray $\underline{r}_p$ will exhibit oscillatory behaviour.

The eigenvectors can be found by forming the modal matrix

$$adj[M - I\lambda]_{\lambda_1,\lambda_2} = \begin{vmatrix} D-\lambda_1 & -B \\ -C & A-\lambda_2 \end{vmatrix}$$

so $$\underline{v}_1 = \begin{pmatrix} D-\lambda_1 \\ -C \end{pmatrix} \text{ and } \underline{v}_2 = \begin{pmatrix} -B \\ A-\lambda_2 \end{pmatrix}. \quad (1\text{-}16)$$

After a sufficient number of passes p through a resonator the term with the largest eigenvalue will dominate, and

$$\underline{r}_p \rightarrow \beta_j \lambda_j{}^p \underline{v}_j \text{ as } p \rightarrow \infty \quad (1\text{-}17)$$

where λ_j is the larger of eigenvalues λ_1 and λ_2.

A real resonator will always contain a limiting aperture of radius a, which might be the laser rod, a cavity mirror, or an iris placed in the resonator. The limiting aperture radius a is another important parameter of a resonator because it defines the transverse extent available to the laser beam.

The laser beam that emerges from a resonator can be characterized by its mode, or the distribution of intensity in a plane at a point along its path, and is given as some function $I(x, y)$. The total power in a continuous beam can be calculated from:

$$P_{tot} = \int_{-\infty}^{\infty} \int_{-\infty}^{\infty} I(x,y)\,dx\,dy\,. \quad (1\text{-}18)$$

A normalised beam is defined as one with unit power, or

$$P_{norm} = \int_{-\infty}^{\infty} \int_{-\infty}^{\infty} I(x,y)\,dx\,dy = 1\,. \quad (1\text{-}19)$$

A propagating laser beam which encounters an aperture of radius a will be clipped, and the laser power P_a transmitted through the aperture can be calculated:

$$P_a = \int_{r=0}^{a} \int_{\theta=0}^{2\pi} I(r)\,r\,dr\,d\theta \quad (1\text{-}20)$$

and the fraction of laser power transmitted T can be found from:

$$T = \frac{P_a}{P_{tot}}\,. \quad (1\text{-}21)$$

A related parameter useful in estimating the output power from a laser is the round-trip diffraction loss, *V*, defined as:

$$V = 1 - \frac{P_1}{P_0} \tag{1-22}$$

where P_0 is the initial power, and P_1 is the power remaining after one complete round trip through a resonator.

The simplest laser resonator is the Fabry-Perot resonator, which comprises two mirrors with spherical curvatures of radius R_1 and R_2 respectively, separated by some distance *L*, as shown in Figure 3. Typically one mirror reflects 100% of the incident light, and the other is partially reflecting, allowing a certain percentage of the laser beam to be coupled out of the resonator as the useful beam.

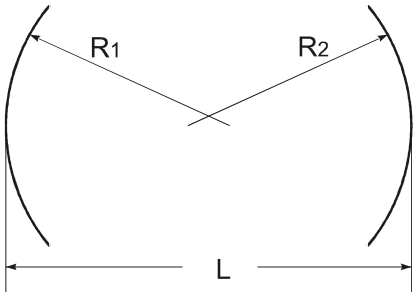

Figure 3 Fabry-Perot resonator with spherical mirrors.

For the Fabry-Perot resonator illustrated in Figure 3 the ray transfer matrix is:

$$M_{mir} = \begin{pmatrix} A & B \\ C & D \end{pmatrix} = \begin{pmatrix} 1 & 0 \\ -2/R_2 & 1 \end{pmatrix}\begin{pmatrix} 1 & L \\ 0 & 1 \end{pmatrix}\begin{pmatrix} 1 & 0 \\ -2/R_1 & 1 \end{pmatrix}\begin{pmatrix} 1 & L \\ 0 & 1 \end{pmatrix}$$

$$= \begin{pmatrix} 1-\dfrac{2L}{R_1} & 2L\left(1-\dfrac{L}{R_1}\right) \\ \dfrac{-2(R_1+R_2-2L)}{R_1R_2} & 1+\dfrac{2L}{R_1}\left(\dfrac{2L}{R_2}-1\right)-\dfrac{4L}{R_2} \end{pmatrix}. \tag{1-23}$$

From (1-13) this leads to the stability condition for a Fabry-Perot resonator:

$$0 < \left(1-\frac{L}{R_1}\right)\left(1-\frac{L}{R_2}\right) < 1 \tag{1-24}$$

Defining the stability parameters g_1 and g_2 to be:

$$g_1 = 1 - \frac{L}{R_1} \text{ and } g_2 = 1 - \frac{L}{R_2}, \tag{1-25}$$

then a resonator is stable if

$$0 < g_1 g_2 < 1. \tag{1-26}$$

For a resonator with no apertures the equivalent G-parameter is defined:

$$G \equiv 2 g_1 g_2 - 1 \tag{1-27}$$

and is the first of the two fundamental parameters of a generalised resonator used to characterize and compare resonators.

Because of the symmetry of any mirror-aperture or lens-aperture configuration, the second important parameter of generalized resonators is the effective Fresnel number, defined as:

$$N_F = \frac{a^2}{\lambda L}, \tag{1-28}$$

and is determined by the propagation distance from one encounter of the limiting aperture to the next (L), as well as the limiting aperture radius a. Resonators with the same Fresnel number and wavelength will have equivalent diffraction properties because the ratio of cross-sectional area to length is the same.

This implies that the resonator configurations in Table 2 are equivalent, because G and N_F are identical for each.

Table 2 Three equivalent resonators. Note that for all three the G-values, as well as the N_F values, are identical.

Parameter	**Units**	**Resonator 1**	**Resonator 2**	**Resonator 3**
λ	μm	1.064	1.064	1.064
L	cm	10	20	100
R	cm	40	80	400
G	-	0.75	0.75	0.75
a	cm	0.045 257	0.064 002	0.143 114
N_F	-	1.924 95	1.924 95	1.924 95

Because the ray transfer matrix of a curved mirror with radius R is identical to that of a lens with focal length $R/2$ (or to two lenses with focal length R), the behaviour of a beam in a resonator is equivalent to the beam passing through an infinite series of lenses a distance L apart. Figure 4 shows the "dual" or equivalent resonator to Figure 3. The mirrors in Figure 3 are replaced by lenses with focal lengths $f_1 = R_1$ and $f_2 = R_2$ as shown in Figure 4. The two resonators are equivalent, the only difference being that the ray pattern is folded in Figure 3 and unfolded in Figure 4.

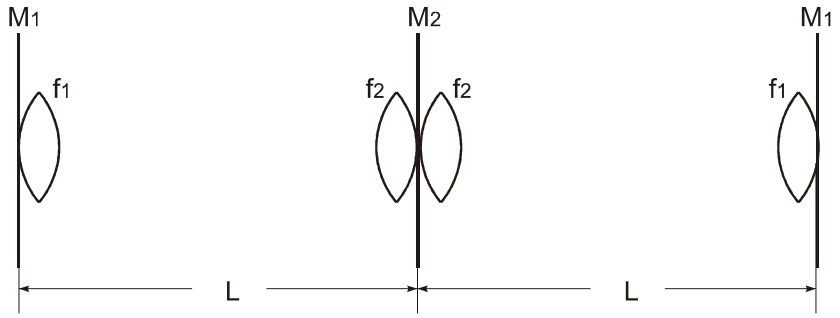

Figure 4 Equivalent resonator of Figure 3, with lenses and flat mirrors.

For comparison, the ray transfer matrix of the unfolded resonator in Figure 4 is:

$$M_{lens} = \begin{pmatrix} A & B \\ C & D \end{pmatrix} = \begin{pmatrix} 1 & 0 \\ -1/f_2 & 1 \end{pmatrix}\begin{pmatrix} 1 & 0 \\ -1/f_2 & 1 \end{pmatrix}\begin{pmatrix} 1 & L \\ 0 & 1 \end{pmatrix}\begin{pmatrix} 1 & 0 \\ -1/f_1 & 1 \end{pmatrix}\begin{pmatrix} 1 & 0 \\ -1/f_1 & 1 \end{pmatrix}\begin{pmatrix} 1 & L \\ 0 & 1 \end{pmatrix} \tag{1-29}$$

$$= \begin{pmatrix} \dfrac{1-2L}{R_1} & \dfrac{2L(R_1-L)}{R_1} \\ \dfrac{-2(R_1+R_2-2L)}{R_1R_2} & \dfrac{4L^2+R_1R_2-2L(2R_1+R_2)}{R_1R_2} \end{pmatrix} \tag{1-30}$$

which is equal to Eq. (1-23) when $f_1 = R_1$ and $f_2 = R_2$.

A geometrical or ray transfer approach is useful to quantify the degree of stability of a resonator but does not predict the intensity distribution of a laser beam. The most common and useful beam produced by a real laser has a Gaussian intensity profile. This is illustrated in Figure 5, and has the form:

$$I(r) = I_0 \exp\left(\frac{-2r^2}{\omega^2}\right) = \frac{2P}{\pi\omega^2}\exp\left(\frac{-2r^2}{\omega^2}\right) \tag{1-31}$$

where P is the total power in the beam, and is the same at all cross sections of the beam, and ω is the size of the laser beam and is defined as the radius at which the beam irradiance (intensity) has fallen to $1/e^2$ (13.5 percent) of its peak value (see Figure 5).

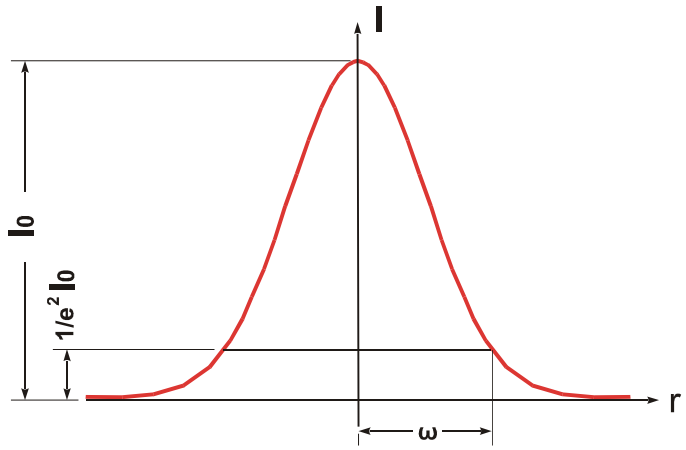

Figure 5 A Gaussian beam profile showing the beam radius ω.

Many lasers are designed to produce a beam with a Gaussian intensity profile (see Figure 5), which has characteristic propagation properties. At some point along the axis of propagation (usually denoted $z = 0$) the beam has the smallest transverse extent, known as the waist, which is also the point at which the wave front is planar.

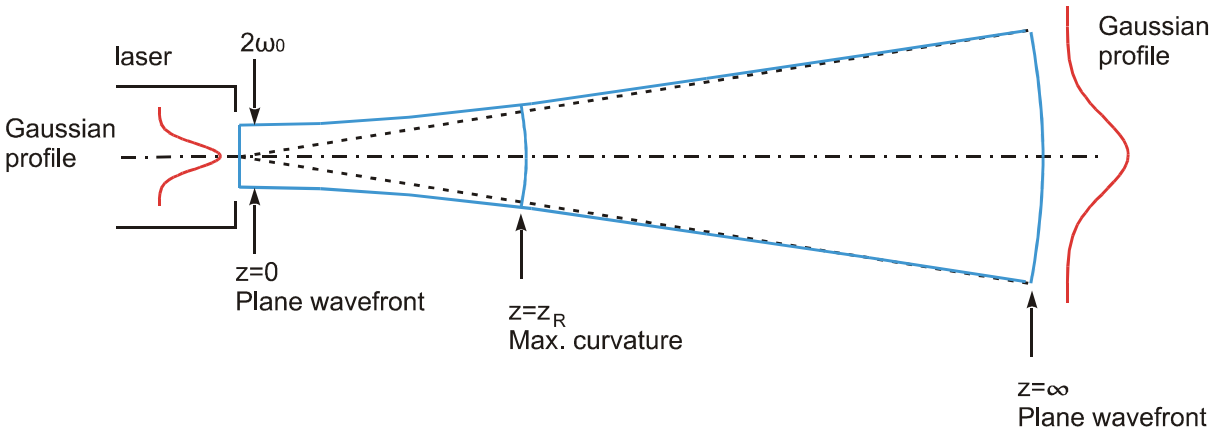

Figure 6 Propagation of a Gaussian laser beam.

Diffraction causes light to spread transversely and causes the wavefronts to acquire curvature as they propagate (see Figure 6) according to:

$$\omega(z) = \omega_0 \left[1 + \left(\frac{z}{z_R} \right)^2 \right]^{\frac{1}{2}} \qquad (1\text{-}32)$$

and $$R(z) = z\left[1+\left(\frac{z_R}{z}\right)^2\right] \tag{1-33}$$

where z is the distance propagated from the plane where the wavefront is flat,

ω_0 is the radius of the $1/e^2$ irradiance contour at the plane where the wavefront is flat,

$z_R = \frac{\pi\omega_0^{\,2}}{\lambda}$ is the Rayleigh range,

$\omega(z)$ is the radius of the $1/e^2$ contour, and

$R(z)$ is the wavefront radius of curvature after propagating a distance z.

If $z = 0$ marks the position of the waist (and the place at which $R(z)$ is infinite), then as the beam propagates $R(z)$ passes through a minimum at some finite $z = z_R$, and rises again toward infinity as z increases, and asymptotically approaches the value of z itself.

Simultaneously, as $R(z)$ asymptotically approaches z for large z, $\omega(z)$ asymptotically approaches the value :

$$\omega(z) = \frac{\lambda z}{\pi\omega_0} \tag{1-34}$$

where z is much larger than $\frac{\pi\omega_0}{\lambda}$ so that the $1/e^2$ irradiance contours asymptotically approach a cone of angular radius :

$$\theta = \frac{\omega(z)}{z} = \frac{\lambda}{\pi\omega_0}. \tag{1-35}$$

This value is the half-angle divergence of the Gaussian TEM_{00} beam and is a measure of the divergence or spread of the beam with distance.

Using the steady-state condition that the radius of the phase front of the beam must be identical at an arbitrary but defined plane in the resonator reveals the property that the intensity distribution is identical at that plane after every round trip, and that this distribution is an eigenmode of the resonator. In a resonator with no apertures there are infinitely many eigenmodes, and these are referred to as transverse electromagnetic (TEM) resonator modes.

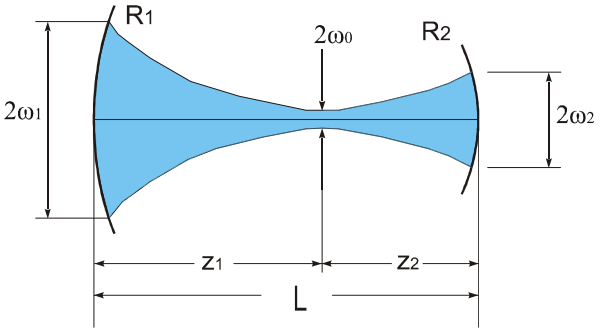

Figure 7 Diagram of a stable Fabry-Perot resonator.

The lowest order, or "fundamental" transverse mode, TEM_{00}, is a Gaussian beam, and has a waist of radius $\omega_{0,}$, defined to be the minimum radius of the beam. For the Fabry-Perot resonator illustrated in Figure 7 the waist is located at a distance z_1 from mirror 1 on the optical axis and a distance z_2 from mirror 2.

The waist size is given by:

$$\omega_0^{\,4} = \left(\frac{\lambda}{\pi}\right)^2 \frac{L(R_1 - L)(R_2 - L)(R_1 + R_2 - L)}{(R_1 + R_2 - 2L)^2}, \tag{1-36}$$

and it is located at

$$z_1 = \frac{L(R_2 - L)}{R_1 + R_2 - 2L} \quad \text{and} \quad z_2 = \frac{L(R_1 - L)}{R_1 + R_2 - 2L}. \tag{1-37}$$

Using Gaussian propagation within the resonator gives the spot sizes on each mirror:

$$\omega_1^{\,4} = \left(\frac{\lambda R_1}{\pi}\right)^2 \frac{L(R_2 - L)}{(R_1 - L)(R_1 + R_2 - L)}, \text{ and}$$

$$\omega_2^{\,4} = \left(\frac{\lambda R_2}{\pi}\right)^2 \frac{L(R_1 - L)}{(R_2 - L)(R_1 + R_2 - L)}. \tag{1-38}$$

The higher-order eigenmodes can take the forms either of Hermite-Gaussian functions (*Lukš* 1976; *Bekshaev* 1999) in rectangular coordinates, or of Laguerre-Gaussian functions (*Wang & Stephan* 1991; *Arlt et al.* 2001; *Webb & Jones* 2004) in cylindrical coordinates. The Hermite-Gaussian modes are denoted by TEM_{nm}, where *n* is the order in the *x*-direction and *m* is the order in the *y*-direction, and have an intensity distribution of the form:

$$I_{nm}(x,y) = I_0\left(H\left(n, \frac{x\sqrt{2}}{\omega} \right) \mathrm{Exp}\left(-\frac{x^2}{\omega^2} \right) H\left(m, \frac{y\sqrt{2}}{\omega} \right) \mathrm{Exp}\left(-\frac{y^2}{\omega^2} \right) \right)^2 . \qquad (1\text{-}39)$$

The Hermite polynomials can be found using (*Stevens* 1963; *Kimel & Elias* 1993):

$$H_n(z) = (-1)^n e^{z^2} \frac{d^n}{dz^n} e^{-z^2} \qquad (1\text{-}40)$$

or $$H_n(z) = (2z)^n - \frac{n(n-1)}{1!}(2z)^{n-2} + \frac{n(n-1)(n-2)(n-3)}{2!}(2z)^{n-4} - +... \qquad (1\text{-}41)$$

The first few Hermite polynomials are given:

$$\begin{aligned} H_0(z) &= 1 \\ H_1(z) &= 2z \\ H_2(z) &= 4z^2 - 2 \\ H_3(z) &= 8z^3 - 12z \end{aligned} \qquad (1\text{-}42)$$

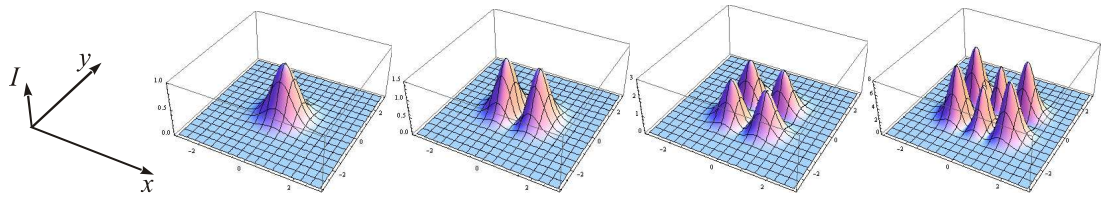

Figure 8 Hermite-Gaussian mode patterns: TEM_{00}, TEM_{10}, TEM_{11}, TEM_{21}.

Figure 8 shows transverse mode patterns for Hermite-Gaussian modes of various orders. Notice that the transverse extent of the modes increases with order.

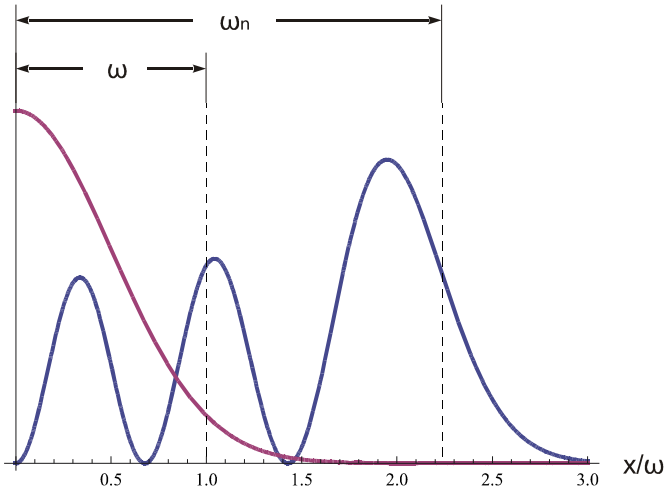

Figure 9 Illustration of radius x_5 of higher-order mode I_{5m}, as compared to the Gaussian spot size ω

The spot sizes of higher-order modes in rectangular coordinates can be approximated by:

$$\omega_n = \omega\sqrt{n} \quad \text{and} \quad \omega_m = \omega\sqrt{m} \tag{1-43}$$

where ω is the spot size of the corresponding TEM_{00} mode and m and n are the orders of the x- and y-modes respectively.

This allows us to determine which higher-order modes will pass through an aperture of radius a, namely those indices given by

$$n < N_{\max} \approx \left(\frac{a}{\omega}\right)^2. \tag{1-44}$$

The eigenmodes can also be equivalently expressed in cylindrical coordinates using Laguerre functions. A Laguerre-Gaussian beam (*Padgett et al.* 1996) is given by:

$$I(r) = I_0\left(2\frac{r^2}{\omega^2}\right)^l\left(L_p^l\left(2\frac{r^2}{\omega^2}\right)\right)^2 \exp\left[-2\frac{r^2}{\omega^2}\right]. \tag{1-45}$$

The Laguerre polynomials $L_p^l(x)$ are the solutions of the differential equation

$$x\frac{d^2L_p^l}{dx^2} + (l+1-x)\frac{dL_p^l}{dx} + pL_p^l = 0. \tag{1-46}$$

Some polynomials of low order are

$$L_0^l(x) = 1$$
$$L_1^l(x) = l + 1 - x \qquad (1\text{-}47)$$
$$L_2^l(x) = \tfrac{1}{2}(l+1)(l+2) - (l+2)x + \tfrac{1}{2}x^2.$$

Figure 10 shows Laguerre-Gaussian modes of various orders.

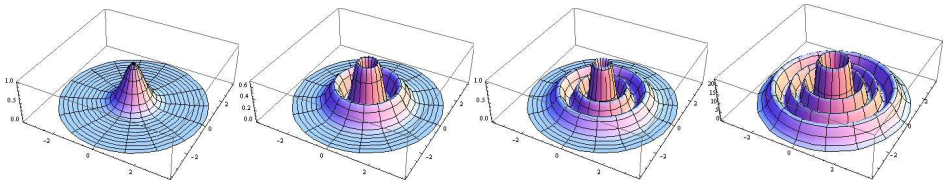

Figure 10 Laguerre-Gaussian mode patterns: L_0^0, L_1^1, L_2^2, L_3^3.

Using Eqs. (1-21) and (1-31), the transmission of a Gaussian beam passing through a circular aperture is given by:

$$T_{00} = 1 - \exp\left(-2\left(\frac{a}{\omega}\right)^2\right). \qquad (1\text{-}48)$$

The transmission of several low-order transverse mode intensity profiles was calculated using Eqs. (1-21) and (1-39) as a function of the aperture radius *a*, and is shown in Figure 11.

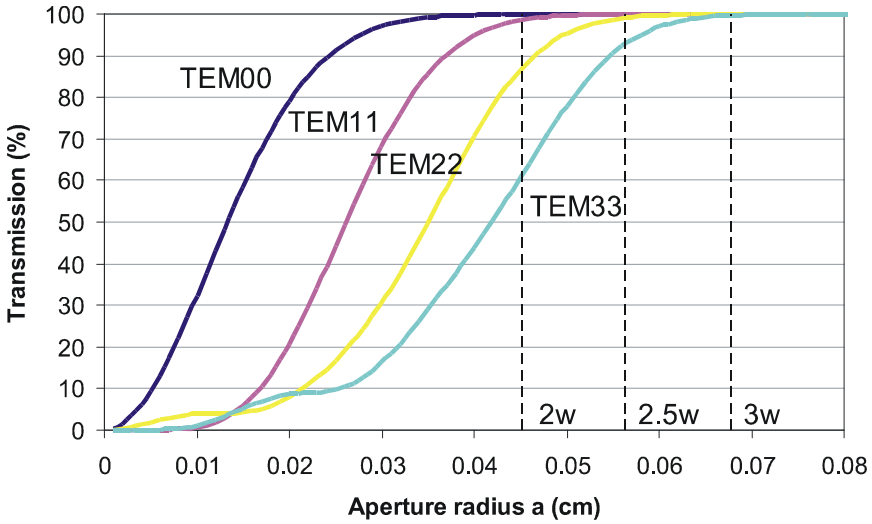

Figure 11 Transmission values for several TEM_{nm} modes as a function of the aperture size. The resonator was modelled with G = 0.75. The vertical lines represent $a = 2\omega_1$, $a = 2.5\omega_1$, and $a = 3\omega_1$ respectively.

Figure 11 illustrates the property of Fabry-Perot resonators that the higher-order modes are larger in transverse extent than lower-order modes, so for any aperture radius *a* it is clear that the Gaussian or TEM_{00} mode has the highest transmission (or lowest loss), and that the higher-order modes have successively lower transmission values (or higher losses). Therefore any aperture inside a resonator will introduce losses which discriminate against higher-order transverse modes and favour the lower-order modes (*Smith* 1972). This effect can be used in a resonator to discriminate against high-order modes and limit a beam to low-order modes (*Blows et al.* 2000). The higher losses of higher-order modes in a resonator also implies that given sufficient time the output beam will converge to the fundamental or Gaussian mode. Spontaneous emission and the reseeding of higher-order modes in a real laser limits the degree of convergence, however.

Some resonators do not produce Hermite-Gaussian (or Laguerre-Gaussian) eigenmodes. It is however also possible to characterize the size and propagation properties of any arbitrary non-Gaussian beam using the Second-Moment method, which is also the basis of the so-called "M-squared" method for characterizing laser beams (*Siegman* 1998). This formulation starts by evaluating the second moment of the beam intensity profile $I(x, y)$ across the rectangular coordinate x (or alternatively across the y coordinate) in the form

$$\sigma_x^{\,2} = \frac{\int_{-\infty}^{\infty} (x - x_0)^2 I(x, y) dxdy}{\int_{-\infty}^{\infty} I(x, y) dxdy} \tag{1-49}$$

where x_0 is the centre of gravity of the beam. The second moment propagates according to

$$\sigma_x^{\,2}(z) = \sigma_{x0}^{\,2} + \sigma_\theta^{\,2} \times (z - z_0)^2 \tag{1-50}$$

where σ_{x0} is the variance at the beam waist;

σ_θ is the variance of the angular spread of the beam departing from the waist; and

z_0 is the location of the beam waist along the z axis.

This quadratic propagation dependence holds for any arbitrary real laser beam, whether it is Gaussian or non-Gaussian.

Considering the x-component of (1-31), the beam spot size parameter ω_x is just twice the variance, i.e. $\omega_x \equiv 2\sigma_x$. Therefore for any arbitrary beam it is convenient to adopt the spot-size or beam-width definitions:

$$W_x \equiv 2\sigma_x \tag{1-51}$$

where (capital) W is the general beam width notation for arbitrary real beams, with this definition being coincident with the Gaussian beam parameter ω for ideal Gaussian beams. The second-moment-based beam width W_x defined above will then propagate exactly like the Gaussian spot size $\omega(z)$ of an ideal Gaussian beam, except for the insertion of an M^2 multiplication factor in the far-field spreading of the beam. This leads to the second-moment width definitions

$$W_x{}^2(z) = W_{0x}{}^2 + M_x{}^4 \times \left(\frac{\lambda}{\pi W_{0x}}\right)^2 (z - z_{0x})^2 \tag{1-52}$$

where M_x is a parameter characteristic of the beam.

As a result, using these definitions one can write the near-field far-field product for an arbitrary beam in the form

$$W_{0x} \times W_x(z) \approx M_x{}^2 \times \frac{z\lambda}{\pi}. \tag{1-53}$$

The parameters $M_x{}^2$ and $M_y{}^2$ give a measure of the "quality" of an arbitrary beam. General properties of these M^2 values include:

• The values of $M_x{}^2$ and $M_y{}^2$ are ≥ 1 for any arbitrary beam profile, with the limit of $M^2 \equiv 1$ occurring only for single-mode Gaussian beams

• The M^2 values evidently give a measure of "how many times diffraction limited" the real beam is in each transverse direction.

Arbitrary real laser beams can then be fully characterized by exactly six parameters, namely W_{0x}, W_{0y}, z_{0x}, z_{0y}, $M_x{}^2$ and $M_y{}^2$.

There are a number of methods or algorithms for measuring the beam diameter (*Wright et al.* 1992), for example the slit scan method (*Chapple* 1994), variable aperture method, knife-edge scan method, and second-moment method (*Siegman* 1993; *Champagne & Bélanger* 1995; *Siegman* 1998). All the methods are reliable for perfect Gaussian beams but suffer from various errors when applied to non-Gaussian beam shapes. The second moment method is a standard method of measuring beam width when using 2D beam profile data (e.g. CCD cameras). This method has difficulties in implementation since noise in the wings of the beam contributes

excessive errors, resulting in deviations in the beam width calculation. This can be avoided by mathematically eliminating any noise.

The second-moment method requires the acquisition of a complete array of beam intensities using a raster-scanned pinhole or a CCD camera (*Roundy* 2008). For simplicity, it is assumed that the beam profile for the measurement of the beam diameter is acquired as a 256x256 square pixel array. Then, the first order linear moments x_c and y_c (the beam centroid coordinates) are given by:

$$x_c = \frac{1}{P_H}\sum_1^{256} xP(x,y) \text{ and } y_c = \frac{1}{P_H}\sum_1^{256} yP(x,y) \tag{1-54}$$

where $P(x, y)$ is the local intensity at each pixel site and P_H is given by:

$$P_H = \sum_1^{256}\sum_1^{256} P(x,y) \tag{1-55}$$

By calculating the second moments about the centroid, beam widths can be determined as

$$\left\langle x^2 \right\rangle_c = \frac{1}{P_H}\sum_1^{256}\sum_1^{256} \left(x - x_c\right)^2 P(x,y)$$

and

$$\left\langle y^2 \right\rangle_c = \frac{1}{P_H}\sum_1^{256}\sum_1^{256} \left(y - y_c\right)^2 P(x,y)\,. \tag{1-56}$$

The beam radii are given by

$$W_x = 2\sqrt{\left\langle x^2 \right\rangle_c} \text{ and } W_y = 2\sqrt{\left\langle y^2 \right\rangle_c}\,. \tag{1-57}$$

This approach was used to verify the beam-size values calculated by the GLAD optical modelling program.

2. ANALYSIS AND NUMERICAL MODEL OF FABRY-PEROT RESONATORS

2.1 Introduction

The temporal development of the transverse modes of simple Fabry-Perot resonators was studied using a numerical model. The temporal behaviour of the spot size, beam quality factor (M^2) and loss is presented, and the values of these parameters given by the numerical model are compared with those from analytical models. The mode patterns from the numerical model are compared with the patterns predicted for stable Fabry-Perot resonators. Agreement between the numerical model and analytical models lends credibility to this method of modelling a laser resonator.

In the analysis that follows a symmetrical resonator with two spherical mirrors of radius $R_1 = R_2 = R$ separated by a distance L, and with two clear apertures of radius a located at the mirrors, was modelled for simplicity. The formalism is easily extended to the asymmetric case where $R_1 \neq R_2$. A schematic representation of a symmetrical stable Fabry-Perot resonator is shown in Figure 12.

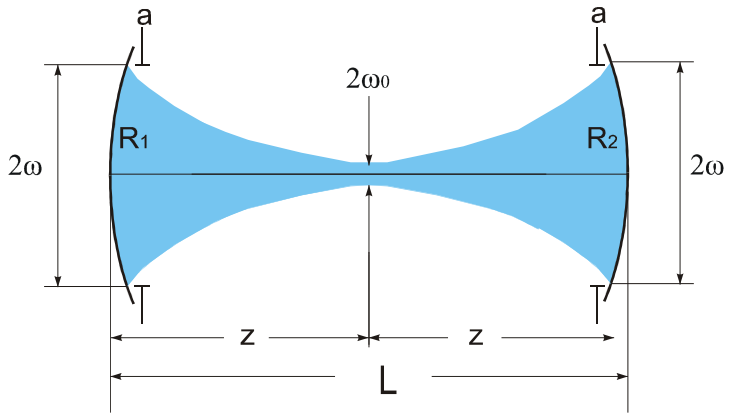

Figure 12 Symmetric Fabry-Perot resonator.

As noted in Section 1-1, any chosen stable resonator is equivalent to any other with the same values of the equivalent G-parameter and effective Fresnel number when considering resonator stability, beam modes and loss. For the special case of a symmetric Fabry-Perot resonator with both mirrors apertured the equivalent G-parameter is given by (*Hodgson & Weber* 2005, p.267-270):

$$G = g_1 = g_2 , \tag{2-1}$$

and the effective Fresnel number is given as in Eq. (1-28) by:

$$N_F = a^2 / \lambda L \tag{2-2}$$

In the following models and calculations the resonator length L was kept at 10 cm, and the mirror radius R and clear aperture radius a were varied. Resonators with the effective G-parameters G = -0.111, G = 0.5, G = 0.75, G = 0.833, G = 1.0 were modelled, with N_F values between 1.5 and 18.

2.2 Numerical model of a Fabry-Perot resonator

A physical optics numerical model based on the propagation of optical beams, which are represented by the complex amplitude of the optical wavefront, through optical components was developed for a symmetric Fabry-Perot resonator to simulate a beam travelling between two mirrors, from laser switch-on and over any number of round trips[1] (*Lawrence* 1987; *Lawrence* 1991; *Vtorova et al.* 1991; *Siegman* 2000). A single beam was defined on a full-width field of 0.3 cm in a 256 x 256 array. The resonator was comprised of two spherical end mirrors of radius R, which were separated by a distance L. In the model, apertures located at the mirrors defined the clear or limiting aperture a of the resonator. In an actual resonator, if no aperturing components are included in the resonator, then the limiting aperture would be the radius of the component which limits the transverse extent of the beam, typically the laser rod or mirror mounts. The resonator contained no gain medium, and the mirrors were taken to reflect 100% of the radiation, so that the only losses considered were the losses at the mirror apertures. The initial beam was randomly generated noise, and the gain was simulated by recording and then resetting the energy to unity after each round trip, giving the loss per round trip due to diffraction only. A wavelength of 1.064 μm was used, since the models would be compared to a laboratory Nd:YAG laser. A diagnostics subroutine characterised the beam, and on each round trip the aperture size, spot sizes and the beam quality or M^2 in the x- and y-directions as well as the loss were written to a text file for analysis. The beam pattern was recorded after each round trip in order to visualise the changes in intensity distribution; it proved useful to record sequences of beam patterns at various stages of mode development.

The following data is typical of that obtained from the numerical model, and the temporal behaviour of parameters like spot size, M^2, loss, and mode structure can be used to characterise

[1] The GLAD code is given in Appendix 7.1.

a resonator. The specific resonator with L = 10 cm, R = 40 cm, and clear aperture radius a = 0.056 cm was modelled, and some pertinent results are presented.

Figure 13 shows the spot size ω as a function of the number of round trips p, so also as a function of time. The spot size ω_x (component in the x-direction) is shown, but the modes are radially symmetrical, so the y-values are identical. The spot sizes ω_x and ω_y are calculated with the second moment method described in Section 1.1.

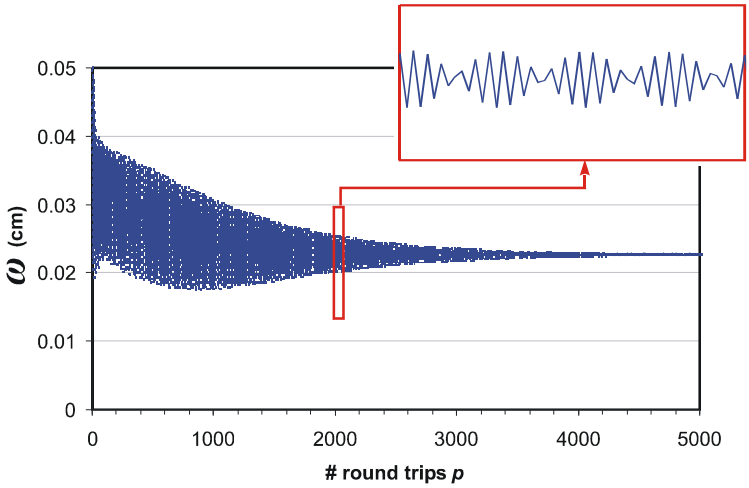

Figure 13 Spot size ω (x-direction) as a function of the number of round trips p.

Initially, when the beam is simply apertured noise, the spot size is large and comparable to the aperture radius. As the beam traverses several passes through the resonator the more divergent elements of the beam are apertured and absorbed, and the spot size is confined between an upper and lower bound. The spot size changes on each round-trip between these bounds, and the spot size converges to ω = 0.022631 cm, which is within 0.01% of the theoretical value (using Eq. 1-28), after approximately 4000 round trips. The oscillation of the spot size between an upper and a lower bound can be understood as the transfer of the beam energy between low-order transverse modes. When the data is expanded along the p-axis sufficiently to view the point-to-point behaviour, a periodic structure is evident.

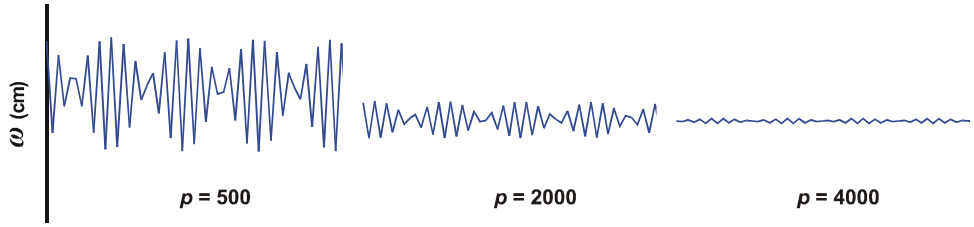

Figure 14 Change of amplitude of pattern with the number of round trips *p*.

The same pattern is observed at all points along the *p*-axis, but the magnitude of the pattern decreases between the upper and lower bounds towards convergence, when the pattern disappears. This can be seen in Figure 14, where the amplitude of the periodic pattern is shown near 500, 2000 and 4000 round trips through the resonator.

Figure 15 shows the behaviour of the beam quality factor, M^2, as a function of the number of round trips, or with time, after switch-on.

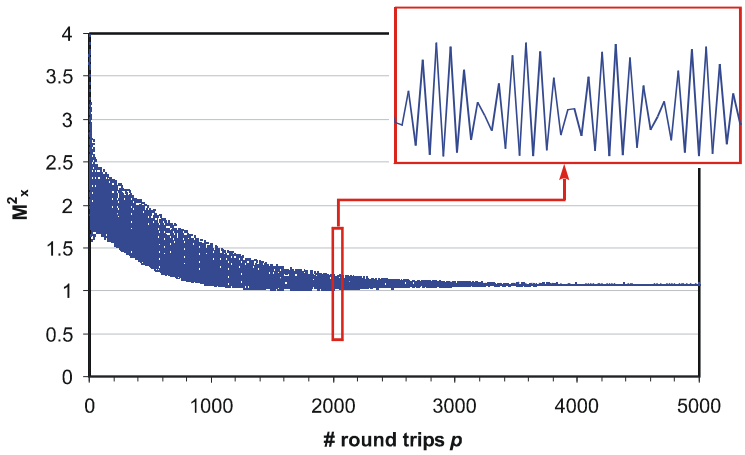

Figure 15 M^2 (*x*-direction) as a function of the number of round trips *p*.

The behaviour of M^2 shows a similar pattern to that of the spot size ω, namely that the value is initially high before any mode structure is evident, and then decreases by oscillating within bounds until it converges at about 4000 round trips. M^2 converges to a value of 1.07, which is close to the M^2 value of 1 for a Gaussian beam (see Section 1.1 on page 17).

Figure 16 shows the round-trip diffraction loss as a function of the number of round trips *p*. The loss was calculated by noting the amount of energy lost from the beam after one round trip through the resonator as a percentage of energy before the round trip. Note again that in the

simulation the energy does not continuously decrease with each round trip but is re-normalized to unity after the loss calculation, and also that any absorption losses or loss due to radiation coupled out of the resonator are not included.

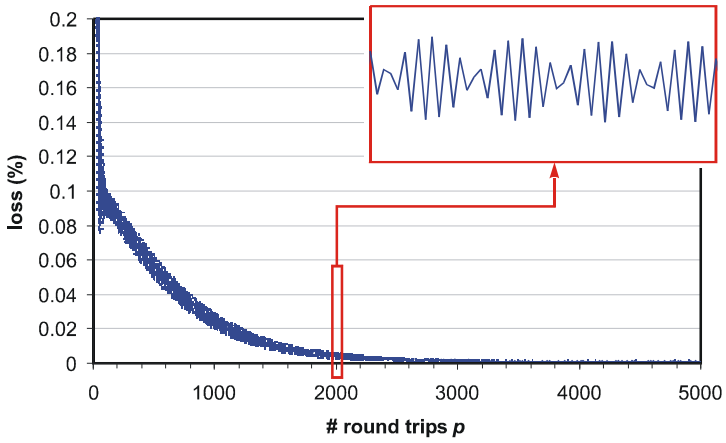

Figure 16 Loss as a function of the number of round trips *p*.

The loss is initially high corresponding to the absorption of the non-axial elements of the beam as the beam is apertured at successive mirrors. It decreases within narrow bounds and converges to a value of 0.0011% after approximately 4000 round trips. The loss too exhibits an oscillatory behaviour, the pattern and period of which remains throughout the history of the beam, although the amplitude decreases with time as the beam converges.

The graphs of the spot size ω, M^2 and loss all show an oscillation of a fixed pattern and period (although decreasing in amplitude in each case). A close inspection of the mode after each round trip reveals the significance of the pattern.

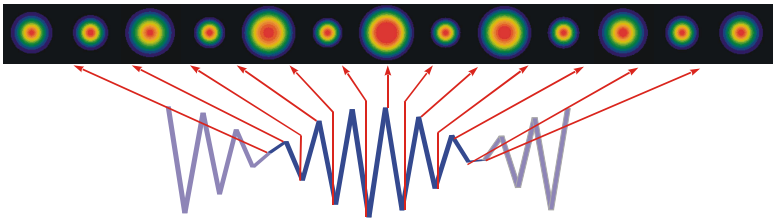

Figure 17 Mode structure after successive round trips, showing correspondence to spot size.

Figure 17 shows the mode at the first mirror after each round trip after 1000 round trips, and how each successive spot corresponds to a point on the oscillatory pattern. The pattern of modes repeats every 13 round trips, as suggested by the detail of the plots of spot size, M^2 and loss.

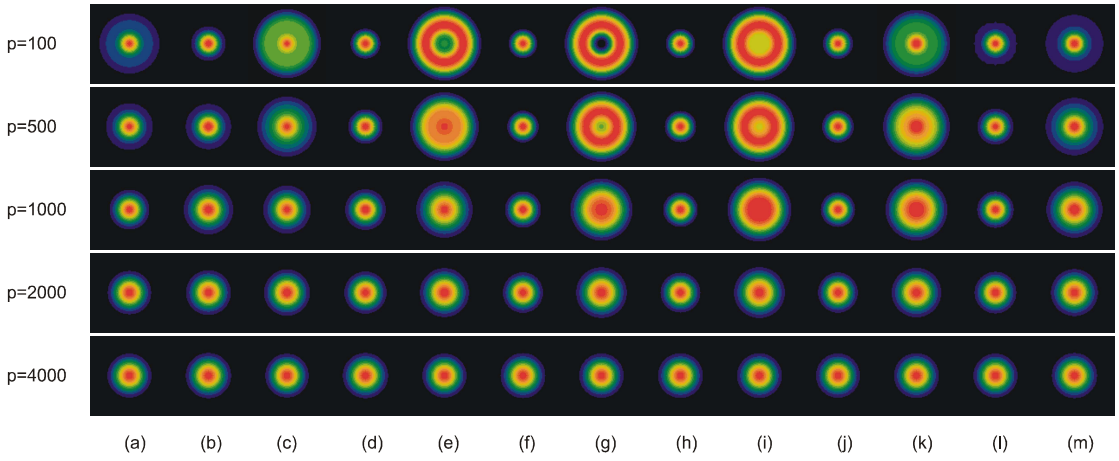

Figure 18 Series of beams, one per round trip, at several points in the evolution of the mode.

Figure 18 shows the series of 13 round trips at several different moments in time along the evolution of the mode pattern. After 100 round trips the nature of the spot size oscillation becomes clear – there is clearly a mixture of TEM_{00} (Gaussian) and TEM_{10}^{*} (doughnut) modes, and there is a significant change in the spot size from one round trip to the next. The largest mode pattern (g) is a doughnut mode, with the intensity at the centre dropping to zero. Alternate spots ((b), (d), (f), (h), (j) and (l)) have a Gaussian distribution pattern. At around 500 round trips the series of modes still shows a large variation in spot size, but the centre of mode (g) is no longer zero. The series at 1000, 2000 and 4000 show a progressive convergence to a constant Gaussian mode.

Pioneering work on the numerical modelling of resonators was done in order to study the losses associated with low- and higher-order transverse modes in stable Fabry-Perot resonators, which shows that higher-order modes experience increasingly higher losses (*Fox & Li* 1961; *Fox & Li* 1963; *Fox & Li* 1968). This leads to the tendency of a beam consisting of high-order modes to converge to lower-order modes. Also pertinent are studies in which the fractions of higher-order modes are measured, and the periodic oscillation of intensity in a CO_2 TEA laser with a Fabry-Perot resonator is found to be caused by competing modes (*Martinez et al.* 1997; *Encinas-Sanz et al.* 1999).

Figure 19 shows how the size of the intracavity apertures affects the rate of convergence of the mode structure. An aperture value of $a = 2\omega$ exhibits convergence after about 200 round trips; $a = 2.5\omega$ converges after about 4000 round trips, and the $a = 3\omega$ case had still not completely converged after 30000 round trips.

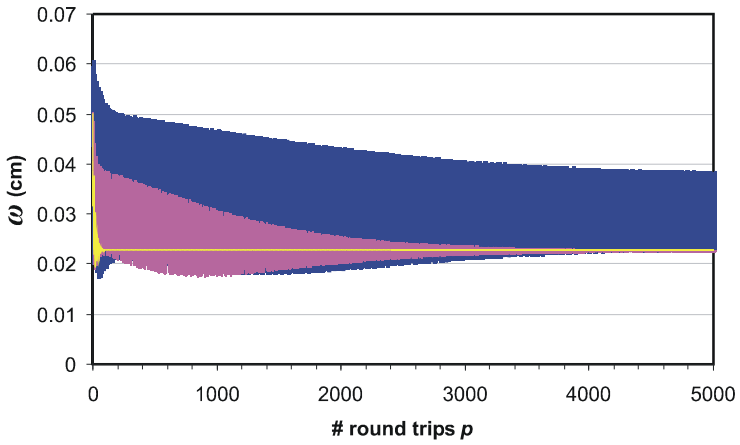

Figure 19 Spot size ω (x-direction) on the mirrors as a function of the number of round trips p for aperture values $a = 2\omega$ (yellow), $a = 2.5\omega$ (purple), $a = 3\omega$ (blue).

Figure 19 suggests that soon after switch-on a beam oscillates between a number of higher-order transverse modes, and that after a sufficiently large number of passes the mode converges to the TEM_{00} or Gaussian mode. The number of passes required for convergence depends on the clear aperture radius a; the larger the aperture and consequently the effective Fresnel number N_F, the slower the beam converges to the Gaussian mode.

This trend of slower convergence with increasing N_F was found to hold for every resonator studied and can be explained by greater discrimination against the higher-order modes in all resonators, but which is more pronounced in resonators with smaller apertures and correspondingly lower values of N_F.

2.3 Verification of numerical model

Analytical models which necessarily make certain assumptions and approximations are routinely used to calculate resonator parameters. In this section a brief discussion of each expression derived from a widely accepted analytical model is followed by a comparison between the results obtained for the analytical method and the numerical method to validate the results given by the numerical model.

The analytical expressions for the waist radius ω_0 (Eq. (1-36)) and beam radius at the mirrors, ω_1 and ω_2 (Eq. (1-38)) are derived from the propagation path of a Gaussian beam in a resonator. The mirrors are assumed to be effectively infinitely large, and the model includes no edge effects. The numerical model, on the other hand, is the repetitive propagation of the beam through a resonator as a complex wave function, and includes diffraction.

Table 3 Comparison of beam sizes calculated analytically and with a GLAD numerical model.

	ω_0	$\omega_1 = \omega_2$	
G	(cm)	(cm)	
	Analytical	Analytical	GLAD
-0.111	0.012307	0.018461	0.018593
0.75	0.021167	0.022628	0.022631
0.833	0.023699	0.024753	0.024944

The beam waist radii ω_0 were not calculated explicitly in the numerical model; the values given were calculated analytically. Analytical values of the spot size on both mirrors $\omega_1 = \omega_2$ (for a symmetrical resonator) were calculated, and compared to the value to which ω_1 converges in the numerical model. The values are found to differ by typically less than 0.7%, and the agreement is good.

Since the apertures are located at the mirrors where the beam size is ω_1 (or ω_2), and noting (Eq. (1-22) and Eq. (1-48)) that T_{00} (and therefore V) is a function of $\frac{a}{\omega_1}$ only, the round-trip loss of a Gaussian beam (T_{00}) over two passes (or one round trip) through any resonator (with $-1 < G < 1$) was calculated analytically for $\frac{a}{\omega_1} = 2$, 2.5 and 3 respectively. These values are shown in the first row of Table 3.

The loss values from the numerical model were found not to be independent of G, so three values of G were used, namely G = -0.111, 0.75 and 0.833 respectively. The numerical model values are those of a *converged* diffractive beam passing through apertures with the same $\frac{a}{\omega_1}$ -values as used in the analytical calculation.

The agreement between the analytical and numerical results is not good, with significantly higher losses from the numerical model, but this stems from an important difference in these two modelling techniques. The analytical model assumes that the beam has a perfect Gaussian intensity distribution which extends in the transverse direction to infinity. The losses in the numerical model must correspond mainly to the losses of a TEM_{00} beam, with small contributions from the competing higher-order modes. It is reasonable to assume that these higher-order modes account for the higher losses of the numerical model.

An alternative approach to calculating the round-trip losses V (*Hodgson & Weber* 2005, p.267-270) was followed as a comparison to the methods followed above. For the case of a stable symmetric resonator apertured at both mirrors the round-trip losses for the TEM_{00} modes can be approximated with the empirical relation

$$V = \exp\left(-\alpha N_F{}^{\beta}\right) \tag{2-3}$$

where $\alpha_{00} = 2.9$ and $\beta_{00} = 1.16$ for the case $G = 0.8$.

Table 4 shows a comparison of the round trip losses calculated using (2-3) for the case $G = 0.8$ with the round trip losses from the numerical model for the case $G = 0.83$. The agreement is better, especially for the smallest aperture size ($a = 2\ \omega_1$ or $N_F = 1.9$).

Table 4 Comparison of round trip loss calculated analytically, with the numerical model, and using an empirical method.

	G	***V* (%)**		
		$\underline{a}=2\omega_1$	$\underline{a}=2.5\omega_1$	$\underline{a}=3\omega_1$
Analytical (TEM_{00})	all G, $-1 < G < 1$	6.709×10^{-4}	7.453×10^{-6}	3.046×10^{-8}
Numerical (converged)	-0.111	0.14907	0.00158	0.00090
	0.75	0.17211	0.00116	0.00073
	0.833	0.16966	0.00096	0.00048
Empirical (TEM_{00})	0.8	0.203	0.00304	1.27×10^{-5}

The selective influence of loss at an aperture is clear, however: higher-order beams are selected *against*, with higher loss, and lower-order modes are selected *for*, and will dominate after sufficiently many round trips. This supports the understanding that the mode pattern converges to the lowest-order mode in the absence of perturbations like continuous reseeding by spontaneous emission in the resonator.

The periodicity of a beam in a laser resonator can be defined as the number of round trips required for any ray to return to an initial position and orientation, and can be found using geometrical ray analysis. Applying this to a stable, symmetrical Fabry-Perot resonator, if an initial ray vector $\underline{r}_0$ corresponds to an infinitesimal element of a mode pattern, then using Eqs. (1-6), (1-7) and (1-15), after p cycles the ray vector $\underline{r}_p$ is:

$$\underline{r}_p = \beta_1 \underline{v}_1 e^{ip\theta} + \beta_2 \underline{v}_2 e^{-ip\theta}$$

so
$$\underline{r}_p = \underline{r}_0 \cos p\theta + i(\beta_1 \underline{v}_1 - \beta_2 \underline{v}_2)\sin p\theta . \tag{2-4}$$

From Eq. (1-23) in Section 1-1, the ray transfer matrix M_{mir} of an empty symmetrical Fabry-Perot resonator in terms of G is given by:

$$M_{mir} = \begin{pmatrix} 2G^2 - 1 & GR(1-G) \\ -4G/R & 2G^2 - 1 \end{pmatrix} \tag{2-5}$$

where L and R are shown in Figure 12, and G is defined in Eq. (2-1).

Then by Eqs. (1-11) and (1-12):

$$\lambda_{1,2} = 2G^2 - 1 \pm 2\sqrt{G^2(G^2-1)} \tag{2-6}$$

are the eigenvalues and functions only of G, and

$$\underline{v}_{1,2} = \begin{pmatrix} \pm \frac{1}{2}\sqrt{G^2 - 1}R \\ 1 \end{pmatrix} \tag{2-7}$$

are the eigenvectors of the matrix M_{mir}.

From Eq. (1-11)
$$m = 2G^2 - 1 \tag{2-8}$$

and from Eq. (1-15),
$$\theta = \arccos(2G^2 - 1). \tag{2-9}$$

By Eq. (2-4), the ray exhibits periodicity when $\underline{r}_p = \underline{r}_0$, or when $\cos p\theta = 1$ (and $\sin p\theta = 0$). This gives the condition for periodicity:

$$P = 0, \frac{2\pi}{\theta}, \frac{4\pi}{\theta}, \ldots \tag{2-10}$$

where P is the periodicity and number of round trips, and *must* be a *whole number*.

If $\underline{r}_0 = \begin{bmatrix} y_0 \\ y'_0 \end{bmatrix}$ and $\underline{r}_p = \begin{bmatrix} y_p \\ y'_p \end{bmatrix}$, then to plot the ray position y_p it is first necessary to solve the simultaneous equations implicit in Eq. (1-6) to calculate:

$$\beta_{1,2} = \pm \frac{y_0}{R\sqrt{G^2 - 1}} + \frac{y'_0}{2} . \tag{2-11}$$

Now using Eq. (2-4) $\underline{r}_p$ can be plotted as a function of p. In the following graphs the ray position y is plotted. The ray slope y' shows the same periodicity[2].

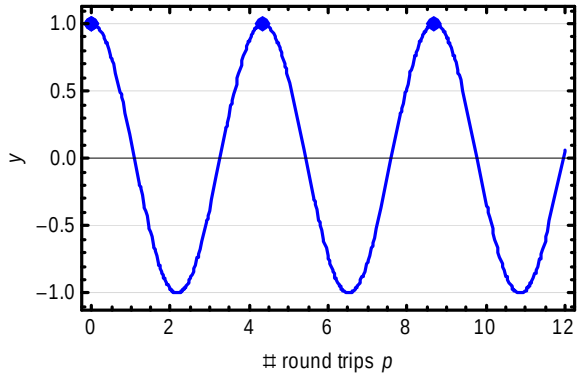

Figure 20 Plot of ray position y_p as a function of the number of round trips p for the particular case where $G = 0.75$. The periodicity is indicated with points, and periodicity $P = 4.35$ in this case.

In Figure 20 the ray position y is plotted as a function of p for the case $G = 0.75$. In this case the periodicity is 4.35, which is not a whole number. Since $\underline{r}$ is *any* ray in the beam this means that the beam will vary periodically, but the points at which it is identical to the initial beam will occur at some point within the resonator and not on the starting mirror. Therefore the mode on the starting mirror will be the same as the initial mode only when $p = kP$ is a whole number for some integer k.

Whole values for the periodicity can be calculated by using the steps (2-4) to (2-10) in reverse, namely using a chosen periodicity to calculate θ, m, G (and therefore g) and lastly R for some chosen L. Notice that Eq. (2-8) yields two G-values:

$$G = \pm\sqrt{\frac{m+1}{2}}. \tag{2-12}$$

There are therefore two resonators which both have the same periodicity P. For example, if $m = 0.5$ then both a resonator with $G = 0.866$ and a resonator with $G = -0.866$ will have periodicity $P = 6$. Figure 21 shows the plot of a ray passing through these two resonators. Note that in the resonator with $G < 0$ the ray is contained and does not extend transversely beyond the starting position, whereas the resonator with $G > 0$ has a greater transverse extent.

[2] The Mathematica eigenfunction code to calculate the periodicity is given in Appendix 7.2.

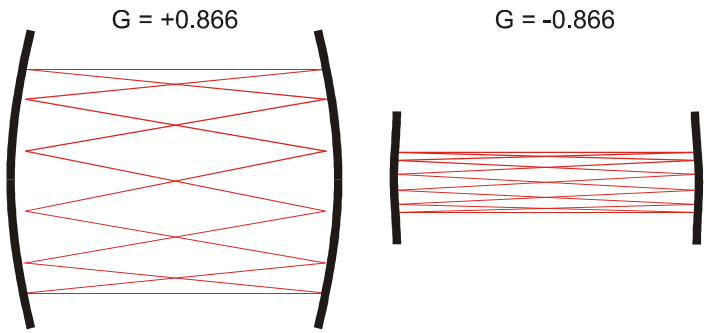

Figure 21 Plots of a ray path through two resonators, both with m = 0.5 and periodicity P = 6 round trips. Note that these plots are drawn to the same scale.

In both the numerical as well as the analytical (or eigenmode) models the periodicity is found to depend only on the equivalent G–parameter, which quantifies the stability, and not on the effective Fresnel number N_F.

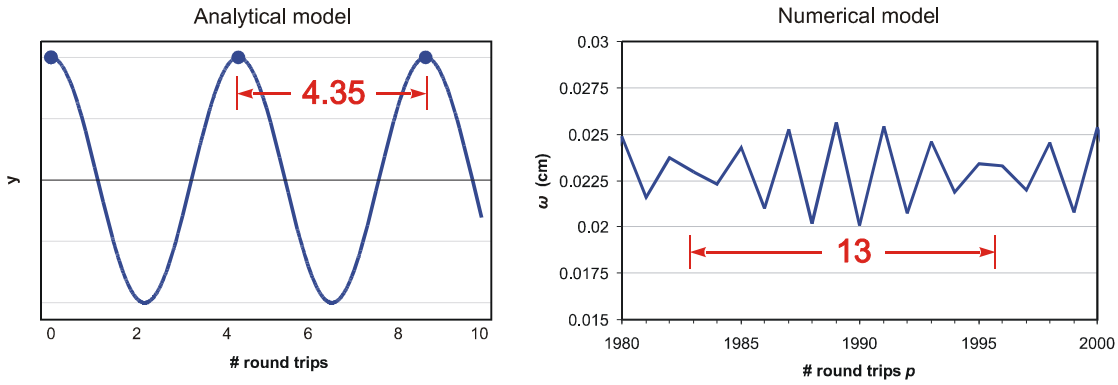

Figure 22 Comparison of Numerical and Analytical models of resonator with G = 0.75, with non-identical periodicity.

Figure 22 shows the periodicity in the output of the numerical model typical of stable resonators (as already seen in Figures 13 to 16 in the behaviour of the spot size, M^2 and loss) compared to the ray position behaviour from the eigenmode model. It is immediately evident that the periodicity differs – for the numerical model it is 13, whereas for the eigenmode model it is 4.35. This value being close to 4.33 and the fact that 3 x 4.33 = 13 implies that after a single cycle the ray has returned to its initial height and slope at an intermediate position along the optical axis, and that three cycles or 13 round trips are required for the ray to return to its initial height and slope at the initial position. Indeed, setting r_0 = (1, 0) and substituting p = 13 into (2-4) gives r_{13} = (1, 0) as expected. This is consistent with the requirement that the periodicity be a whole number for the ray to return to its initial height and slope *at the initial position*.

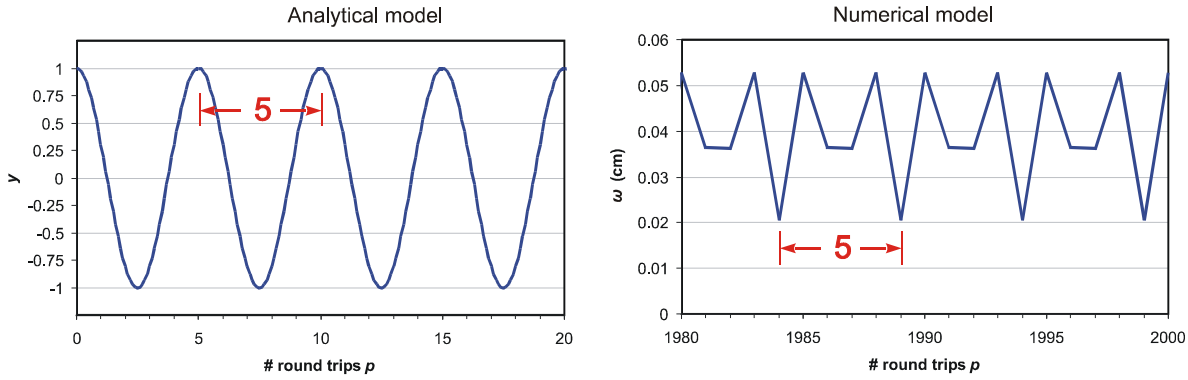

Figure 23 Comparison of Numerical and Analytical models of resonator with G = 0.809, with identical periodicity (P = 5) in both cases.

By comparison, Figure 23 shows the periodicity from the numerical model for a resonator corresponding to the analytical or eigenmode model for the case of P = 5, a chosen whole number. In this case, and for all resonators corresponding to whole-number P-values (for $P > 2$), the periodicity of the numerical model was found to exactly match that of the analytical model.

2.4 Conclusion

A numerical model of a stable Fabry-Perot resonator was developed. The numerical model was tested against several different "text-book" analytical models, and predictions of spot size and M^2 were found to be in good agreement. There was some discrepancy in the round-trip loss figures obtained which was understandable since the analytical loss model was not an intra-cavity model. These values can therefore be used with confidence for resonator design.

The model is also able to produce a picture of the competing temporal processes in a resonator, which is useful for modelling modal build-up in an empty Fabry-Perot resonator. 2-D plots of the beam are easily produced, allowing for graphical comparison and interpretation.

The following tendencies of stable Fabry-Perot resonators were noted:

- The round-trip loss decreases with increasing N_F
- The spot sizes (waist and on the mirrors) are a function of L and R only
- The time or number of round trips required for convergence increases with increasing N_F
- Given sufficient time, a resonator will always converge to the lower-order TEM mode TEM_{00}

- The periodicity in the spot size, M^2 and loss is a function of G only

Although only the intensity of beams was discussed, the numerical model contains complete phase information, at every point on the beam and at every time in its evolution. This information would be valuable if the model was extended to include intra-cavity phase elements, for example.

For this project the model was extended to the more complex Porro prism resonator.

3. PORRO PRISM LASERS

3.1 Introduction

The Porro prism resonator configuration has been widely used for over 30 years in commercial and military applications where their inherent ruggedness makes them ideally suited to applications where a laser beam is required at a large distance from the source, and where the source is not a stable platform. In typical field use the conditions these resonators are subject to could include shock and large temperature variations, and will experience some degree of optical misalignment. Porro resonators have been extensively used in long-range military beam applications like range finders and laser designators (*Dudeja* 1989; *Singh et al.* 1995; *Cole* 1998; *Bahuguna et al.* 2007), as well as in exotic laser systems such as the Mars Observer Laser Altimeter (*Afzal* 1994), the CALIOP lidar system (*Winker et al.* 2004), the XI UV laser trigger system (*Sundvold et al.* 1999), and in a LASTEC diode-pumped Nd:YAG laser for use in space (*Joseph* 2007).

Porro prism lasers have been incorporated into many patents (*Richards* 1982; *Lundstrom* 1983; *Lundstrom* 1984; *Severinsson* 1985; *Reeder* 1988; *Reed* 1997; *Gregor et al.* 1998; *Ishizu* 2004; *Yanagisawa & Hirano* 2005), and into several experiments, including a laser for the production of synchronized giant radiation pulses (*Podgaetskii & Chernets* 1967), an experiment to optimize the cooling of slab Nd:glass lasers (*Lu et al.* 1989), an experiment to determine the output energy characteristics in rotating mirror Q-switch lasers (*Lukac* 1991), and in experimental techniques to eliminate parasitic lasing in high-gain lasers (*Storm* 1992).

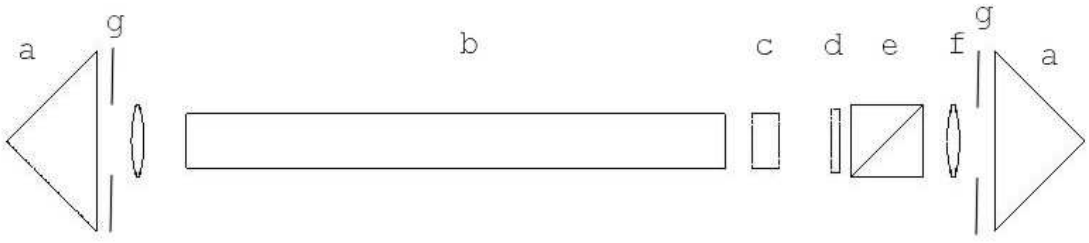

Figure 24 Schematic diagram of a Porro prism resonator, showing the following optical elements: (a) Porro prisms, (b) Nd:YAG rod, (c) Q-switch, (d) quarter-wave plate, (e) polarizing beam cube, (f) lenses, and (g) apertures.

The Porro prism resonator investigated in this study, shown schematically in Figure 24, was based on a flash lamp pumped Nd:YAG laser with passive Q–switching and Porro prisms in the place of end mirrors.

In this section the literature on Porro resonators is reviewed, after which some useful results are summarized.

3.2 Literature review

The study of Porro prism resonators followed from early work on flat-roof resonators commonly used in microwave systems (*diFrancia* 1965; *Checcacci et al.* 1966; *Pasqualetti & Ronchi* 1973; *Ronchi* 1973; *Mansfield et al.* 1983; *Yassin & Lain* 1985).

Right angle prisms, often referred to as Porro prisms, have the useful property that all incident rays on the prism are reflected back parallel to the initial propagation direction, independent of the angle of incidence. Thus an initial planar wave front remains planar after reflection. This property was initially exploited in Michelson interferometers (*Peck* 1962) to relax the tolerances on misalignment, and then proposed (*Gould et al.* 1962) as a means to overcome misalignment problems in optical resonators employing Fabry–Perot cavities by replacing the end face mirrors with crossed roof prisms.

Much of the theoretical work to date has focused on geometric methods to model the inverting properties of such resonators (*Kuo & Ko* 1984). The prism can be modelled as a ray deviator by replacing an imaginary mirror some distance behind the prism, and the alignment sensitivity of Porro resonators is quantified by deriving an expression for the beam centroid displacement as a function of prism misalignment. The main effect of misalignment is to reduce the active volume of the laser medium (*Lee & Leung* 1988; *Lee & Leung* 1989a; *Lee & Leung* 1989b). The model correctly accounts for the beam direction, but does not account for the complex field distribution found experimentally from the laser. Optical ray tracing software extends these results (*Rapaport & Bass* 2000), (*Rapaport et al.* 2001), and geometrical techniques can also be used to study the properties of a prism to determine the conditions to prevent a beam from being obscured by the prism's surfaces (*Tsai & Lin* 2008). A recurrence relation is found which describes the stepping of rays around the longitudinal axis of a Porro prism resonator (*See et al.* 1980), but the effect of this on the beam structure is not discussed.

Internal phase shifts and output polarization states are accounted for using polarization considerations in several papers. Early work deals with the polarization in resonators with a Porro prism replacing one end mirror (*Buchman* 1965; *Podgaetskii & Chernets* 1967). The first comprehensive study of polarization in a Porro resonator shows the effect of polarization on the

output coupling reflectivity, the Q-switch, and the stored energy in a laser rod (*Chun & Teppo* 1976). A comment in the conclusion of this paper explains the usefulness of these resonators, and the subsequent military interest:

"The laser rangefinder has successfully withstood 150 g's on a shock machine and has been subjected to actual ground firing. Earlier tests of the resonator alone indicate no change in the alignment of the optical assembly after 17,000 cycles of up to 200-g peak acceleration."

The rotation of a prism in a Porro prism resonator can be used to optimize the energy extracted from a laser (*Chen et al.* 1996), and to compensate for birefringence and increase the performance of lasers using cylindrical laser rods (*Richards* 1987). A Jones matrix formulation can be used to describe the phase shifts introduced by Porro prisms and other polarizing elements in a Porro resonator (*Agrawal et al.* 2007). Clearly the rotation of the prisms with respect to each other is an important property of Porro prism resonators and, as will be shown later, is found to have a profound effect on the beam structure.

3.3 Pumping and gain

The laser medium, Q-switch and means of excitation are identical to a traditional solid-state laser. The choice of the gain medium determines the wavelength that the laser will produce. The work in the following sections is general and applicable to any gain medium. However, Porro resonators are commonly used with Nd:YAG lasers (wavelength 1064 nm) which have high gain and are simple and rugged enough to be useful in field application (*Dudeja* 1989; *Afzal* 1994; *Singh et al.* 1995; *Cole* 1998; *Winker et al.* 2004; *Bahuguna et al.* 2007; *Joseph* 2007). In the system under discussion the active medium was a 50 mm long Nd:YAG rod of radius 3 mm, and the laser was pulsed using a Cr^{4+}:YAG passive Q–switch.

The energy or power which can be obtained by a laser is determined by the active volume or the volume of gain medium which contributes to the lasing process.

3.4 Properties of prisms

Mirrors have the well-known property that they reflect an incident ray at an angle equal to the incident angle (*Hecht & Zajac* 1997). As a consequence, any tilt of a mirror will result in a deflection of the reflected ray away from the optical axis. Porro prisms, however, are simple 45°-90°-45° prisms orientated to reflect an incident ray.

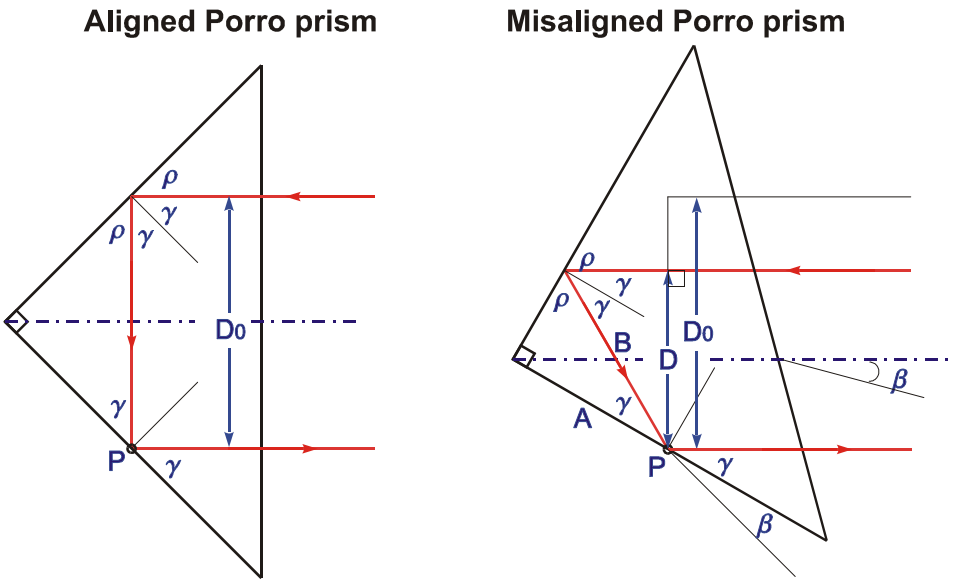

Figure 25 Reflection of a ray by an aligned and misaligned Porro prism.

Referring to Figure 25, when a Porro prism is tilted by an angle β about an axis which lies along the apex of the prism the shift in the optical axis can be calculated as follows:

$$\gamma = \tfrac{\pi}{4} \pm \beta \qquad \text{so} \qquad \rho = \tfrac{\pi}{4} \pm \beta \,.$$

Also $$\sin 2\gamma = \frac{D}{B} \qquad \text{and} \qquad \cos\gamma = \frac{A}{B} \,.$$

Solve for *B*:

$$\frac{D}{\sin\left[2\left(\frac{\pi}{4} \pm \beta\right)\right]} = \frac{A}{\cos\left(\frac{\pi}{4} \pm \beta\right)}$$

$$D = 2A\sin\left(\frac{\pi}{4} \pm \beta\right)$$

For $\beta = 0$: $$D_0 = \sqrt{2}A$$

Then for $\beta \neq 0$

$$\frac{D}{D_0} = \left(\cos\beta \pm \sin\beta\right)$$

$$\frac{D}{D_0} \approx 1 \pm \beta \qquad \text{for small angles } \beta\text{, in radians.} \qquad (3\text{-}1)$$

Therefore any tilt of a prism around the apex of the prism will cause only a small shift (proportional to the tilt angle of the prism) parallel to the optical axis.

By “crossing” the Porro prisms, so that the apexes are at 90° to each other (as shown later in Figure 34), any misalignment in one direction is compensated for by one prism and any misalignment in the orthogonal direction is compensated for by the other prism, thus making the resonator insensitive to misalignment. If the azimuthal angle α is less than 90° then an angular misalignment of one prism is only partially converted into a shift of the beam parallel to the optical axis, with some residual angular deflection. Thus the deflection of the beam in a Porro resonator subject to misalignment is a function of the azimuthal angle α.

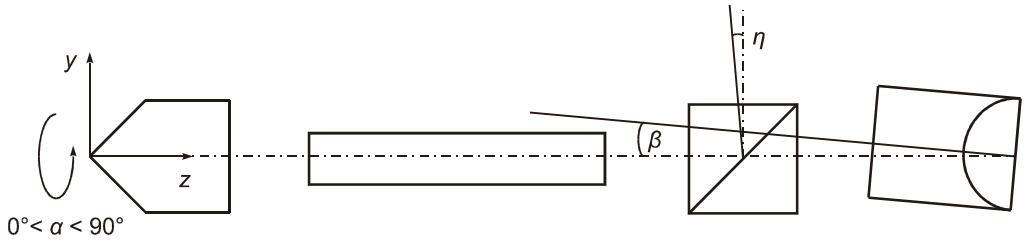

Figure 26 Misaligned Porro prism resonator

These geometrical techniques are also used to consider the effect of misalignment of one prism in a Porro prism resonator in three dimensions (*Lee & Leung* 1989a). If η and ζ are the tilt angles of the output beam in the horizontal (y) and vertical (x) directions, respectively then

$$\eta = -\beta \tag{3-2}$$

and

$$\xi = \arcsin\left[\frac{\cos\alpha\sin\beta}{\left(\cos^2\theta\sin^2\beta + \sin^2\theta\cos^2\beta\right)^{1/2}}\right] \quad \text{for } \beta \le 1°, \tag{3-3}$$

$$\cong \beta\cot\alpha \qquad \text{for } \beta << 1° \tag{3-4}$$

where α is the prism azimuthal angle, and β is the misalignment or tilt angle.

Figure 26 shows that the beam deflection is linear in the range of ±1°, which is typical, and that the deflection is much smaller than the misalignment angle.

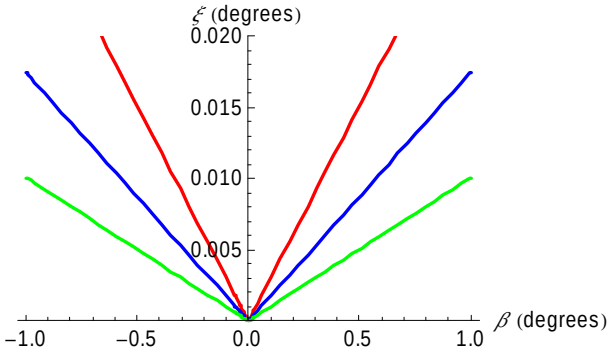

Figure 27 Plot of beam deflection angle ζ as a function of misalignment angle β for α = 30° (red), α = 45° (blue) and α = 60° (green).

For a resonator in multimode operation, the smaller mode volume is the only cause for the decrease of the output power, since additional diffraction losses are only generated if the fundamental mode gets clipped by the active medium.

3.5 Resonator stability

In a conventional Fabry-Perot resonator the stability of the resonator is determined by the radius of curvature on the mirrors. In a Porro resonator however the Porro prisms do not contribute any focusing power and so intracavity lenses may be included to determine the stability. A telescopic configuration is commonly used to tailor the beam size to match that of the active medium (*Hanna et al.* 1981).

Referring to Figure 28, in the general case that spaces exist between the intracavity lenses and the Porro prisms the ray transfer matrix M_{lens} given in (1-29) for a resonator consisting of two plane mirrors with intracavity lenses needs to be modified in the following way:

In Section 1.1 on pages 4-5 it was stated that an empty resonator with spherical mirrors and apertures can be analysed by replacing the spherical mirrors with plane mirrors and lenses, and unfolding the resonator. Since Porro prisms simply reflect a field (albeit with inversion about the prism apex), in a Porro prism resonator the Porro prisms can in turn be replaced by mirrors. This is illustrated in Figure 28.

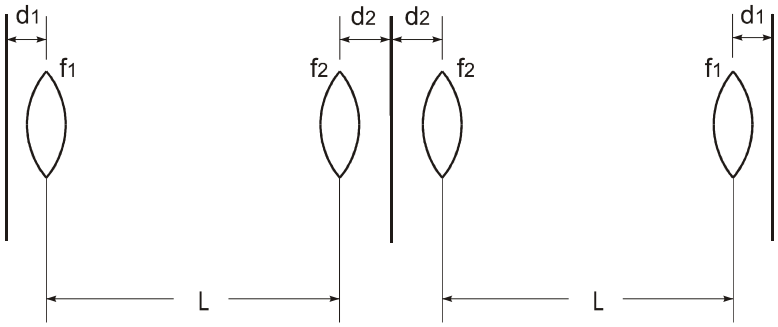

Figure 28 An unfolded representation of a Porro prism resonator.
Note the gaps d_1 and d_2 between the lenses and mirrors.

Following the approach given in (*Hanna et al.* 1981) the spaces d_1, d_2 are accounted for in the ray transfer matrix to give:

$$M_{Porro} = \begin{pmatrix} 1 & \frac{L}{2} \\ 0 & 1 \end{pmatrix} \begin{pmatrix} 1 & 0 \\ \frac{-1}{f_1} & 1 \end{pmatrix} \begin{pmatrix} 1 & d_1 \\ 0 & 1 \end{pmatrix} \begin{pmatrix} 1 & d_1 \\ 0 & 1 \end{pmatrix} \begin{pmatrix} 1 & 0 \\ \frac{-1}{f_1} & 1 \end{pmatrix} \begin{pmatrix} 1 & L \\ 0 & 1 \end{pmatrix} \begin{pmatrix} 1 & 0 \\ \frac{-1}{f_2} & 1 \end{pmatrix} \begin{pmatrix} 1 & d_2 \\ 0 & 1 \end{pmatrix} \begin{pmatrix} 1 & d_2 \\ 0 & 1 \end{pmatrix} \begin{pmatrix} 1 & 0 \\ \frac{-1}{f_2} & 1 \end{pmatrix} \begin{pmatrix} 1 & \frac{L}{2} \\ 0 & 1 \end{pmatrix} \tag{3-5}$$

where d_1, d_2, L, f_1, f_2 are shown in Figure 28.

The stability of the system can be calculated[3] using the stability function in Eq. (1-13):

$$\left| \frac{A+D}{2} \right| \leq 1. \tag{3-6}$$

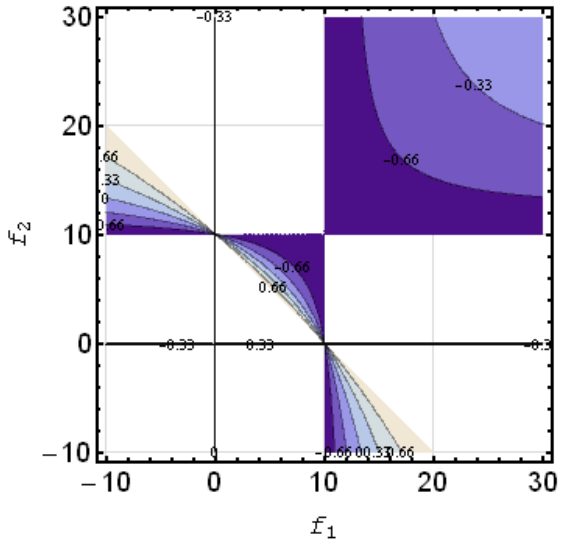

(a)

[3] The Mathematica code for the stability calculations can be found in Appendix 7.3.

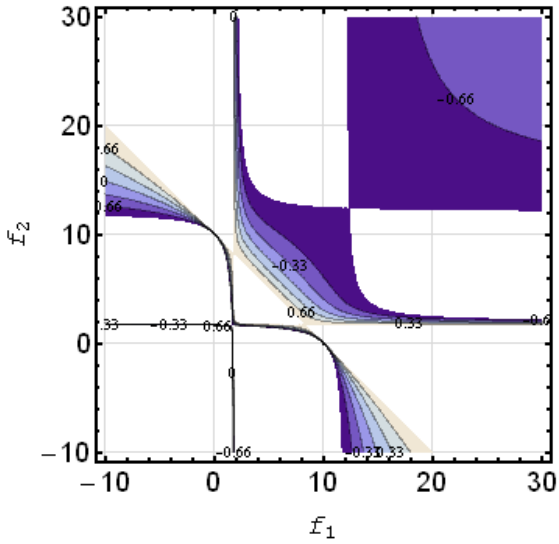

(b)

Figure 29 Plots of the stability function as a function of f_1 (x-axis) and f_2 (y-axis) (a) L = 10 cm, $d_1 = d_2 = 0$, and (b) L = 10 cm, $d_1 = d_2 = 2$ cm.

In Figure 29 the regions for which f_1 and f_2 give rise to stable resonators are plotted in shades of blue while the unstable regions are white. Note that the traditional stability plot is in terms of the g- (or G-) parameters, which are not defined when there are gaps between the focussing elements and the mirrors. Therefore these plots are in terms of the focal lengths f_1 and f_2. Figure 29 shows the influence of the spaces between the lenses and the mirrors or Porro prisms on the stability of the resonator. In Figure 29 (a), for example, the resonator with intracavity lenses with $f_1 = f_2 = 10$ cm is equivalent to a Fabry-Perot resonator with spherical mirrors with $R_1 = R_2 = 20$ cm and is marginally stable, whereas in Figure 29 (b) it is stable.

3.6 Out-coupling and polarization

The angle between the prism axes influences the beam stability as well as the polarization in the resonator, which in turn determines the amount of radiation coupled out of the resonator.

In a traditional mirror resonator the laser beam is coupled out through a partially transmitting output coupling mirror. In a Porro prism resonator, with both resonator mirrors replaced by roof prisms, output coupling is realized by polarization techniques using a polarizer. The orientation of the Porro prisms with respect to each other (or the angle between the apexes) affects the polarization within the resonator, and this angle is commonly adjusted in order to optimize the fraction of energy coupled out of the resonator. When a particular Porro angle is

required a retardation plate can be used to change the polarization fractions and allow the output coupling to be adjusted to its optimum value.

The Jones matrix method can be used to calculate the polarization shift experienced by a beam in a Porro prism resonator (*Chun & Teppo* 1976). The polarizer-Porro prism-polarizer matrix M_{prp} for a Porro prism orientated at a transmission angle (θ) of 0° is given (*Buchman* 1965; *Podgaetskii* 1969) by

$$M_{prp} = M_p M_r M_p$$

where $M_p = \begin{pmatrix} 1 & 0 \\ 0 & 0 \end{pmatrix}$ is the matrix for polarizer orientation of transmission axis $\theta = 0°$,

$M_r = \begin{pmatrix} A & iB \\ iB & A^* \end{pmatrix}$ is the matrix for the Porro prism, with

$A = \cos\left(\frac{P}{2}\right) + i\sin\left(\frac{P}{2}\right)\cos(2\beta)$, and

$B = \sin\left(\frac{P}{2}\right)\sin(2\alpha)$, and

P is the index dependent Porro prism internal phase shift angle, and

α is the azimuth angle of the Porro prisms.

So
$$M_{prp} = \begin{pmatrix} 1 & 0 \\ 0 & 0 \end{pmatrix}\begin{pmatrix} A & iB \\ iB & A^* \end{pmatrix}\begin{pmatrix} 1 & 0 \\ 0 & 0 \end{pmatrix}$$

$$= \begin{pmatrix} A \\ 0 \end{pmatrix}. \qquad (3\text{-}7)$$

For a Porro prism the phase shift P associated with total internal reflection is:

$$P = \pi + 4\tan^{-1}\left(\frac{\cos\gamma\left(\sin^2\gamma - \frac{1}{n^2}\right)^{\frac{1}{2}}}{\sin^2\gamma} \right) \qquad (3\text{-}8)$$

where γ is the incident angle, and n is the refractive index of the prism. Since a Porro prism roof angle is 90°, γ is 45°; thus, there is a finite phase shift when the refractive index is other than $\sqrt{2}$.

The effective reflectivity R_{eff} is then (*Chun & Teppo* 1976)

$$R_{eff} = M^{*}_{prp} M_{prp} = \cos^2\left(\frac{P}{2}\right) + \sin^2\left(\frac{P}{2}\right)\cos^2(2\alpha). \tag{3-9}$$

Figure 30 is a plot of the reflectivity R_{eff} as a function of azimuthal angle α for several values of refractive index n, and was plotted using Eqs. (3-8) and (3-9).

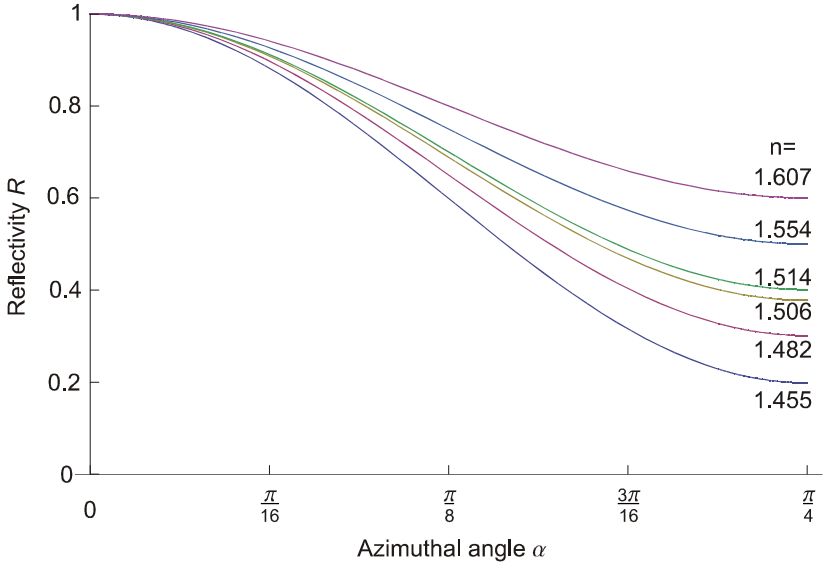

Figure 30 Plot of reflectivity R_{eff} as a function of the azimuthal angle α for several values of refractive index n.

4. TRANSVERSE MODES IN PORRO PRISM RESONATORS

4.1 Introduction

Beams with either radially-symmetric lobed (or "petal") patterns, or flattened doughnut patterns are reported to be characteristic of Porro prism lasers (*Nortier* 1981; *Preussler* 2007; *Steyl* 2007). Figure 31 (a) shows the lowest-order Hermite-Gaussian mode which, as will be discussed in the next section, was the beam structure predicted previously in the literature. Figure 31 (b) however shows the sort of mode which is commonly obtained experimentally from a Porro prism resonator where the number of spots or petals is a function of the rotation of the Porro prisms with respect to each other.

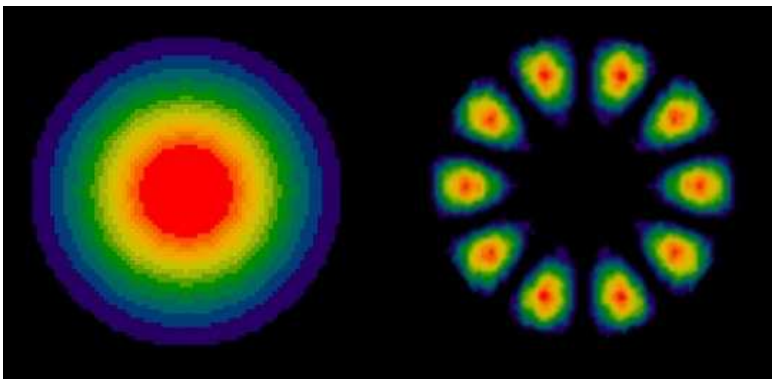

(a) (b)

Figure 31 (a) is the lowest-order Hermite-Gaussian mode pattern, the Gaussian beam, while (b) shows the type of modes typically observed from Porro prism resonators.

Despite the ubiquitous nature of these lasers in the field, for a long time the output modes from such lasers were not fully understood.

In early work a consideration of the theoretical properties of resonators with corner cube prisms specifically mentions the influence of bevels of finite width at the prism edges as a possible explanation for a tendency for distinct longitudinal sectors to oscillate independently, but does not go on to develop this idea into a model which could be used to explain experimental results (*Anan'ev* 1973).

A physical optics model which solves the Fresnel-Kirchoff integral equation for the case of a stable, large aperture roof mirror resonator concludes that Hermite-Gaussian modes can be

expected from them (see Figure 31 (a) for example) and therefore also fails to account for the true field pattern found from such resonators (*Zhou & Casperson* 1981). This is because only the optical path length experienced by the beam in the kernel of the Fresnel–Kirchoff diffraction integral is considered, thus treating the prism as though it were acting like a perfect mirror, with an identical ABCD matrix representation albeit incorporating the inverting properties of the prisms.

Zhou & Casperson's approach appears to be the preferred model for Porro prisms. The conclusion that Hermite-Gaussian modes can be expected from these lasers is used to investigate the time-dependence of the transverse mode in a theoretical and numerical model of a Porro prism resonator (*Chen et al.* 2006), and is also included in a textbook (*Hodgson & Weber* 2005, p.585-590), which states that the beam quality of the laser resonator is not affected by the prism. The chapter on Porro prism lasers also summarizes key findings of Porro prism resonators and proceeds to derive an expression for the reduced output power on misalignment in terms of the Porro angle, the displacement angle, and the gain and saturation parameters of the gain medium, but does not explain the complex transverse field patterns found in Porro prism resonators.

A comprehensive numerical model of a Q-switched Nd:YAG Porro prism laser is used to study pumping and gain, thermal effects, polarization and associated output coupling effects, and Q-switching (*Henriksson et al.* 2005; *Henriksson & Sjoeqvist* 2007). This model includes temporal effects, but the prisms are modelled with plane mirrors and do not predict the beam structure.

This is a recurring problem in the literature, with only a hint at a solution offered in (*Virnik et al.* 1987) and (*Anan'ev et al.* 1977), where it was proposed to treat the field patterns as a result of diffractive coupling between a linear combination of sub-resonators.

Clearly the approach of treating Porro prisms as simple plane mirrors (albeit having an effect on the intracavity polarization) is not sufficient to explain the beam structure observed from these lasers, and a deeper understanding of the field in the resonator requires an investigation as to how the properties of prisms differ from plane mirrors in a resonator, which could not be found in the literature. This gives rise to a new analytical model which accounts for diffraction losses not only at the limiting aperture, but also from the prism apexes.

We present a new approach (*Litvin, Burger & Forbes* 2007a; *Litvin, Burger & Forbes* 2007b), and are the first to consider the loss from the apex of the prisms. We include this as a

loss screen in a physical optical model of the Porro prism resonator, and also consider the conditions required for a field in a resonator to repeat back on itself. We predict a petal pattern beam (see Figure 31 (b)), where the number of petals (N) can be calculated for discrete values of the Porro angle. This new analytical model is tested and confirmed by including it in a numerical model, the output of which is in good agreement with the predicted mode patterns. These petal patterns were also observed experimentally at the predicted Porro angles.

The numerical model is then used to further investigate the mode patterns from a range of stable and unstable Porro prism resonators with large intracavity apertures (*Burger & Forbes* 2007; *Burger & Forbes* 2008a; *Burger & Forbes* 2008b). We discover that the higher-order modes of these resonators have a kaleidoscope pattern, and investigate the temporal development and characteristics of these modes. These modes are verified experimentally.

Further we make use of non–planar, unidirectional resonance analysis (*Bollig* 1997; *Bollig et al.* 1997; *Hodgeson & Weber* 2005; *Liu et al.* 2005) to understand the oscillating modes supported in these resonators. These higher-order modes bear close resemblance to recently reported kaleidoscope modes (*McDonald et al.* 2000; *Bouchal* 2003; *Anguiano-Morales et al.* 2008) which are named after the patterns formed in a kaleidoscope (*Brewster* 1819).

These similarities and the implications thereof are discussed in Section 4.5. This leads to the conclusion, in Section 4.6, that the petal–like modes hitherto reported are in fact only the lowest-order modes, while higher-order kaleidoscope modes are possible given sufficient transverse spatial extent to oscillate.

4.2 Analytical model

We propose that a “loss-screen” approach be used to model a resonator containing Porro prisms. The approach used is to describe the prisms as standard mirror elements, but with associated amplitude and phase screens, as illustrated in Figure 32. These screens act on the incoming field by modifying both its amplitude and phase by means of a suitable optical transfer function $t(x,y)$:

$$U_{out}(x,y) = U_{in}(x,y)t(x,y) = U_{in}(x,y)A(x,y)\exp(i\varphi(x,y)), \tag{4-1}$$

where $A(x,y)$ describes the amplitude effects, and $\varphi(x,y)$ describes the phase effects of the prism respectively.

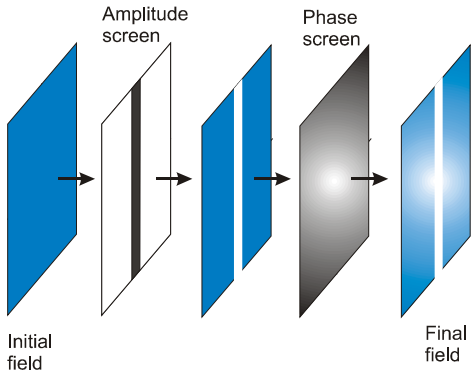

Figure 32 Illustration of the effect of phase and intensity screens on an incident field.

In the case of a Porro prism, the apex of each prism where the prism surfaces meet is never perfect, and the edge is always bevelled to some extent. This represents a narrow area of loss in the resonator. The amplitude screen introduces losses not only at the edges of the element (transverse confinement), but also at the bevel along the apex.

This bevel can be the a result of the machining process, and a typical specification is a width of $\leq 5\,\mu m$ (*CVI* 2009), but even a perfect prism would have a loss line at the intersection of the two surfaces. There is complete internal reflection on the reflective surfaces of the prism, but reflections of less than 100% at the apex as a result of the rounded or flat surface at the apex.

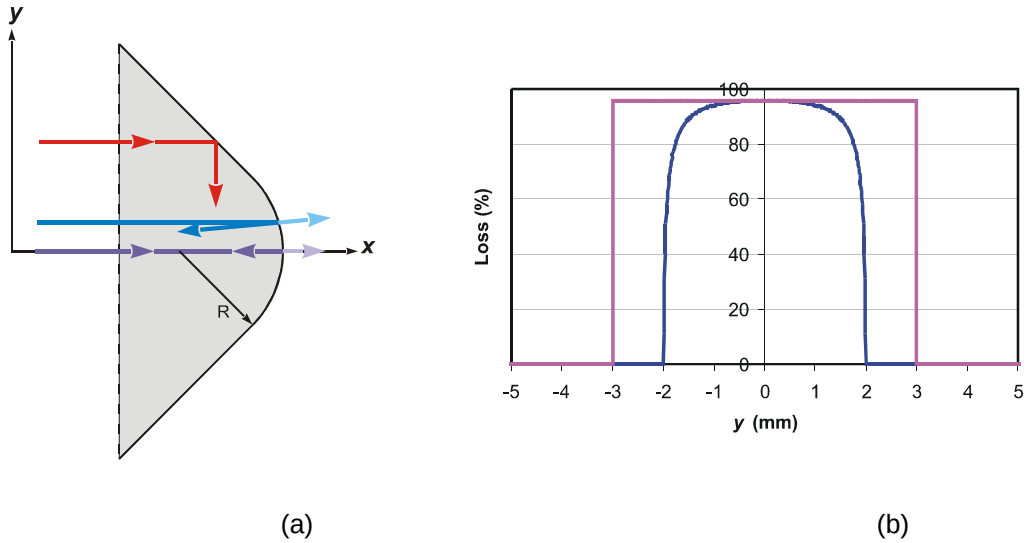

(a) (b)

Figure 33 (a) Sketch of the path of rays in the region of a rounded bevel. (b) Transmission (loss) at the apex of a Porro prism for a rounded bevel with radius 3 mm (blue) and for a flat bevel (purple). Note that for the rounded bevel, for |y| > 2 mm the loss is 0%. Similarly, for the flat bevel, for y > 3 mm the loss is 0%.

Figure 33 (a) is a schematic of a Porro prism, showing the partial reflection of the beam in the region of the apex or bevel. Figure 33 (b) shows the calculated transmission (loss) at the apex of a Porro prism for both a rounded and flat-edge bevel. The half-width of the bevel is taken to be 3 mm, which is much wider than would be found on a typical prism, but illustrates the point. The reflectivity is calculated purely using Snell's law for a BK7 prism (n = 1.50669 at 1064 nm) and shows that in the region of the bevel the transmission (or loss) is high, but drops to 0% on the prism faces where the beam experiences complete internal reflection. According to (*Hodgson & Weber* 2005, p.585-590), for high quality prisms, which exhibit edge widths of less than 5 μm, the additional loss per round trip is less than 0.5% overall. In this case, the extraction efficiency is as high as for a conventional resonator provided that the small-signal gain is chosen high enough.

Nevertheless, the bevel at the prism apex represents a narrow rectangular region of 100% loss across the centre of the field, and which has a small impact on the overall losses. The impact of the bevel on the mode will be shown.

The phase screen allows for the optical path length to vary as a function of the input position on the prism face, for example, to model errors in the prism angle or fabrication errors on the prism surfaces. With this approach, the diffractive effects of the prisms are taken into account, and the screens can be treated as intra–cavity elements that change the eigenmodes of a standard mirror–mirror resonator. Only the amplitude screen approach was used to model perfect prisms with high losses where the prism edges meet. With the prism orientated with the bevel vertical the loss area has the same height as the prism and the same width as the bevel, 2δ. The transfer function for the new prism model then includes only the amplitude effects,

$$t(x,y) = 1 \text{ for } |x| \leq \delta \qquad (4\text{-}2)$$

$$0 \text{ for } x > \delta.$$

This loss function describes a high loss region along the apex of the prism, with 100% losses, and no losses elsewhere within the clear aperture of the element.

4.2.1 The "loss-screen" approach

The following section shows the effect of this new transfer function on the structure of the emergent beam.

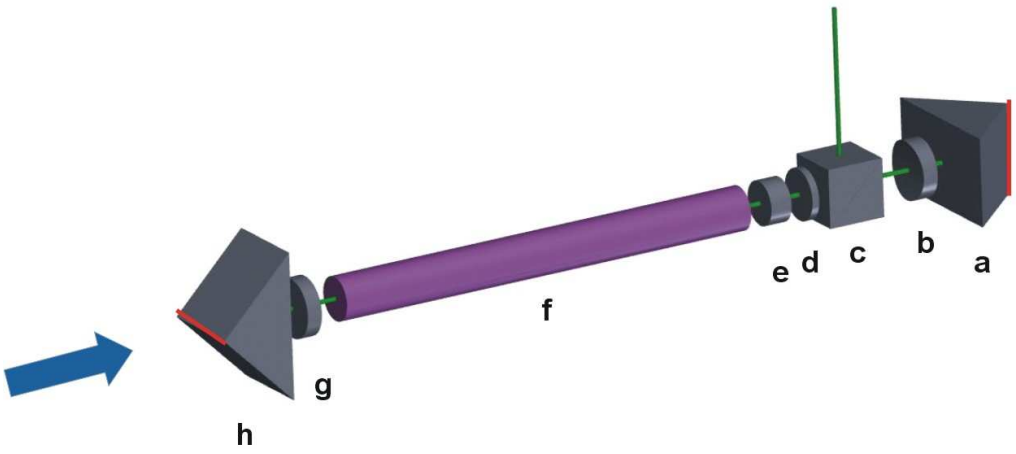

Figure 34 A typical Porro prism based Nd:YAG laser with passive Q–switch, showing the following optical elements: Porro prisms (elements a and h); intra–cavity lenses (elements b and g); a beamsplitter cube (element c); a quarter wave plate (element d), and a passive Q–switch (element e).

Referring to Figure 34, and considering for the moment only the two Porro prisms and their impact on the propagating field, imagine viewing the resonator along its length from one prism (element **h**) looking towards the other (element **a**). On encountering a prism, the field inverts itself around the prism apex, and reverses its propagation direction, travelling back towards the opposite prism. The same inversion and reversing of propagation direction takes place again, and this sequence repeats on each pass. The prisms would essentially be treated as perfect mirrors but with a field inverting property.

A geometric approach is useful in understanding the symmetry and repeatability of the resonator modes: consider a propagating ray viewed along the optical axis and assume, without any loss of generality, that the Porro prism (PP) closest to the observer has its apex in the horizontal plane, while the opposite PP has its apex rotated at some angle α from the horizontal, referred to henceforth as the *Porro angle*. By way of example, consider the case of $\alpha = 60°$, as illustrated in Figure 35 (a) – (e). In the analysis to follow the pertinent information is the location of the prism apexes, which is illustrated as solid lines 1 and 2 in Figure 35, corresponding to elements **h** and **a** in Figure 34 respectively.

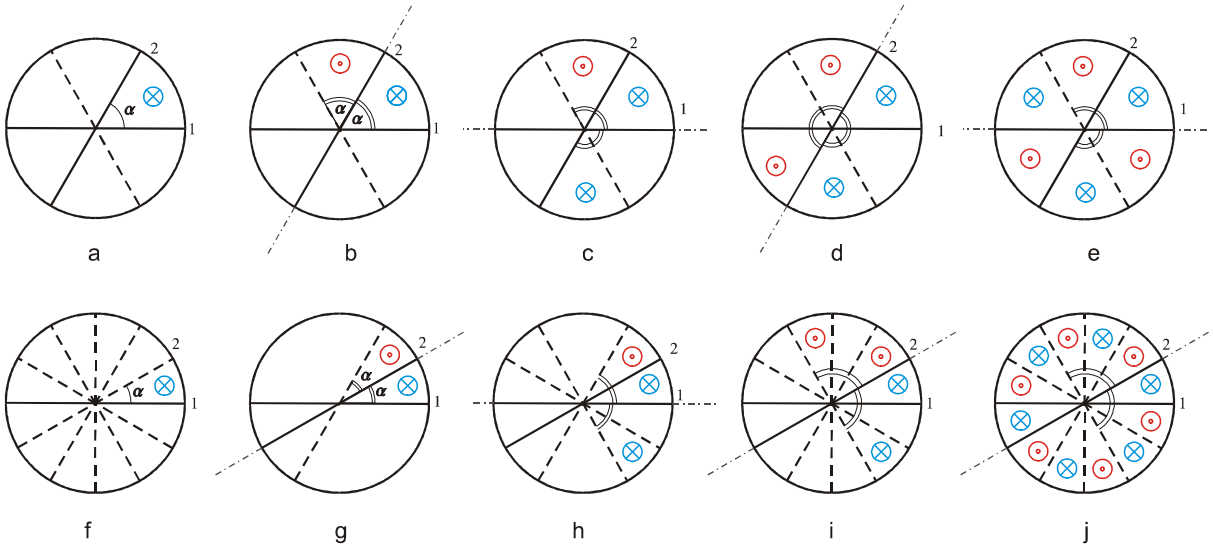

Figure 35 (a) – (e): Evolution of a ray as it is reflected back and forth in the resonator, for starting Porro angle $\alpha = 60°$. After 3 round trips the pattern is complete (e) and starts to repeat. (f) – (j): Equivalent case but with $\alpha = 30°$, and now taking 6 round trips for completion .

Having *a priori* knowledge of how the mode will develop, consider a starting ray located as shown in Figure 35 (a), travelling away from the viewer towards PP 2. This location was chosen based on the assumption of high loss along the apexes, thus avoiding the apex zones. At PP 2 the ray is inverted about the prism apex (PP 2), and travels back towards the viewer parallel to the optical axis as indicated in Figure 35 (b). At PP 1, the ray is inverted about the axis of prism 1, and travels back towards PP 2 (Figure 35 (c)). This process continues until the complete pattern is created (Figure 35 (e)), and the ray has returned to its starting position. This happens after three round trips. Clearly subsequent reflections simply duplicate the pattern. A second example is shown in Figure 35 (f) – (j), where the case of $\alpha = 30°$ is illustrated. The same propagation rules apply so that eventually, after six complete round trips the pattern starts repeating itself. By dividing the field into equal sectors this approach correctly predicts the petal pattern formation often observed from such lasers, but this is a “ray” picture based on *a priori* knowledge and not physical reasoning. Also, this approach is only useful for limited Porro angles.

An alternative approach, which is more useful in modelling such a resonator, is to consider that since losses are introduced onto the field from each prism apex, and the field is then inverted, one can view the situation as the amplitude screen being inverted after each prism reflection. From the viewpoint of the field travelling inside the resonator, the equivalent picture is that of the field remaining inversion free, while the prisms edges invert after each pass, essentially appearing to rotate by an amount dependent on the Porro angle, and hence the main

area of losses (the apex edges) also appear to rotate. An example of this rotation is shown in Figure 36.

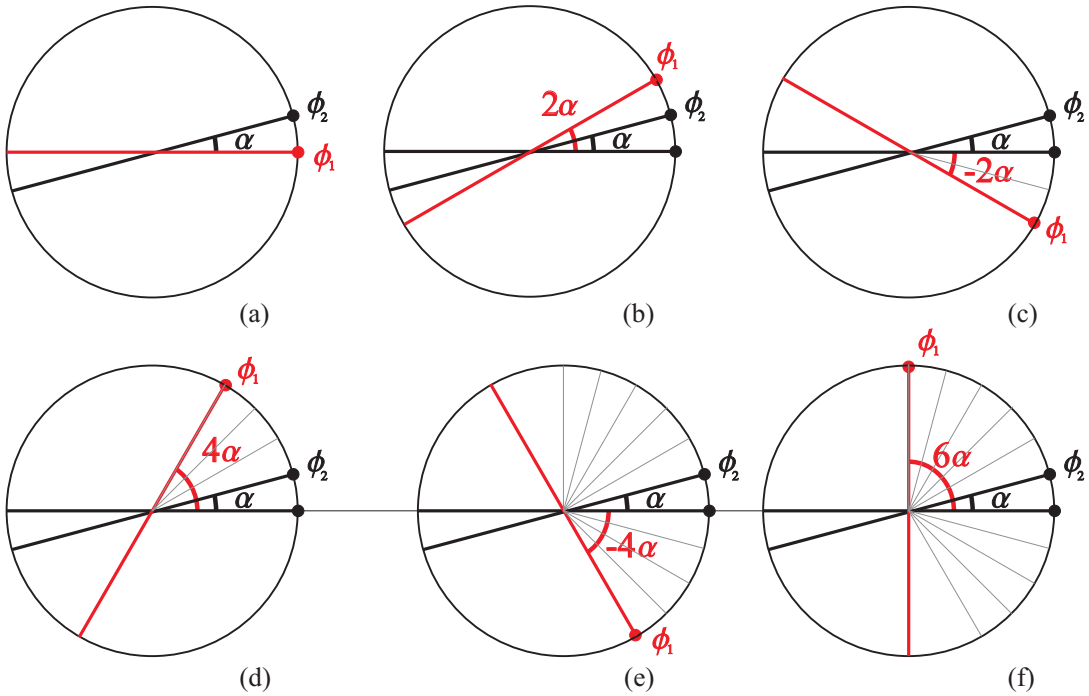

Figure 36 The apexes of two Porro prisms at angles ϕ_1 and ϕ_2. Initially the apex of PP 1 is in the horizontal plane (a), but after successive reflections about the inverting edges of the two prisms the apex will appear to be rotating about the circle: (b) 1 pass, (c) 2 passes and (d) 3 passes (e) 4 passes (f) 5 passes.

In order to develop a physical optics model based on this approach, expressions are needed for the equivalent picture of the rotating prism apexes (high loss areas). Consider the rotation of the first PP apex, denoted with the subscript 1, whose position on the circle in Figure 36 is described by the vector $v_1 = (x_1, y_1)$ with angular displacement given by ϕ_1. The region of high loss is then simply a line passing through the origin with slope y_1/x_1. Without any loss of generality it is assumed that the resonator is viewed such that the first PP has an edge parallel to the horizontal axis, with the second PP rotated at the Porro angle α, as illustrated in Figure 34.

Referring to Figure 36, and considering only the position of apex 1:

(a) This is the initial position of v_1 relative to v_2, as viewed along the resonator axis.

(b) After one reflection (about axis 2) v_1 appears to have rotated through an angle of $+\alpha+\alpha=+2\alpha$; $\phi_1=+2\alpha$.

(c) On a return trip a second reflection about axis 1 results in v_1 appearing to have rotated through an angle of $-2\alpha-2\alpha=-4\alpha$; $\phi_1=-2\alpha$.

(d) After a third reflection (about axis 2) v_1 appears to have rotated through an angle of $+3\alpha+3\alpha=+6\alpha$; $\phi_1=+4\alpha$.

(e) After a fourth reflection (about axis 1) v_1 appears to have rotated through an angle of $-4\alpha-4\alpha=-8\alpha$; $\phi_1=-4\alpha$.

(f) After a fifth reflection (about axis 2) v_1 appears to have rotated through an angle of $+5\alpha+5\alpha=+10\alpha$; $\phi_1=+6\alpha$.

In general then, after n reflections this vector has rotated through an angle $\theta_1(n)$ given by:

$$\theta_1(n)=(-1)^{n+1}2n\alpha, \tag{4-3}$$

where α is the Porro angle, and the angular position of this vector after n reflections can be found from:

$$\phi_1(n)=\sum_{i=0}^{n}\theta_1(i)=\frac{\alpha}{2}\left[1-(-1)^n(1+2n)\right]. \tag{4-4}$$

Prior to any reflections the apex of the first prism is at $\phi_1(0)=0$, so that if we imagine the apexes rotating about the unit circle, then the vector $v_1(n)$ may be expressed as:

$$v_1(n)=\begin{pmatrix}\cos\phi_1(n) & -\sin\phi_1(n)\\ \sin\phi_1(n) & \cos\phi_1(n)\end{pmatrix}\begin{pmatrix}1\\0\end{pmatrix}. \tag{4-5}$$

Similar expressions can be derived for the second PP apex:

$$\theta_2(n)=(-1)^n 2n\alpha; \tag{4-6}$$

$$\phi_2(n)=\alpha-\frac{\alpha}{2}\left[1-(-1)^n(1+2n)\right]; \tag{4-7}$$

$$v_2(n)=\begin{pmatrix}\cos\phi_2(n) & -\sin\phi_2(n)\\ \sin\phi_2(n) & \cos\phi_2(n)\end{pmatrix}\begin{pmatrix}1\\0\end{pmatrix}. \tag{4-8}$$

Note that the notation has been selected so that the initial positions of the two apexes are given by:

$$v_1(0)=\begin{pmatrix}1\\0\end{pmatrix}, \tag{4-9a}$$

$$v_2(0)=\begin{pmatrix}\cos\alpha\\ \sin\alpha\end{pmatrix}, \tag{4-9b}$$

with corresponding initial apex loss regions along $y_1 = 0$ and $y_2 = (\tan\alpha)\, x_2$ respectively.

Recall Eq. (1-8) $$M\,\underline{r} = \lambda \underline{r}\,.$$

This is the eigenequation of a ray $\underline{r}$ in a resonator with ray transfer matrix M.

This is a statement of the necessary condition for resonance. If the resonator is stable, then the eigenvalues λ are complex and imply an inherent periodicity, as shown in Section 2.3, pages 27-31, and imply that after a certain number of round trips the ray will repeat on itself. A consequence of this is that since the transformation matrix M is a function of the Porro angle, the condition implied by Eq. (1-8) will only be met at some discrete starting angles at which the rotating edges repeat on themselves. At these angles the field is finitely sub–divided by the prisms losses, and it takes a certain number of passes for the sub–division of the field to be complete. The resulting field is then made up of a circular pattern of spots which we refer to as petals or as a petal pattern. At other angles, the edges never repeat on themselves, thus infinitely sub–dividing the field. With this formalism we are able to find the angles α at which these repeating patterns manifest themselves, as well as the number of sub–divisions (or equivalent, number of petals) that will be observed. Consider for example the first Porro prism apex. It will return on itself when $v_1(n) = v_1(0)$, which leads from Eq. (4-5) to the relation:

$$\begin{pmatrix} \cos\phi_1(n) & -\sin\phi_1(n) \\ \sin\phi_1(n) & \cos\phi_1(n) \end{pmatrix} = \begin{pmatrix} 1 & 0 \\ 0 & 1 \end{pmatrix}. \tag{4-10}$$

This will be true when

$$\phi_1(n) = \frac{\alpha}{2}\left[1-(-1)^n(1+2n)\right] = i2\pi\,, \tag{4-11}$$

for any integer i.

Solve for α: $$\alpha = \frac{i4\pi}{1-(-1)^n(1+2n)}$$

To select only the positive solutions for α, let $n = 2m$, where m is any integer.

Now $$\alpha = \frac{i4\pi}{1-(-1)^{2m}(1+4m)}\,,$$

which becomes $$\alpha = \frac{i\pi}{m} \tag{4-12}$$

for any positive integers i and m

Thus we have derived a simple expression for the initial angles α that will lead to a finitely sub–divided field (or repeating pattern from the geometric viewpoint):

The same result can be derived by starting from vector v_2. The implication is that only at these specific angles α will the field be finitely sub–divided, thus leading to some regions with low loss for lasing. In addition, since the position of these sub–divisions remains stable (i.e., they repeat on themselves) after a certain number of round trips, the modal pattern that oscillates inside such a resonator will give rise to a petal pattern *only* at those angles given by Equation (4-12). At other Porro angles the high loss apexes will continuously rotate to new positions, thus resulting in high losses across the entire field.

We can now go on to calculate how many petals will be observed for a given Porro angle α. The number of petals will be equal to the number of sub–divisions of the field, but the field may not be completely sub–divided in one complete rotation of the vector; it may take several complete rotations for this to happen. Note that the sub–divisions will not necessarily be equal to the Porro angle; when several rotations are needed to complete the sub–divisions, it is likely that the area between the initial apexes will be sub–divided further. In general the following expression relating the Porro angle to the total number of sub–divisions (petals) of the field can be written:

$$\frac{\alpha}{j} = \frac{2\pi}{N}. \tag{4-13}$$

The validity of this is evident from the following heuristic argument: The complete circle (2π) divided by the total number of sub–divisions N must return the angle of each sub–division. If the sub–division is completed in one rotation, then the sub–division angle will equal α, but if more complete rotations are needed, then this will result in α itself being sub–divided by integer amount, j. Thus both the left and rand hand sides of Eq. (4-13) represent the same quantity – the final angle of each sub–division. A simple rearrangement of this equation then yields:

$$N = \frac{j2\pi}{\alpha}. \tag{4-14}$$

Since each reflection may only increase the number of sub–divisions in multiples of two, we deduce that N must be an even number. The positive integer j now appears to take on the meaning of the number of complete cycles required to return the apexes back onto one another. At present we cannot offer a simple analytical method of determining j, but can offer the following conditions: (i) j is the lowest positive integer such that N is even, and (ii) $j \leq i$.

Equations (4-12) and (4-14) are new predictions as to which initial angles α will result in stable petal pattern output, and how many petals N will be observed in the pattern respectively. A plot of the allowed angles for petal pattern formation together with the number of petals that will be observed is shown in Figure 37.

Since the sub–divisions divide the circle finitely, the angle subtended by each sub–division is given by:

$$\psi = \frac{2\pi}{N} = \frac{\alpha}{j}. \tag{4-15}$$

Thus the more complete rotations needed to complete the pattern, the smaller the angle of each sub–division. The simplest case is when $i = 1$; then $j = 1$ and the circle is divided into divisions of α. For higher j values the lossless regions between the high loss sub–division lines become small. Thus although there is an infinite number of solutions for α that lead to finite sub–divisions of the field, if the number of divisions is too large, diffraction will blur the spot structure and no petal pattern will be observed.

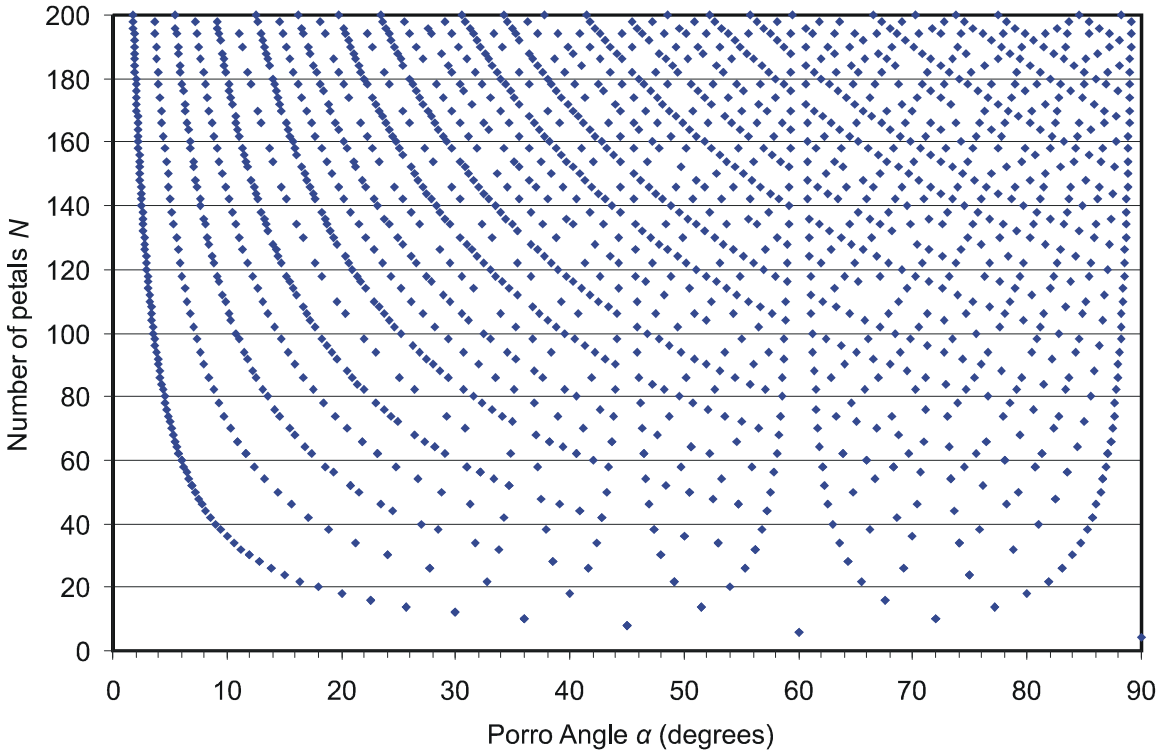

Figure 37 Plot of the discrete set of angles α that give rise to a petal pattern, with the corresponding number of petals to be observed. Data calculated for $j \in$ [1,100] and $i \in$ [1,50].

Taking this into account, and considering the diffraction of a field propagating between areas of high losses, it is reasonable to suppose that the approach and theory presented here is the explanation for the observed (and sometimes not observed) petal patterns from Porro prism resonators. The governing equations for the onset of petal patterns and the number of petals observed are given by Eqs. (4-12) and (4-14) respectively.

4.3 Numerical model

The first step in writing a numerical model for a Porro prism resonator is to interpret the optical components in the resonator.

The laser was modelled[4] by successive passes through a folded–out resonator following the approach described in Section 1.1 on page 9 and using the Prony method (*Siegman & Miller* 1970; *Siegman* 1986).

Since the Fabry-Perot resonator equivalent to any Porro resonator can be found and described in terms of a ray transfer matrix, it was decided to simplify the model and use lens-mirror distances d_1=0 and d_2=0, and also to use a symmetric configuration with $f_1 = f_2 = f$. Then, using the equivalence of lenses and spherical mirrors and from (1-25) above, the G- or stability parameters in (1-27) can be calculated for a resonator containing identical intracavity lenses:

$$G = g_1 = g_2 = 1 - \frac{L}{2f}. \tag{4-16}$$

And, to reiterate Equation (1-28): $$N_F = \frac{a^2}{\lambda L}. \tag{4-17}$$

In this case the Porro ray transfer matrix M reduces to:

$$M = \begin{pmatrix} 1 & \frac{1}{2}L \\ 0 & 1 \end{pmatrix} \begin{pmatrix} 1 & 0 \\ -f^{-1} & 1 \end{pmatrix} \begin{pmatrix} 1 & 0 \\ -f^{-1} & 1 \end{pmatrix} \begin{pmatrix} 1 & L \\ 0 & 1 \end{pmatrix} \begin{pmatrix} 1 & 0 \\ -f^{-1} & 1 \end{pmatrix} \begin{pmatrix} 1 & 0 \\ -f^{-1} & 1 \end{pmatrix} \begin{pmatrix} 1 & \frac{1}{2}L \\ 0 & 1 \end{pmatrix}. \tag{4-18}$$

The model uses diffractive optics numerical techniques (*Lawrence* 1987; *Lawrence* 1991) and simulates a beam travelling in a symmetric resonator from laser switch-on and over any number of round trips. A single beam is defined on a square field of 0.4 x 0.4 cm, using a beam array size of 256×256.

[4] The GLAD code for the Porro prism resonator can be found in Appendix 7.4.

In the model each prism was assumed to be equivalent to a perfect flat mirror superimposed on a rotating loss line (see Figure 36), with the rotation of the loss region for prism 1 given by Eq. (4-4) and that for prism 2 by Eq. (4-7). The mirrors were separated by a distance L, and the resonator contained two intracavity lenses of focal length f located at the mirrors. Apertures located at the mirrors defined the clear or limiting aperture a of the resonator. The resonator contained no gain medium, absorption losses or loss due to radiation coupled out of the resonator, so that the only losses considered were the losses at the apertures and the rotating loss lines. The initial beam was randomly generated noise, and the gain was simulated by recording and then resetting the energy to unity after each round trip, giving the loss per round trip due only to diffraction. Typically the modal build–up data was recorded until the loss per round trip stabilized to within 0.5%.

A diagnostics subroutine characterises the beam, and on each round trip the aperture size, spot sizes and the beam quality or M^2 in the x- and y-directions[5] as well as the loss are written to a text file for analysis. The beam pattern is taken at prism 1, and can be recorded after each round trip in order to visualise the changes in intensity distribution; it proved useful to record sequences of beam patterns at various stages of mode development.

In keeping with the available experimental laser the following parameters were used:

- L = 10 cm
- λ = 1.064 μm
- f was varied from -1000 to 60 cm which corresponds to g-values of -1 to 1.2 (shown in Figure 38)
- a was varied from 0.04 to 0.12 cm, which corresponds to N_f - values of 1.5 to 13.5
- a prism bevel width of 0.002 cm was used.

[5] The code used in the verification of GLAD's M^2 calculations are given in Appendix 7.5.

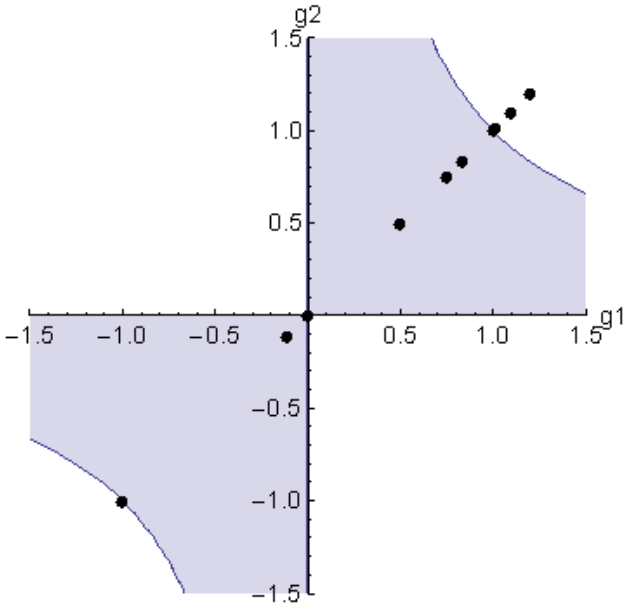

Figure 38 Plot showing the stability of the *g*- values used in the numerical model.

4.3.1 Mode patterns

The numerical model was used for extensive tests on the analytical predictions of Section 4.2. A marginally stable resonator with no intracavity lenses ("flat-flat") was modelled because this configuration does not exhibit any higher-order transverse modes.

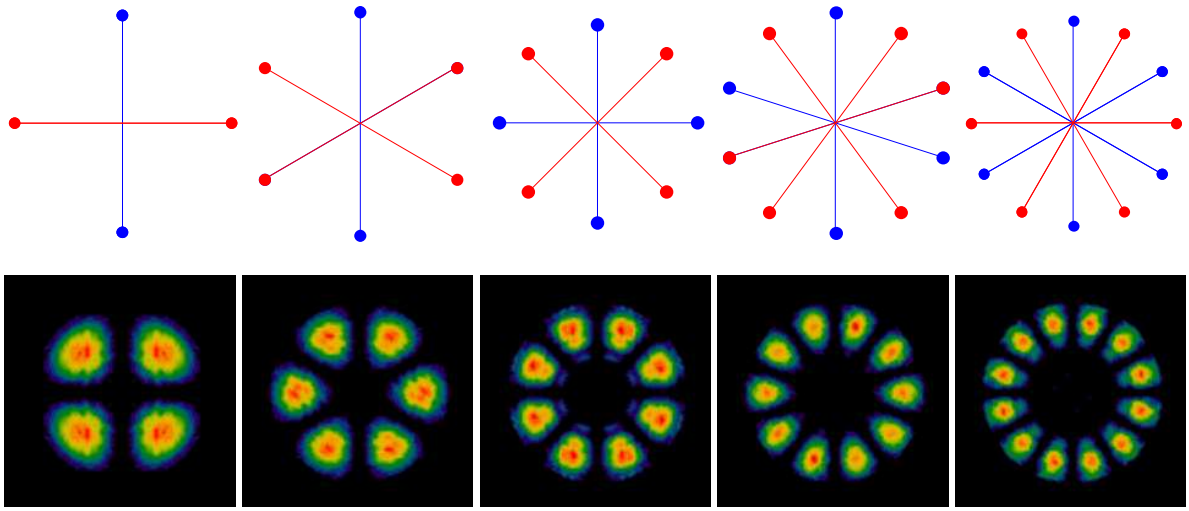

Figure 39 Analytically calculated sub–division of the field using Equations (4-4) and (4-7) (top row), with corresponding petal patterns calculated numerically using this model, with α = 90°, 60°, 45°, 36° and 30° respectively.

Figure 39 shows examples of some results of resonators with $g = G = 1$ and identical N_F, with the analytical prediction of the stabilized sub–division of the field shown in the top row, with corresponding petal patterns calculated numerically shown below. The top row of Figure 39 shows the calculated apex positions after rotation by Equations (4-4) and (4-7), and after a stable pattern has emerged. The numerical model correctly predicts the following features of the petal pattern:

- The number of petals is correctly predicted by (4-14).
- The prism apexes coincide with the zero-intensity areas between the petals.

Related work (*Forbes, Burger & Litvin* 2006) shows that the brightness of Porro resonator beams is strongly influenced by the angle between the two prism edges, and that at those angles at which petal patterns are observed one finds an increase in the laser brightness relative to nearby non-petal pattern generating angles, and that there also appears to be a trend towards improved brightness and beam quality for those angles at which fewer petals are generated.

The numerical model was used to further investigate the properties of these resonators. Both the lens focal lengths f, and the aperture radius a were varied in order to investigate the impact of resonator stability G given in (4-16) and effective Fresnel number N_F given in (4-17) on the oscillating modes.

The first observation is that unstable resonators do not generate repeating petal–like patterns, while stable resonators do. To preempt our discussion to follow later with the following geometrical optics argument: a ray traversing the resonator must return to a loss–free sub–division in order to create the complete petal pattern. The lack of ray repeatability and confinement in an unstable resonator precludes this from happening, and hence only stable resonators exhibit the petal–like modes. Loss as a mechanism to explain this observation can further be eliminated in that the loss for both stable and unstable resonators was set arbitrarily in this study and yet did not influence the observation of petals, or the lack thereof. The discussion to follow will therefore concentrate on stable resonators only. Without any loss of generality, all spatial modes to follow are calculated at the face of one of the Porro prisms, and may be propagated to any other plane if so desired.

The following data is typical of that obtained from the numerical model and can be used to characterise a Porro prism resonator. Although the characteristics described apply to some

extent to all Porro prism resonators, configurations which best illustrate the characteristic under discussion are presented.

Consider by way of example three stable resonators chosen so that G = 0.75 and with Porro angles (α) of 60°, 45° and 30° respectively. When the intracavity aperture is very small (N_F ~ 1.5), no mode is able to resonate (crossed out mode patterns in Fig. 40, 41). At intermediate aperture sizes (N_F ~ 3.5) the conventional petal–like modes are observed, with 6, 8 and 12 petals for α = 60°, 45° and 30° respectively. At large aperture sizes (N_F > 6) the petal–like modes give way to more complex mode patterns which we call kaleidoscope modes after their resemblance to the patterns produced by the optical toy, the kaleidoscope. This increase in mode complexity as the aperture size increases suggests that the petal–like modes are in fact the lowest-order modes of Porro prism resonators, while previously unreported higher-order kaleidoscope modes also exist, and can be made to resonate if given sufficiently large transverse freedom. These results are shown in Figure 40.

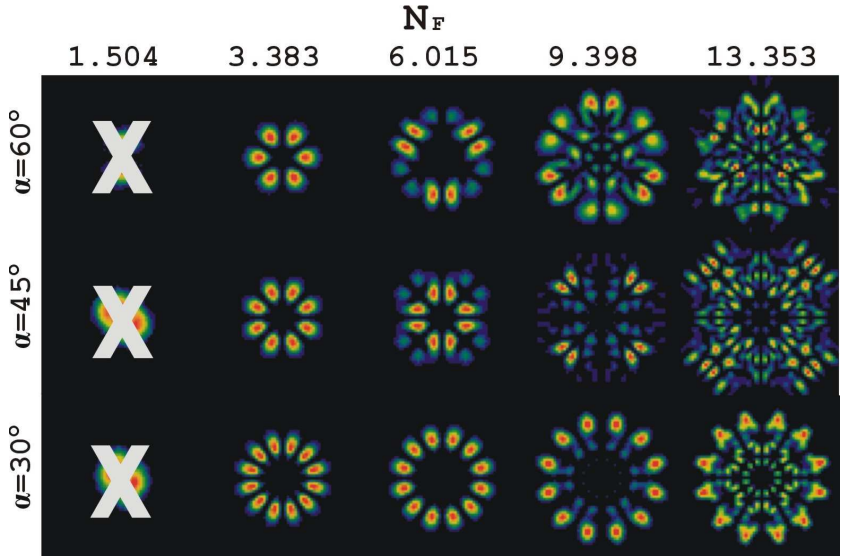

Figure 40 Modal patterns for three Porro angles with increasing effective Fresnel number to the right in each row. As N_F is increased (through an increase in aperture size), the modes become more complex, departing from the petal–like standard.

Porro prism resonators appear to offer a rich landscape of possible modes, many of which have not been associated with this type of resonator previously. While the previous discussion focused on one particular resonator for three Porro angles, we illustrate in Figure 41 that the resonator parameter G also influences the oscillating mode, as one might expect.

While the results are illustrated for α = 45°, similar results are found at other Porro angles.

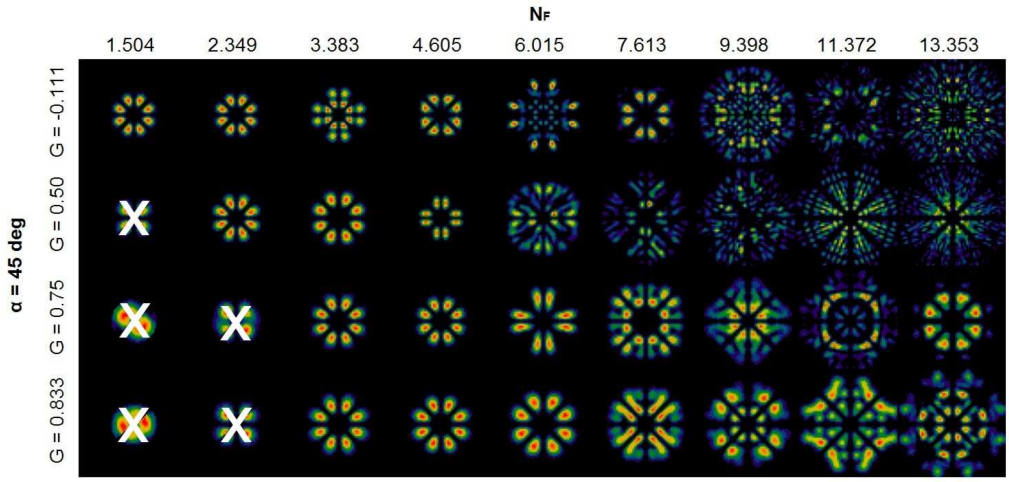

Figure 41 The output modes of a number of Porro prism resonators arranged as a function of *G* (rows) and N_F (columns). Note that in the petal–like cases the single repeating mode is shown, while in the higher-order mode cases, only one of the oscillating modes is shown.

4.3.2 Mode Periodicity

The higher-order kaleidoscope modes depicted in Figure 40 and Figure 41 exhibit an interesting feature: they repeat after a fixed number of passes through the resonator. This periodicity is not a function of the Porro angle α but rather of *G*, and is the result of the resonator's complex eigenvalues.

Figure 42 shows the spot size ω as a function of the number of round trips *p*, so also as a function of time. The spot size ω_x (component in the *x*-direction) is shown, but the modes are radially symmetrical, so the *y*-values are identical. The spot sizes ω_x and ω_y are calculated with the Second Moment Method described in Section 1.1 on pages 16-17 above. The periodicity in the region of $p = 2000$ is shown in the insert, with the associated modes patterns.

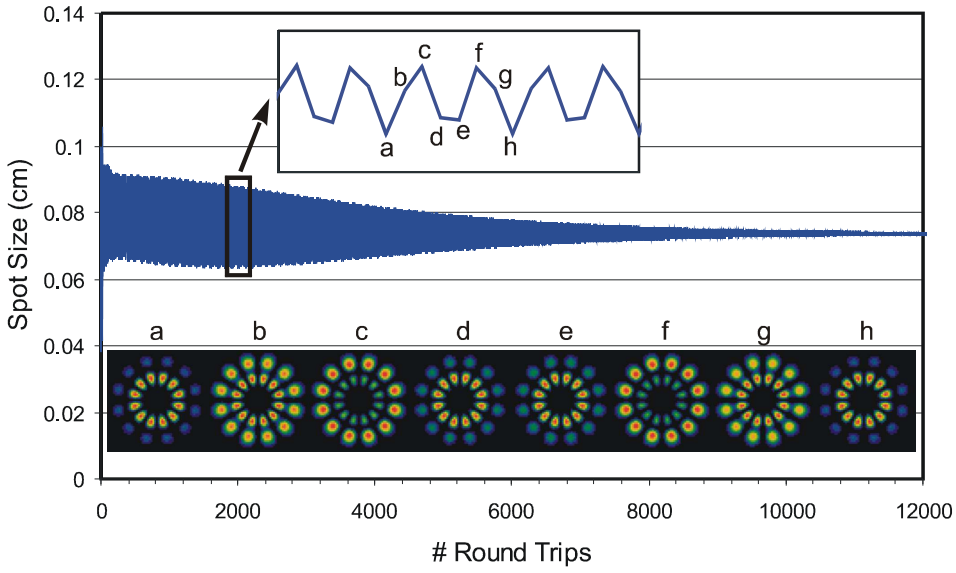

Figure 42 Plot of spot size for 12 000 round trips (double passes) through a resonator with Porro angle 30° for $G = 0.9$, $N_F = 9.4$, illustrating the periodic nature of the spot size and showing eventual convergence. The sequence of modes through one period is also shown.

This periodicity can be defined as the number of conventional round trips (double passes) required for any ray to return to an initial position and orientation, and can be found using geometrical ray analysis. Following the periodicity analysis in Section 2.3 on pages 27 - 31, if the Porro resonator matrix M is given by (4-18) then an initial ray, which can be thought of as any element of a mode pattern, can be written as a two–row vector $\underline{r}_0$ describing both the position and angular deviation of the ray. After p round trips through the resonator, $\underline{r}_0$ will be transformed into a new vector $\underline{r}_p$ according to:

$$\underline{r}_p = M^p \underline{r}_0 = \sum_i \lambda_i^p \beta_i \underline{r}_i , \qquad (4\text{-}19)$$

where λ_i and $\underline{r}_i$ are the eigenvalues and eigenvectors of the matrix M respectively and β_i are the coefficients required for the expansion of r_0 in terms of the eigenvectors. For repeatability of the mode we require $\underline{r}_p = \underline{r}_0$, found from the solution to the simultaneous equations (for each i) $\lambda_i^p = 1$. Using the Porro resonator matrix M and following the approach given in Section 2.3[6] in Eqns (2-4) to (2-11), the periodicity of the Porro resonator is found to be a function of the stability parameter G, and given by:

[6] Mathematica code to determine periodicity for Porro resonators is given in Appendix 7.6.

$$P = 0, \frac{2\pi}{\theta}, \frac{4\pi}{\theta}, \ldots \tag{4-20}$$

where P is the periodicity and number of round trips, and *must* be a *whole number*, and, as in Eq. (2-9) in Section 2.3:

$$\theta = \arccos(2G^2 - 1) \tag{4-21}$$

where G is given in (4-16). This is the same expression as was derived in (2-9), and is expected since the Fabry-Perot and Porro resonators are identical if $R = 2f$.

As in Section 2.3 on pages 27 - 31, $\underline{r}_p$ can be plotted as a function of p. In the following graphs the ray position y is plotted:

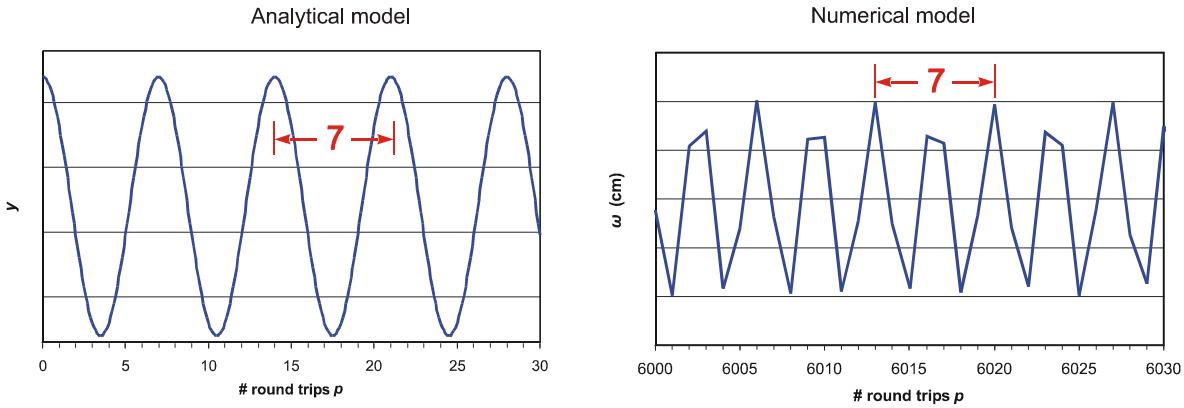

Figure 43 Comparison of Numerical and Analytical models of resonator with $G = 0.9$, with identical periodicity ($P = 7$) in both cases.

Figure 43 shows the periodicity from the numerical model for a resonator corresponding to the analytical or eigenmode model for the case of $P = 7$. For Porro resonators as with Fabry-Perot resonators, for all resonators corresponding to whole-number P-values (for $P > 2$), the periodicity of the numerical model was found to exactly match that of the analytical model.

This approach allows the periodicity of the cycling modes to be determined analytically, and compared to the periodic pattern observed in the spot size data from the numerical model. The results are illustrated graphically in Figure 43, as well as in Table 5.

Table 5 Periodicity comparison

G	***P***	
	Theory	*Model*
-1.0	none	none
0.0	none	none
0.5	3	3
0.707	4	4
0.809	5	5
0.867	6	6
0.9	7	7
0.924	8	8
0.94	9	9

Table 5 shows the agreement in periodicity predicted by geometric resonator theory compared to that observed in the numerical model for the beam loop modes.

One can understand this periodicity if one considers the similarities to the well–known Herriot cell resonator (*Hodgson & Weber* 2005) and by following the path of a ray through the resonator. Such resonators result in a periodicity that is not a double pass through the resonator, as is the case in a standard Fabry–Perot system, but rather is based on a uni–directional analysis, where the number of passes can be made very large for a complete “round trip” – in this case “round trip” refers to the condition that the beam repeats a previous path through the resonator. The number of reflections and the orientation of the beam, and hence the periodicity of the resonator, can be controlled by judicious choice of the resonator parameters. This concept is illustrated in Figure 44 where a standard resonator is operated as a non–planar ring laser (*Liu et al.* 2005). In this case the beam passes through the resonator six times (or reflects off each mirror three times) in a single “round trip”.

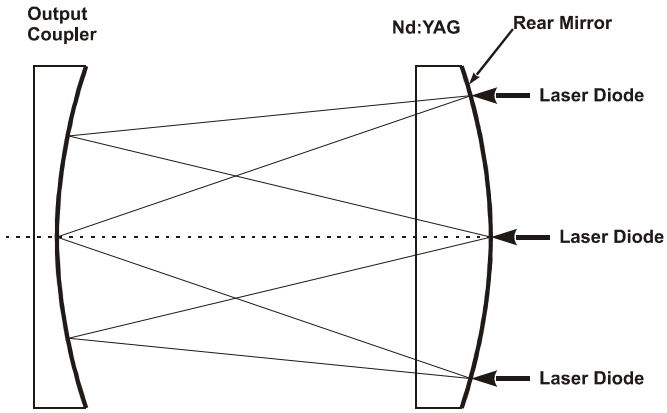

Figure 44 A multi–pass beam pass is possible for a given resonator configuration. If the gain region is small and central then a Gaussian mode is expected. The resonator can be forced into a higher multi–pass mode by off–centre pumping.

Such a configuration leads to a complex output beam pattern based on the possible beam paths through the resonator, which we can refer to as beam loops. Since each beam loop has a particular output pattern, it is convenient to refer to these patterns as modes of the resonator. Thus the modes and their periodicity are linked by the choice of resonator parameters.

4.3.3 M^2

Each transverse mode pattern has an associated M^2-value which is a measure of its size. Figure 45 shows the behavior of the M^2 parameter as a function of time (or equivalently, the number of round trips p) in a Porro prism resonator.

Initially, when the field is essentially random noise, the M^2 –value is high (> 10). Within a hundred round trips the value oscillates between 7.8 and 8.5, dropping to an oscillation between 7.0 and 7.2 by p = 6000. Further convergence is slow.

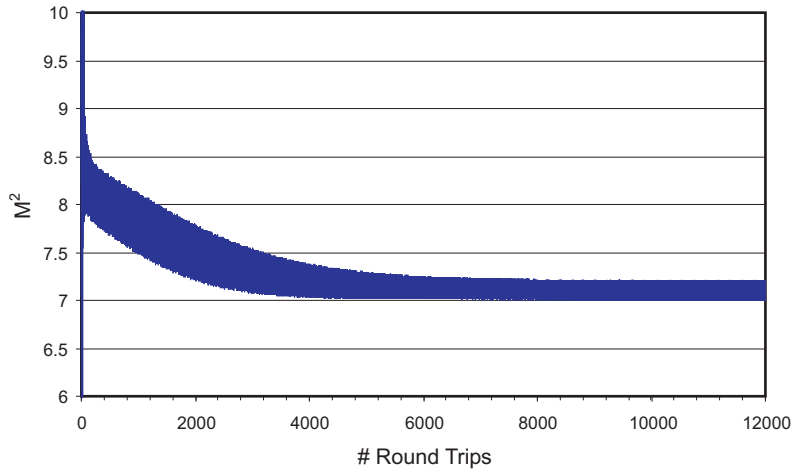

Figure 45 Temporal behaviour of M^2 in a Porro prism resonator, G = 0.9, N_F = 9.4.

4.3.4 Loss

Figure 46 shows high initial loss, settling to between 0.2 and 0.49 within a few hundred round trips, and to between 0.22 and 0.32 by p = 1000, after which convergence is slow. As for the M^2 parameter, the late slow convergence is indicative of a residual higher-order mode component.

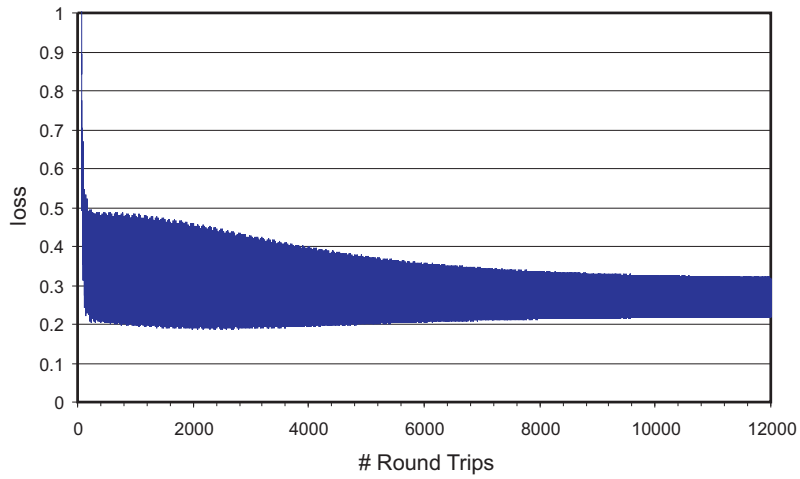

Figure 46 Temporal behaviour of loss in a Porro prism resonator, G = 0.9, N_F = 9.4.

An increase in round trip loss inside the laser cavity is also associated with an increase in the number of sub–divisions of the field N or, equivalently, in a decrease in the Porro angle.

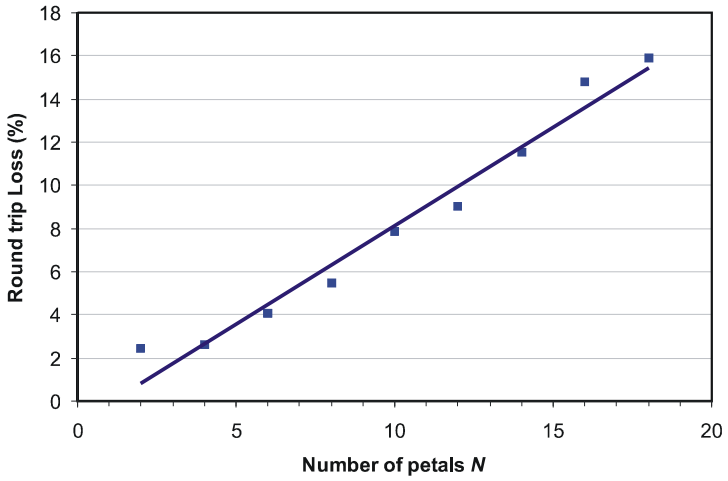

Figure 47 Plot of the round–trip loss as a function of the number of petals as predicted by the numerical model.

Figure 47 shows that for a fixed aperture radius *a*, the stabilized round–trip losses increase nearly linearly with the number of petals in the petal pattern over the region that one might reasonably expect to observe petals. This is due to the ever decreasing low loss area as the sub–divisions become closer together. This places restrictions on the allowed Porro angles that can actually be observed experimentally from such lasers.

The numerical model also correctly predicts the higher-order kaleidoscope beam modes to have higher losses than the lower-order petal–like mode. Because our numerical model allows the modes to oscillate indefinitely, loss selection ultimately results in the convergence of all starting fields to the petal–like patterns, as shown in Figure 48.

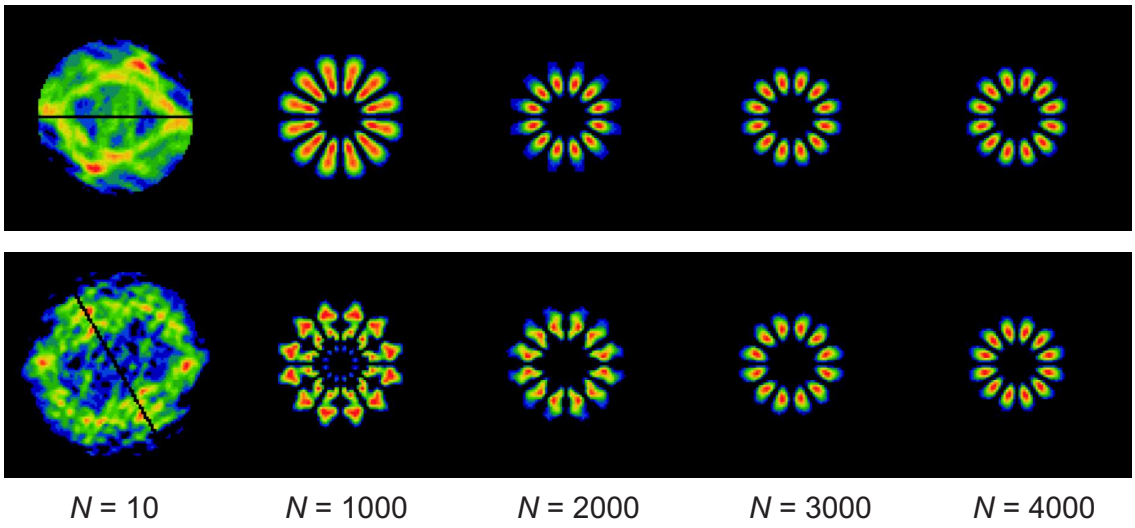

Figure 48 Development in time of the transverse modes in two Porro prism resonators (above) $\alpha = 60°$, $G = 0.9$, $N_F = 9.4$, and (below) $\alpha = 30°$, $G = 0.75$, $N_F = 13.5$.

Figure 48 shows examples of two Porro resonators with the mode pattern at $p = 10$, or just after switch-on when the mode is no more structured than apertured noise, and then in steps of 1000 round trips thereafter. In the series above ($\alpha = 60°$, $G = 0.9$, $N_F = 9.4$) the mode pattern soon appears petal-like, with variation mainly in the size of the mode pattern. In the series below ($\alpha = 30°$, $G = 0.75$, $N_F = 13.5$) the kaleidoscope modes are apparent in the region between approximately $p = 500$ to $p = 2000$ round trips. After $p = 2500$ the petal-pattern is apparent, with decreasing oscillation in the variation in the mode size.

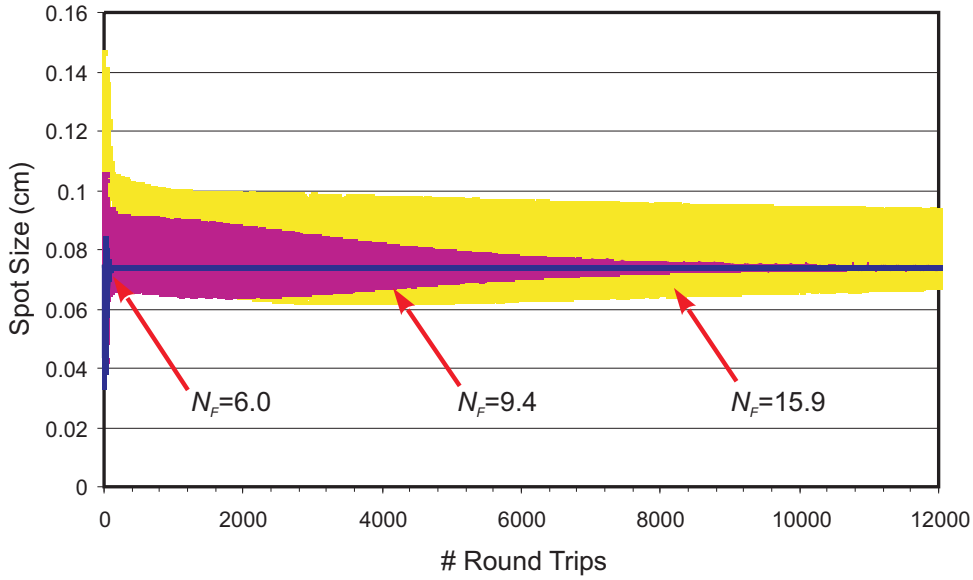

Figure 49 Comparison of the number of round trips required for mode convergence for increasing aperture sizes in a Porro prism resonator with α = 30°, G = 0.9.

Figure 49 shows that increasing the limiting aperture size a increases the number of round trips required for the beam to converge to a petal pattern. For N_F = 6.0 a few hundred round trips are required, for N_F = 9.4 about 7000 round trips are required, and for N_F = 15.9 the mode requires over 32000 round trips for convergence.

In the presence of gain and hence a limited build–up time, such a complete convergence would not necessarily take place, but partial convergence at least is expected, and would follow the behaviour of stable Fabry-Perot resonators (*Martinez et al.* 1997; *Encias-Sanz* 1999), and in this respect agrees with the prediction for Porro prism resonators by (*Chen et al.* 2006), that a slowly-opened Q-switch (and therefore longer pulse) will result in a lower-order mode beam.

4.4 Experimental verification

The Porro prism resonator investigated in this study is shown schematically in Figure 34, and was based on a flash lamp pumped Nd:YAG laser with passive Q–switching. The active medium was a 50 mm long Nd:YAG rod of radius 3 mm. Two Porro prisms at either end of the laser formed the resonator, replacing traditional mirrors. The stability of the resonators was determined by the two intra–cavity lenses near the prisms, but in our experiment no intracavity lenses were used, yielding a marginally stable resonator. The resonator was confined in the transverse direction by the clear aperture of the optical elements, such as lenses, prisms and gain

rod. The laser was pulsed using a Cr^{4+}:YAG passive Q–switch. A quarter wave plate together with a polarizing beamsplitter cube ensured variable output coupling from the laser by polarization control (by rotation of the waveplate or by rotation of the prisms).

The assembled laser used in our experiments is shown in Figure 50. The spatial intensity profile of the laser output was measured using a CCD camera (model COHU 4812). The temporal characteristics were detected with a silicon detector coupled to a 50 Ω impedance, and displayed on a two channel oscilloscope (Tektronic TDS 360).

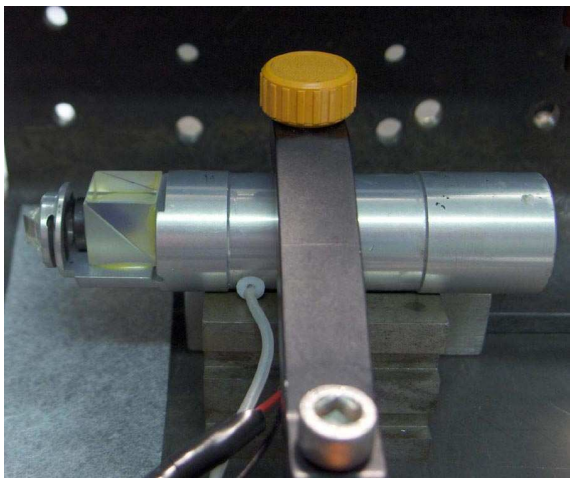

Figure 50 Photograph of assembled laser. The beamsplitter cube and one of the Porro prisms can be made out on the left of the assembly.

It is pertinent at this point to discuss the possibility of the experimental observation of these complex beam patterns. Their losses are such that in a mode competing environment they are distinct from the petal–like patterns for a time period in the order of 1–2 μs, which is comparable to the mode build–up time of a typical actively Q–switched Porro prism laser (see Figure 34). Thus while we cannot prove analytically that these complex beams are transverse modes of the resonator, their lifetime is such that it is very likely they are transverse modes, and there should be the possibility of observing them experimentally. There are however some limitations and technical challenges to such an experiment. It is likely that in a conventional linear standing-wave resonator some combination of these modes might appear, and with a time-averaged measurement a multi–mode pattern would be observed. We believe that we have observed this.

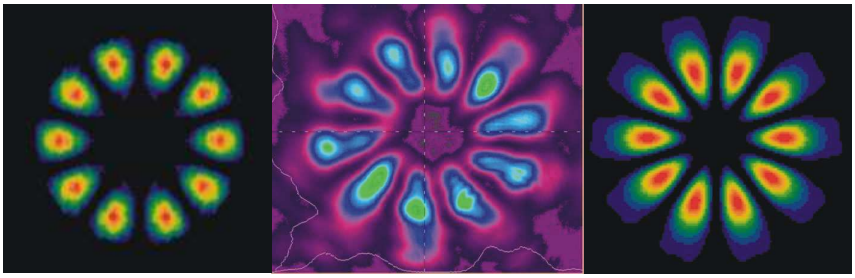

(a) (b) (c)

Figure 51 (a) Petal mode, (b) Experimental beam pattern, (c) Average of 5 cycles of higher-order modes at 1000 round trips.

Figure 51 (a) – (b) shows the comparison of a previously calculated petal pattern together with experimental verification (*Litvin, Burger & Forbes* 2007b). A time-averaged output in the time period of the complex modes is shown in Figure 51 (c). Two observations can be made: firstly, the resulting pattern is again similar to a petal–like pattern, despite no petal–like mode component in the sequence, and secondly, the pattern shows an elongation of the energy distribution, and a departure from the compact petals seen in Figure 51 (a). The latter is more consistent with the experimentally observed pattern, which was measured on a stable resonator with large apertures. This suggests (but does not prove) that the complex modes we predict do indeed exist, and are stable enough with low enough losses to be resonant in the cavity. In this sense they are likely to be viewed as higher-order modes of the resonator (*Burger & Forbes* 2008a; *Burger & Forbes* 2008b).

Further support for the validity of the model comes from Figure 52, which shows the similarity in time-averaged beam pattern predicted by the numerical model to that observed experimentally from a Porro prism resonator which is adjusted *away* from the azimuthal angles given in (4-12), where no petals are expected.

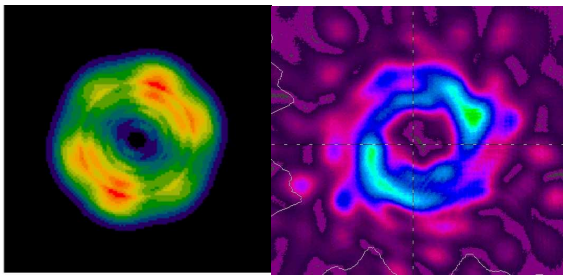

(a) (b)

Figure 52 (a) Result of numerical model time-average, (b) Experimental beam pattern, both from a Porro prism resonator in which the azimuthal angle α is tuned away from a petal pattern.

In order to measure distinct kaleidoscope modes it is possible that the approach of others in selecting multi–pass modes might be employed, together with knowledge of our particular field distributions, as predicted in this work. It has been shown that either preferentially increasing the gain (*Liu et al.* 2005) or the loss (*Bollig* 1997), or altering the phase (*Oron et al.* 1999a; *Oron et al.* 1999b; *Machavariani et al.* 2002; *Chu* 2007) for a particular path can force oscillation of a particular multi–pass beam mode. The challenge is to adapt such approaches to mode selection in Porro prism resonators.

4.5 Discussion

Using Eqs. (4-12) and (4-14), the finite sub–division of the field is predicted at angles α = 67.5° and α = 77.14°, with associated petal numbers of 10 and 14 respectively. No finite sub–division is expected at α = 79.0°. These cases are shown in Figure 53 (a) – (c) respectively, where the locations of the prism apexes are shown around the unit circle after several hundred rotations. In insets (a) and (b) the apexes are clearly repeating on themselves, resulting in a stable pattern, whereas in (c) the field does not result in any lossless regions because of the non–repeating apex positions. This latter situation prohibits the formation of a stable mode since all regions have high loss, while the former scenarios could potentially support lasing in the lower loss regions of the field.

The numerical model of the resonator confirms this (see Figure 53 (d) – (f)), showing a stable mode pattern for α = 67.5° and α = 77.14°, with the correct number of petals (10 and 14 respectively) as predicted by the theory. At α = 79.0° the output mode never stabilizes and results in a random field with high losses. Experimental results verify these findings, with petal patterns occurring when they should (α = 67.5° and α = 77.14°), and with the correct number of petals: 10 and 14 respectively (see Figure 53 (g) and (h)). At α = 79.0° no petal pattern was observed experimentally, in agreement with the theory and numerical model, with the camera image showing the time-averaged intensity from the laser. Thus the theoretical, numerical and experimental results are all in very good agreement.

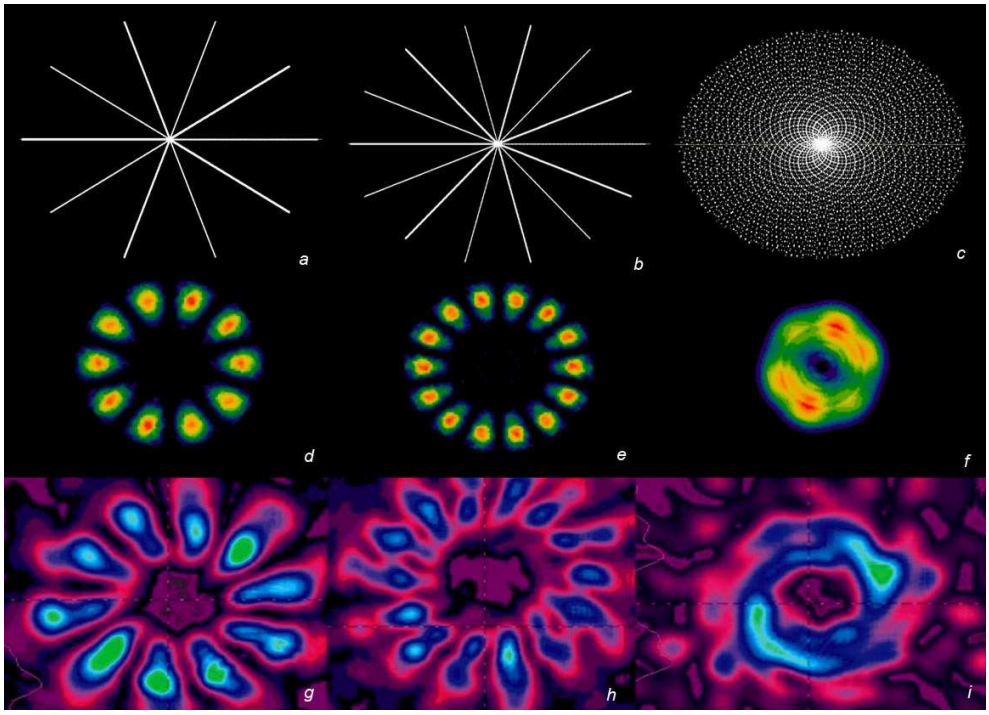

Figure 53 The analytical model depiction of finitely sub–divided fields in (a) and (b), and an infinitely sub–divided field in (c). Numerically this results in a pattern with (d) 10 petals, (e) 14 petals, (f) no petals. The corresponding experimentally observed output is shown in (g) – (i).

The angles α for which an output beam existed for the test laser were limited to between 63° and 87°. The absence of output below 63° was due to increased misalignment between the Porro prisms with decreasing angle away from 90° (the crossed case). It should be noted that this was a particular artefact of the resonator under study, and is not a general property of Porro resonators. The absence of output above 87° was due to two effects: (i) the output coupling method of the given cavity: at 90° (crossed Porro prisms) no output existed because cavity losses were 100% due to the polarization based output coupling method; and (ii) near 90° the number of predicted petals increases very rapidly with Porro angle. Since this reduces the available low loss area for the each petal, either no petals are observed due to the inherently high losses, or the close proximity of the petals leads to blurring due to diffraction.

The available experimental data at selected angles α is shown in Table 6, and is in excellent agreement with the theoretical and numerical predictions.

Table 6 Petal pattern observations: theory and experiment.

Experiment		**Theory**	
α	N	α	N
68° ± 0.5°	16	67.5000°	16
72° ± 0.5°	10	72.0000°	10
77° ± 0.5°	14	77.1429°	14
80° ± 0.5°	18	80.0000°	18

The complex higher-order modes revealed in the previous section show distinct similarities to so–called kaleidoscope modes (*McDonald et al.* 2000; *Bouchal* 2003; *Anguiano-Morales et al.* 2008). The similarities are visual, which we acknowledge to be subjective given that such modes have not been put on a firm mathematical basis, but more important similarities exist in the generating mechanisms.

Field distributions have been proposed which are a result of the coherent superposition of n cosine gratings, each rotated with angular increments of $\psi = \pi/n$ (*Bouchal* 2003). The similarity between this and a rotating loss on the field at angles $\alpha = \pi/n$ (Eq. (4-12) with $i = 1$) in Porro prism resonators probably accounts for the likeness in output modes.

Kaleidoscope modes have also been generated using crossed apertures to sub–divide the input field to an axicon (*Anguiano-Morales et al.* 2008). This type of obstruction pattern is identical to the final loss field observed in Porro prism resonators (see Figure 39). While such fields were previously created external to the laser cavity, we have shown that the fundamental property of field sub–division in Porro prisms can produce similar fields directly from the laser cavity.

The generating mechanisms in both (*Bouchal* 2003) and (*Anguiano-Morales et al.* 2008) have strong points of commonality with how intracavity Porro prisms are treated. However for completeness we must point out that the studies in question dealt with diffraction-free beams created by plane waves travelling on cones, with no obvious link to our resonator. Despite this the output modes bear very strong likeness in form, and perhaps also in properties.

The modes produced by the “kaleidoscope laser” are generated in a similar way to the Porro prism laser, in that in this case geometrically shaped apertures (triangle, rhombus, pentagon, hexagon and octagon) are placed inside the laser resonator (*McDonald et al.* 2000).

As for the Porro prism laser, the mode patterns produced show an increasing complexity with increasing Fresnel number.

The ubiquitous nature of Porro prism resonators makes a study of such modes necessary in its own right, but there also exists the possibility of using such complex modes to excite complex photonic crystal structures, and so further study is required.

4.6 Conclusions

Presented here is a new approach to modelling Porro prism resonators that combines geometrical and physical optical aspects. It shows that for specific prism angles these resonators must generate petal–like patterns or kaleidoscope patterns, and gives the generating equation for the prism angles at which this will happen. It has been shown that resonators produce kaleidoscope patterns as opposed to petal-like patterns only if they have sufficiently large intracavity apertures (or sufficiently high Fresnel numbers). These higher-order modes closely resemble recently reported kaleidoscope modes due to the fundamental property of field sub–division in Porro prism resonators. The appearance of first the petal mode and then increasingly complex kaleidoscope modes with increasing aperture size leads to the conclusion that the petal–like modes are the lowest-order modes of Porro prism resonators, while higher-order modes exist in the form of kaleidoscope–like fields. We also predict that the standard petal mode is only observable from stable Porro prism resonators, and indicate how the stability criterion (*G* parameter) impacts on the cyclical nature of the higher-order modes.

The petal results are confirmed experimentally on a test resonator; we believe it is possible to observe the kaleidoscope modes experimentally, but acknowledge that there are some technical challenges to overcome before doing so.

This work has implications on how such resonators are used in the field. Variable output coupling based on rotating the prisms is often employed, but as has been shown here, this will have a significant impact on the output mode from the laser, affecting laser beam propagation, far field laser intensity and laser brightness.

5. CONCLUSIONS AND FUTURE WORK

Porro prism resonator technology is considered to be mature (*Siegman* 2000) but nevertheless the petal-pattern beam which has long been observed from these resonators has never been explained in published literature. The aim of this dissertation was to develop a model of a Porro prism resonator to investigate the beam structure from these lasers.

Porro prism resonators have previously been treated as Fabry-Perot resonators with field inverting properties and polarization effects. Therefore a simple numerical model of a stable Fabry-Perot resonator was developed for two reasons. Firstly, the Fabry-Perot numerical model serves as a validation of the modelling techniques used by comparing the output of the model with analytical formulas from text-book theory. Secondly the model was used to investigate the properties of transverse mode formation in Fabry-Perot resonators to serve as a reference with which we could compare the differences in output beams from Fabry-Perot and Porro prism resonators. The temporal development of spot size, M^2 and loss were investigated and found to agree well with the understanding that shortly after switch on the beam consists of a rapidly cycling series of modes, and that given sufficient time (and the absence of the reseeding of higher-order modes) discrimination against the higher-order modes results in the convergence to the lowest-order or Gaussian beam.

Next we considered the fact that one of the major differences between Fabry-Perot resonators and Porro prism resonators was the inescapable presence of a narrow area of loss across the field, the result of the prism having two optical surfaces which meet at the apex. This provided a hint that the unique beam structures from Porro prism lasers could be caused by diffraction loss in this region. This led to a new approach to modelling Porro prism resonators that combines geometrical and physical optical aspects, and is based on tracking the apex “shadow” as the field passes from one Porro prism to the next inside a resonator, and we discovered that petal-like patterns will be generated only for certain discrete azimuthal prism angles. We have given the generating equation for the prism angles at which this will happen. This allowed the apex loss to be included in the numerical model as a rotating loss screen, which formed the basis of the Porro prism resonator model. The results are confirmed experimentally on a test resonator. This work has implications on how such resonators are used in the field. Variable output coupling based on rotating the prisms is often employed, but as has been shown here, this will have a significant impact on the output mode from the laser, affecting laser beam propagation, far field laser intensity and laser brightness.

Further, we have applied a previously-developed mathematical model of intracavity Porro prisms to stable and unstable Porro prism resonators with large intracavity apertures. We have shown that higher-order modes exist only if N_F is sufficiently large, and that these higher-order modes closely resemble recently-reported kaleidoscope modes due to the fundamental property of field sub–division in Porro prism resonators. The appearance of first the petal mode and then increasingly complex kaleidoscope modes with increasing aperture size leads to the conclusion that the petal–like modes are the lowest-order modes of Porro prism resonators, while higher-order modes exist in the form of kaleidoscope–like fields. We also predict that the standard petal mode is only observable from stable Porro prism resonators, and indicate how the stability criterion (*G* parameter) impacts on the cyclical nature of the higher-order modes. We believe it is possible to observe these modes experimentally, but acknowledge that there are some technical challenges to overcome before doing so.

Further work could include the decomposition of the predicted kaleidoscope modes into Hermite-Gaussian or Laguerre-Gaussian polynomials:

$$I(x) = \sum_{n=0}^{\infty} c_n G_n^2(x, v_0) \tag{5-1}$$

where c_n (n = 0, 1, …) are coefficients representing the power carried by the n-th order mode,

and $$G_n(x, v_0) = \left(\frac{2}{\pi v_0^2}\right)^{1/4} \frac{1}{\sqrt{2^n n!}} H_n\left(\frac{x\sqrt{2}}{v_0}\right) \exp\left(-\frac{x^2}{v_0^2}\right); \tag{5-2}$$

H_n is the n-th order Hermite polynomial, and v_0 is the spot size of the modes.

Either the method described in (*Borghi et al.* 2001) could be followed, in which the orthogonality and completeness of the Hermite polynomials are exploited to fit these polynomials to a given intensity distribution, or a 2-dimensional genetic algorithm could be written which would evaluate a fit of a set of Hermite-Gaussian polynomials against a given kaleidoscope mode and optimize the coefficients c_n of this set of polynomials to achieve a “best fit”.

It would be interesting to measure the polarization of the individual petals making up a beam experimentally and see whether it changes from one petal to the next as it does in the lobes of the fields of higher-order Laguerre-Gaussian beams (*Casperson* 1976).

It would also be extremely useful to investigate the far-field propagation of both petal and kaleidoscope beams (in other words the low- and higher-order modes), varying both the stability

parameter as well as the Fresnel number of the resonator under study, and also to investigate, using the analysis of (*Forbes et al.* 2008), whether the petals of a beam propagate as *N* separate quasi-Gaussian beams, or whether the beam propagates as a compound beam. The far-field beam pattern will determine the usefulness of these beams over a distance. If the petals propagate as separate quasi-Gaussians then they would be useful in the differential measurement of atmospheric turbulence.

If the beams combine over a distance to form a multimode beam structure then this would have implications as to the divergence and brightness of the beam, and to their usefulness in ranging applications.

6. REFERENCES

Afzal, R.S. (1994) Mars Observer Laser Altimeter: laser transmitter. Applied Optics 33, p. 3184-3188.

Agrawal, L., Bhardwaj A., Pal S. & Kumar A. (2007) Jones matrix formulation of a Porro prism laser resonator with waveplates: theoretical and experimental analysis. Applied Physics B: Lasers and Optics 89, p. 349-357.

Anan'ev, Y.A. (1973) Unstable prism resonators. *Quantum Electronics* 3, p. 58-59.

Anan'ev, Y.A, Kuprenyuk, V.I., Sergeev, V.V. & Sherstobitov, V.E. (1977) Investigation of the properties of an unstable resonator using a dihedral corner reflector in a continuous-flow cw CO2 laser. Quantum Electronics 7, p. 822-824.

Anguiano-Morales, M., Martínez, A., Iturbe-Castillo, D.M. & Chávez-Cerda, S. (2008) Different field distributions obtained with an axicon and an amplitude mask. Optics Communications 281, p. 401-407.

Arlt, J., Kuhn, R. & Dholakia, K. (2001) Spatial transformation of Laguerre-Gaussian laser modes. *Journal of Modern Optics* 48, p. 783-787.

Bahuguna, K.C., Sharma, P., Vasan, N.S. & Gaba, S.P. (2007) Laser Range Sensors. *Defence Science Journal* 57, p. 881-890.

Bekshaev, A.Y. (1999) Intensity Moments of a Laser Beam Formed by Superposition of Hermite-Gaussian Modes. *Fotoelektronika* 8, p. 22-25.

Belanger, P.A. (1991) Beam propagation and the ABCD ray matrices. *Optics Letters* 16, p. 196-198.

Blows, J.L., Forbes, G.W. & Dawes, J.M. (2000) Cavity modes in diode-array end-pumped planar lasers with aberrated thermal lenses. *Optics Communications* 186, p. 111-120.

Bollig, C. (1997) *Single-frequency diode-pumped solid state lasers*. PhD thesis, University of Southampton, UK.

Bollig, C., Clarkson, W.A., Hanna, D.C., Lovering, D.S., Jones, G.C.W. (1997) Single-frequency operation of a monolithic Nd:glass ring laser via the acousto-optic effect. *Optics Communications* 133, p. 221-224.

Borghi, R., Piquero, G. & Santarsiero, M. (2001) Use of biorthogonal functions for the modal decomposition of multimode beams. *Optics Communications* 194, p. 235-242.

Bouchal, Z. (2003) Nondiffracting Optical Beams: Physical Properties, Experiments, and Applications. *Czechoslovak Journal of Physics* 53, p. 537-578.

Brewster, D. (1819) *A Treatise on the Kaleidoscope*. Archibald Constable & Co., London.

Buchman, W. (1965) Laser Q-switch using a roof prism end reflector and electro-optical retarder. *IEEE Journal of Quantum Electronics* 1, p. 280-281.

Burger, L. & Forbes, A. (2007) A model of the transverse modes of stable and unstable porro-prism resonators using symmetry considerations. *Proceedings of SPIE* 6663, p. 666305-1 - 666305-8.

Burger, L. & Forbes, A. (2008a) Kaleidoscope modes in large aperture Porro prism resonators. *Optics Express* 16, p. 12707-12714.

Burger, L. & Forbes, A. (2008b) Porro prism lasers: a new perspective. *Proceedings of SPIE* 7070, p. 70700L-1.

Casperson, L.W. (1976) Phase compensation of laser beam modes. *Optical and Quantum Electronics* 8, p. 537-544.

Champagne, Y. & Bélanger, P.A. (1995) Method for measurement of realistic second-moment propagation parameters for nonideal laser beams. *Optical and Quantum Electronics* 27, p. 813-824.

Chapple, P.B. (1994) Beam waist and M^2 measurement using a finite slit. *Optical Engineering* 33, p. 2461-2466.

Checcacci, P.F., Consortini, A. & Scheggi, A. (1966) Modes, phase shifts, and losses of flat-roof open resonators. *Applied Optics* 5, p. 1567–1572.

Chen, J., Wang, P.J., Yau, H.F. & Chang, S.P. (1996) Energy extraction of Porro resonator in Pockels cell Q-switch operation. *Optical and Quantum Electronics* 28, p. 1453-1462.

Chen, J., Lin, J.T. & Mang, O.Y. (2006) Smaller Output Beam Divergence in the Slowly Opened Q-Switch Operation. *Optical Review* 13, p. 69-76.

Chu, S. (2007) A design of optical resonator for donut mode generation. *Proceedings of SPIE* 6663, p. 66630Q-1 - 66630Q-11.

Chun, M.K. & Teppo, E.A. (1976) Laser resonator-An electro-optically Q-switched Porro prism device. *Applied Optics* 15, p. 1942-1946.

Cole, T.D. (1998) NEAR Laser Rangefinder: A Tool for the Mapping and Topologic Study of Asteroid 433 Eros. *Johns Hopkins APL Technical Digest* 19, p. 142-157.

CVI (2009) Porro Prisms. *CVI Optical Components and Assemblies catalogue*. www.cvilaser.com/Common/PDFsNews/2006_Optical_Components_Catalog.pdf, p. 34.

di Francia, G.T. (1965) Flat-roof resonators. *Applied Optics* 4, p. 1267-1270.

Dudeja, J.P. (1989) Nd: YAG Laser-Pumped Raman-Shifted Methane Laser as an Eye-safe Laser Rangefinder. *Defence Science Journal* 39, p. 221-232.

Encinas-Sanz, F., Calderón, O.G., Gutiérrez-Castrejón, R. & Guerra, J.M. (1999) Measurement of the spatiotemporal dynamics of simple transverse patterns in a pulsed transversely excited atmospheric CO_2 laser. *Physical Review A* 59, p. 4764-4772.

Forbes, A., Burger, L. & Litvin, I.A. (2006) Modelling laser brightness from cross Porro prism resonators. *Proceedings of SPIE* 6290, p. 62900M-1.

Forbes, A., Ngcobo, S., Esser, D., Preussler, D. & Bollig, C. (2008) Laser beam propagation characteristics of incoherently added diode bars. *Proceedings of SPIE* 7062, p. 70621A-1.

Fox, A.G. & Li, T. (1961) Resonant Modes in a Maser Interferometer. *Bell System Technical Journal* 40, p. 453–488.

Fox, A.G. & Li, T. (1963) Modes in a maser interferometer with curved and tilted mirrors. *Proceedings of the IEEE* 51, p. 80-89.

Fox, A. & Li, T. (1968) Computation of optical resonator modes by the method of resonance excitation. *Quantum Electron* 4, p. 460-465.

Friedman, G. (2000) The light fantastic: Ted Maiman and the world's first laser. <http://spie.org/x13999.xml?highlight=x2416>

Gould, G. Jacobs, S., Rabinowitz, P., Shultz, T. (1962) Crossed Roof Prism Interferometer. *Applied Optics* 1, p. 533-534.

Gregor, E., Chen, T. & Bruesselbach, H.W. (1998) *Compact Diode-pumped Solid-state laser*. EP Patent 0,796,513.

Hanna, D.C., Sawyers, C.G. & Yuratich, M.A. (1981) Telescopic resonators for large-volume TEM_{00}-mode operation. *Optical and Quantum Electronics* 13, p. 493-507.

Hecht, E. (2001) *Optics.* Addison-Wesley, Reading MA.

Henriksson, M., Sjoqvist, L. & Uhrwing, T. (2005) Numerical simulation of a battlefield Nd:YAG laser. *Proceedings of SPIE* 5989, p. 59890I-1 - 59890I-10.

Henriksson, M. & Sjoeqvist, L. (2007) *Numerical Simulation of a Flashlamp Pumped Nd:YAG Laser*. FOI-R-1710-SE, Swedish Defence Research Agency, Linkoeping.

Hodgson, N. & Weber, H. (2005) *Laser Resonators and Beam Propagation*. Springer-Verlag, New York.

Ishizu, M. (2004) *Laser oscillator*. US Patent 6,816,533.

Joseph, P. (2007) Solid State Laser Developments at LASTEC. <http://frontierindia.net/solid-state-laser-developments-at-lastec>

Kimel, I. & Elias, L.R. (1993) Relations between Hermite and Laguerre Gaussian modes. *Quantum Electronics, IEEE Journal of* 29, p. 2562-2567.

Kogelnik, H. & Li, T. (1966) Laser beams and resonators. *Applied Optics* 5, p. 1550-1567.

Kuo, I. & Ko, T. (1984) Laser resonators of a mirror and corner cube reflector: Analysis by the imaging method. *Applied Optics* 23, p. 53–56.

Lawrence, G.N. (1987) Optical system analysis with physical optics codes. *Proceedings of SPIE* 766, p. 111-118.

Lawrence, G.N. (1991) Optical design with physical optics using GLAD. *Proceedings of SPIE* 1354, p. 126-135.

Lee, J.F. & Leung, C.Y. (1988) Beam pointing direction changes in a misaligned Porro prism resonator. *Applied Optics* 27, p. 2701–2707.

Lee, J.F. & Leung, C.Y. (1989) Method of calculating the alignment tolerance of a Porro prism resonator. *Applied Optics* 28, p. 3691-3697.

Lee, J.F. & Leung, C.Y. (1989) Lateral displacement of the mode axis in a misaligned Porro prism resonator. *Applied Optics* 28, p. 5278-5284.

Litvin, I.A., Burger, L. & Forbes, A. (2007a) Analysis of transverse field distributions in Porro prism resonators. *Proceedings of SPIE* 6346, p. 63462G-1 – 63462G-7.

Litvin, I.A., Burger, L. & Forbes, A. (2007b) Petal-like modes in Porro prism resonators. *Optics Express* 15, p. 14065-14077.

Liu, W., Huo, Y., Yin, X. & Zhao, D. (2005) Modes of Multi-End-Pumped Nonplanar Ring Laser. *IEEE Photonics Technology Letters* 17, p. 1776-1778.

Lu, B., Cai, B., Liao, Y., Xu, S. & Xin Z. (1989) Flowing air-water cooled slab Nd: glass laser. *Proceedings of SPIE* 1021, p. 175-180.

Lukac, M. (1991) Output energy characteristics of optimally pumped rotating mirror Q-switch lasers. *IEEE Journal of Quantum Electronics* 27, p. 2094-2097.

Lukš, A. (1976) On the moment problem in optics. *Czechoslovak Journal of Physics* 26, p. 1095-1101.

Lundstrom, E.A. (1983) *Waveplate for correcting thermally induced stress birefringence in solid state lasers*. US Patent 4,408,334.

Lundstrom, E.A. (1984) *Output coupler for laser resonator*. US Patent 4,461,009.

Machavariani, G., Davidson, N., Ishaaya, A.A., Friesem, A.A. & Hasman, E. (2002) Transformation of a high-order mode-intensity distribution to a nearly Gaussian beam. *Proceedings of SPIE* 5147, p. 271-275.

Mansfield, D.K., Jones, K., Johnson, L.C. & Semet, A. (1983) Theory of the rooftop resonator: resonant frequencies and eigenpolarizations. *Applied Optics* 22, p.662-665.

Martinez, C., Encinas-Sanz, F., Serna, J., Mejías, P.M. & Martínez-Herrero, R. (1997) On the parametric characterization of the transversal spatial structure of laser pulses. *Optics Communications* 139, p. 299-305.

McDonald, G.S., Karman, G.P., New, G.H.C. & Woerdman, J.P. (2000) Kaleidoscope laser. *Journal of the Optical Society of America B* 17, p. 524-529.

Nortier, F. (1981) *Investigation of a crossed Porro prism resonator employed in a Q-switched Nd:YAG laser*. MSc thesis, University of Natal, South Africa.

Oron, R. Danziger, Y., Davidson, N., Friesem, A.A. & Hasman, E. (1999a) Discontinuous phase elements for transverse mode selection in laser resonators. *Applied Physics Letters* 74, p. 1373-1375.

Oron, R. Danziger, Y., Davidson, N., Friesem, A.A. & Hasman, E. (1999b) Laser mode discrimination with intra-cavity spiral phase elements. *Optics Communications* 169, p. 115-121.

Padgett, M. Arlt, J., Simpson, N. & Allen, L. (1996) An experiment to observe the intensity and phase structure of Laguerre-Gaussian laser modes. *American Journal of Physics* 64, p. 77-82.

Pasqualetti, F. & Ronchi, L. (1973) Roof-mirror resonators. *Journal of the Optical Society of America* 65, p. 649-654.

Peck, E.R. (1962) Polarization properties of corner reflectors and cavities. *Journal of the Optical Society of America* 52, p. 253–257.

Podgaetskii, V.M. & Chernets, A.N. (1967) Using reflecting prisms in a solid-state laser with a kerr cell shutter. *Journal of Applied Spectroscopy* 6, p. 488-490.

Podgaetskii, V.M. (1969) Application of the Jones Method for Computation of the Electrooptical-Shutter Characteristics in a Laser with Porro Prisms as Reflectors. *Optics and Spectroscopy* 26, p. 153.

Preussler D. (2007). Private communication. National Laser Centre, CSIR, PO Box 395, Pretoria, South Africa.

Rapaport, A. & Bass, M. (2000) *Laser resonator design using optical ray tracing software*. SAND2000-2888J, Sandia National Labs., Albuquerque, NM.

Rapaport, A., Weichman, L., Brickeen, B., Green, S. & Bass, M. (2001) Laser resonator design using optical ray tracing software: comparisons with simple analytical models and experimental results. *IEEE Journal of Quantum Electronics* 37, p. 1401-1408.

Reed, E.D. (1997) *Prism folded laser cavity with controlled intractivity beam polarization*. US Patent 5,640,412.

Reeder, R.A. (1988) *Laser resonator*. US Patent 4,740,986.

Richards, J. (1982) *Laser Resonator*. Patent WO/1982/003503.

Richards, J. (1987) Birefringence compensation in polarization coupled lasers. *Applied Optics* 26, p. 2514–2517.

Ronchi, L. (1973) Low-loss modes and resonances in a quasi-90-roof mirror resonator. *Applied Optics* 12, p. 93-97.

Roundy, C.B. (2008) Current Technology of Laser Beam Profile Measurements, http://www.ophiropt.com/user_files/news/camera_based_systems_for_modern_laser_beam_diagnostics.pdf

See, B.A., Fueloep, K. & Seymour, R. (1980) *An Assessment of the Crossed Porro Prism Resonator*. ERL-0162-TM AR-002-041, Electronics Research Lab., Adelaide, Australia, p.1-16.

Severinsson, A.S. (1985) *Method of maintaining a predetermined beam direction in a laser pulse transmitter and an apparatus for carrying out the method*. US Patent 4,498,180.

Siegman, A.E. (1986) *Lasers*. University Science Books, USA.

Siegman, A.E. (1993) Defining, measuring, and optimizing laser beam quality. *Proceedings of SPIE* 2, p. 2-12.

Siegman, A.E. (1998) How to (maybe) measure laser beam quality. *DPSS Lasers: Application and Issues, MW Dowley, ed.* 17, p. 184-199.

Siegman, A.E. (2000) Laser Beams and Resonators: Beyond the 1960s. *IEEE Journal of Special Topics in Quantum Electronics* 6, p. 1389-1399.

Siegman, A.E. & Miller, H.Y. (1970) Unstable optical resonator loss calculations using the Prony method. *Applied Optics* 9, p. 2729-2736.

Singh, I., Kumar, A. & Nijhawan, O.P. (1995) Design of a high-power Nd: YAG Q-switched laser cavity. *Applied Optics* 34, p. 3349-3351 .

Smith, P.W. (1972) Mode selection in lasers. *Proceedings of the IEEE* 60, p. 422-440.

Stevens, H. (1963) Some congruence properties of the Hermite polynomials. *Archiv der Mathematik* 14, p. 391-398.

Steyl, J. (2007). Private communication, Carl Zeiss Optronics (Pty) Ltd., Nellmapius Drive, Irene 0046, South Africa.

Storm, M. (1992) Controlled retroreflection- A technique for understanding and eliminating parasitic lasing. *Optical Society of America, Journal, B: Optical Physics* 9, p. 1299-1304.

Sundvold, S.D., Morrelli, G.L., Brickeen, B.K., Powell, C.A. & Paiva, R.A. (1999) X1 UV laser trigger system. *Proceedings of SPIE* 3613, p. 56-64.

Tsai, C. & Lin, P. (2008) The determination of positions and orientations of a prism's surfaces based on image orientation change. *Applied Physics B: Lasers and Optics* 91, p. 105-114.

Virnik, Y.Z., Gerasimov, V.B., Sivakov, A.L. & Treivish, Y.M. (1987) Formation of fields in resonators with a composite mirror consisting of inverting elements. *Quantum Electronics* 17, p. 1040-1043.

Vtorova, V.E., Gorbachev, V.I. & Scheglov, V.A. (1991) Review of methods of calculating the field in optical cavities and choice of calculation method for free-flow chemical lasers. *Journal of Russian Laser Research* 12, p. 126-146.

Wang, L.Y. & Stephan, G. (1991) Transverse modes of an apertured laser. *Applied Optics* 30, p. 1899-1910.

Webb, C. & Jones, J. (2004) *Handbook of Laser Technology and Applications, Volume 1: Principles*. Institute of Physics Publishing, Bristol and Philadelphia.

Winker, D.M., Hunt, W.H. & Hostetler, C.A. (2004) Status and performance of the CALIOP lidar. *Proceedings of SPIE* 5575, p. 8-15.

Wright, D. Greve, P., Fleischer, J. & Austin, L. (1992) Laser beam width, divergence and beam propagation factor—an international standardization approach. *Optical and Quantum Electronics* 24, p. 993-1000.

Yanagisawa, T. & Hirano, Y. (2005) *Self-compensating laser resonator*. US Patent 6,901,102.

Yassin, G. & Lain, D.C. (1985) Rectangular flat-roof microwave resonator for molecular beam masers. *Journal of Physics D-Applied Physics* 18, p. 1979-1985.

Zhou, G. & Casperson, L. (1981) Modes of a laser resonator with a retroreflecting roof mirror. *Applied Optics* 20, p. 3542–3546.

7. APPENDIX

7.1 GLAD model of a symmetrical Fabry-Perot resonator

Cir-Mir Reson 03.inp

```
variab/dec/int step pass STOP
variables/declare/real L R1 Apertur Dfitxomega Dfityomega Dmsqx Dmsqy
variables/monitor/add L R1 Apertur step Dfitxomega Dfityomega Dmsqx
Dmsqy

write/on
array/set 1 256
fieldsize=0.3
L=10
R1= 52.3607
Apertur=0.08                                # 2w1= 0.0495055 2.5w1=
0.0618819 3w1= 0.0742582

nopass = 10000          #600 #200
set/density 128 128

macro/def reson/o
   pass = pass + 1 list                # increment pass counter
   step = step + 1                     # increment step number
   prop L/2                             # propagate 45 cm.
   macro/run diagnostix
   W1x=Dwx;
   mirror/sph 0 -R1                    # concave mirror of 50 cm
radius
   clap/c/n 0 Apertur #0.14                      # .14 cm. radius
aperture
   prop L                             # propagate 45 cm. along beam
   macro/run diagnostix
   W2x=Dwx;
   mirror/sph 0 R1                     # concave mirror of 50 cm
radius
   clap/c/n 0 Apertur #0.14                      # .14 cm. radius
aperture
   prop L/2
   energy                              # calculate energy in the beams
   variab/set energy1 1 energy
   loss = (1 - energy1)*100            # determine loss (%) before
normalising peak I=1

   pltflag=0
   if [step>99] then
     if [step<120] then
       pltflag=1
     endif
   endif
   if pltflag=1 then
     set/window/center-width 0.1 0.1
     title L=@L R1=@R1 at @step steps
     plot/watch circ_mode_R1=@R1_Ap=@Apertur_Step=@step.plt
```

```
     plot/bitmap/intensity/burnpattern 1 min=0
     plot/meta/wmf
     pause 2
     plot/plot_log/clear
     watch/close
     watch/start
   endif

  # Output data to text file
  write/disk/on 'Output-R=@R1_Ap=@Apertur.txt'/nooverwrite
  C
  Apertur=
  Dfitxomega=
  Dfityomega=
  Dmsqx=
  Dmsqy=

  energy/norm 1 1
  variab/set energy1 1 energy         # reset energy1 to 1

  loss=
  write/disk/off
macro/end

macro/def diagnostix/o
  fitmsquared/both/nocorrection 1       # Diagnostics of Beam #2
  variables/set Dfitxcent fitxcent      # X-beam center
  variables/set Dfitycent fitycent      # Y-beam center
  variables/set Dfitxomega fitxomega    # X-radius of equivalent
gaussian
  variables/set Dfityomega fityomega    # Y-radius of equivalent
gaussian
  variables/set Dfitxrad fitxrad       # X-transverse radius of equiv
gauss
  variables/set Dfityrad fityrad       # Y-transverse radius of equiv
gauss
  variables/set Dfitxsig fitxsig        # X-standard deviation
  variables/set Dfitysig fitysig        # Y-standard deviation
  variables/set Dfitxsigf fitxsigf      # X-standard deviation, freq
space
  variables/set Dfitysigf fitysigf      # Y-standard deviation, freq
space
  variables/set Dmsqx msqx              # M2 in the x-direction
  variables/set Dmsqy msqy              # M2 in the y-direction
  Dwx=2*Dfitxsig
  Dwy=2*Dfitysig
macro/end

nbeam 1                                # establish 2 beams
wavelength/set 1 1.064                 # set wavelengths
units/field 1 fieldsize

resonator/name reson
C ***** Eigen/Test *****
resonator/eigen/test 1

C ***** Eigen/Set *****
resonator/eigen/set 1                  # set beam 2 to eigen mode
```

```
clear 1 1                                # start with a plane wave in
beam 2
energy/norm 1 1
status/p
pass = 0                                 # initialize variables
step = 0                                 # for pass counters
gain/converge/set eps1=.001 npoints=5  # set convergence criterion to
                                         # .1 percent energy change
write/off

write/disk/on 'Output-R=@R1_Ap=@Apertur.txt'/overwrite
write/disk/off

reson/run nopass
write/on

title diffraction mode shape
plot/watch circ_mode_R1=@R1_Ap=@Apertur_diffr_mode.plt
plot/bitmap/intensity/burnpattern 1 min=0
plot/meta/wmf
```

7.2 Mathematica code - periodicity of a Fabry-Perot resonator

Mir Reson Eigen calcs ito g 03 assym.nb

Eigenequation analysis of Porro resonator

- Variables

```
Clear[m, Mmir, Δ0, θ0, λ1, λ2, v1, v2, β1, β2, L, R1, R2, g1, g2, periodicity, p]
R1 = ∞;
R2 = 1048;
L = 177.2;
```

- Set known variables

```
Δ0 = 1;
θ0 = 0;
```

- ABCD Matrix for a Mirror Resonator

```
mirror[R_] := {{1, 0}, {-2/R, 1}};
flatmirror := {{1, 0}, {0, 1}};
gap[d_] := {{1, d}, {0, 1}};

Mmir[R1_, R2_] := gap[L/2].mirror[R1].gap[L].mirror[R2].gap[L/2] // Simplify;
MatrixForm[Mmir[R1, R2]];
```

- Mirror Resonator Analysis

```
g1 = 1 - L/R1;
g2 = 1 - L/R2;
m = 1/2 (Mmir[R1, R2][[1, 1]] + Mmir[R1, R2][[2, 2]]) // Factor;
{evals, evecs} = Eigensystem[Mmir[R1, R2]];

λ1 = evals[[1]] // Simplify;
λ2 = evals[[2]] // Simplify;

v1 = evecs[[1]] // Simplify;
v2 = evecs[[2]] // Simplify;
```

- FInd coefficients

```
Clear[β1, β2];
PP0 = β1 v1 + β2 v2;
(* Δ0=P0[[1]] ; Θ0=P0[[2]] *)
sol = Solve[{Δ0 == PP0[[1]], Θ0 == PP0[[2]]}, {β1, β2}];
β1 = β1 /. sol[[1, 1]] // Simplify;
β2 = β2 /. sol[[1, 2]] // Simplify;
```

- Define Ray Propagation function

```
PP[p_] := β1 λ1^p v1 + β2 λ2^p v2;
PP[0] // Simplify;
```

- Option 1: Given R, find periodicity P

```
θ = N[ArcCos[m]];
periodicity = 2 π / θ;
```

- Output

```
Print["Mmir = ", MatrixForm[Mmir[R1, R2]]]
Print["L    = ", L]
Print["R1   = ", R1]
Print["R2   = ", R2]
Print["g1   = ", g1]
Print["g2   = ", g2]
Print["m    = ", m]
Print["λ1   = ", λ1]
Print["λ2   = ", λ2]
Print["v1   = ", v1]
Print["v2   = ", v2]
Print["β1   = ", β1]
Print["β2   = ", β2]
Print["PP[0] = ", PP[0]]
Print["PP[p] = ", MatrixForm[PP[p]]]
Print["m    = ", m]
Print["θ    = ", N[θ]]
Print["P    = ", N[periodicity]]

Show[
 Graphics[Plot[{PP[p][[1]]}, {p, 0, 25},
   PlotStyle→{Blue, Thick},
   PlotRange→1.13,
   Frame→True,
   FrameStyle→Directive[Thick, 12],
   FrameLabel→{"# round trips p", "y"},
   Ticks→{None, None},
   LabelStyle→{12, FontFamily→"Arial"},
   GridLines→{(*x*){},
     {(*y*){-1.0, LightGray}, {-0.5, LightGray}, {0.5, LightGray}, {1.0, LightGray}}}]]
]

Export[
 "D:\Data\PROJECT\NLC PAPERS & TALKS\MSc Thesis - Porro Project\Graphics\periodicity.wmf",
 %]
```

7.3 Mathematica code to plot the stability of a Porro prism resonator

Resonator Matrix Model 02.nb

Comparison of Ray Transfer Matrixes for Mirror - and Lens - Resonators

- Ray Transfer Matrix elements

```
lens[f_] := {{1, 0}, {-1/f, 1}};
mirror[R_] := {{1, 0}, {-2/R, 1}};
gap[d_] := {{1, d}, {0, 1}};
```

Mirror

```
Clear[R1, R2, f1, f2, L];
ABCDmir[R1_, R2_] := gap[d1].mirror[R1].gap[L].
   mirror[R2].gap[d2].gap[d2].mirror[R2].gap[L].mirror[R1].gap[d1];
MatrixForm[Simplify[ABCDmir[R1, R2]]]
```

```
R1 = 2 f1; R2 = 2 f2;
MatrixForm[Simplify[ABCDmir[R1, R2]]]
```

```
StabilityFnmir[f1_, f2_] :=
  1/2 ((Extract[ABCDmir[f1, f2], {1, 1}]) + (Extract[ABCDmir[f1, f2], {2, 2}]));
StableZonemir[f1_, f2_] := If[-1 < StabilityFnmir[f1, f2] < 1, 1, 0];
```

- Graphics - Mirror

```
d1 = 0; d2 = 0;
L = 10 ;
Show[
 Graphics[
  ContourPlot[StabilityFnmir[R1, R2], {R1, -10, 30}, {R2, -10, 30},
   ContourLabels→ Automatic, PlotPoints→ 100, Contours→ 5, PlotRange→ {-1, 1},
   Frame→ True,
   FrameStyle→ Directive[Thick],
   LabelStyle→ {18, FontFamily→ "Arial"},
   FrameLabel→ {"f1", "f2"},
   GridLines→
    {
     (*x*){-20.0, -10, 0, 10, 20},
     (*y*){-20.0, -10, 0, 10, 20}
    }, GridLinesStyle→ Directive[LightGray]

  ]
 ]
]

Export["D:\Data\PROJECT\NLC PAPERS & TALKS\MSc
   Thesis - Porro Project\Graphics\StabilityMir 10_0_0.wmf", %]
```

Lens

```
Clear[R1, R2, f1, f2, L];
ABCDlens[f1_, f2_] :=
  gap[d1].lens[f1].gap[L].lens[f2].gap[d2].gap[d2].lens[f2].gap[L].lens[f1].gap[d1];
MatrixForm[Simplify[ABCDlens[f1, f2]]]

StabilityFnlens[f1_, f2_] :=
  1/2 ((Extract[ABCDlens[f1, f2], {1, 1}]) + (Extract[ABCDlens[f1, f2], {2, 2}]));
StableZonelens[f1_, f2_] := If[-1 < StabilityFnlens[f1, f2] < 1, 1, 0];

d1 = 0;
d2 = 0;

L = 10;
ABCDlens[15, 15]
StabilityFnlens[15, 15]
StableZonelens[15, 15]
(*Simplify[ABCD[f1,f2]];*)
```

- **Graphics - Lens**

```
d1 = 0; d2 = 0;
L = 10 ;
Show[
 Graphics[
  ContourPlot[StabilityFnlens[f1, f2], {f1, -10, 30}, {f2, -10, 30}, (*ContourStyle→None,*)
   ContourLabels→ Automatic, PlotPoints→ 100, Contours→ 5, PlotRange→ {-1, 1},
   Frame→ True,
   FrameStyle→ Directive[Thick],
   LabelStyle→ {18, FontFamily→ "Arial"},
   (* ContourLabels→Directive[10,"Arial"], *)
   FrameLabel→ {"f1", "f2"},
   GridLines→
    {
     (*x*){-20.0, -10, 0, 10, 20},
     (*y*){-20.0, -10, 0, 10, 20}
    }, GridLinesStyle→ Directive[LightGray]

  ]
 ]
]

Export["D:\Data\PROJECT\NLC PAPERS & TALKS\MSc
   Thesis - Porro Project\Graphics\StabilityLens 10_0_0.wmf", %]



d1 = 2; d2 = 2;
L = 10 ;
Show[
 Graphics[
  ContourPlot[StabilityFnlens[f1, f2], {f1, -10, 30},
   {f2, -10, 30}, (*ContourStyle→None,*)ContourLabels→ Automatic,
   PlotPoints→ 100, Contours→ 5, PlotRange→ {-1, 1},
   Frame→ True,
   FrameStyle→ Directive[Thick],
   LabelStyle→ {18, FontFamily→ "Arial"},
   (* ContourLabels→{10,FontFamily→"Arial"}, *)
   FrameLabel→ {"f1", "f2"},
   GridLines→
    {
     (*x*){-20.0, -10, 0, 10, 20},
     (*y*){-20.0, -10, 0, 10, 20}
    }, GridLinesStyle→ Directive[LightGray]
  ],
  Graphics[{Red, PointSize[Large], Point[{{5, 5}, {9, 9}, {10, 10},
      {20, 20}, {40, 40}, {60, 60}, {100, 100}, {-100, -100}, {-50, -50}}]}]
 ]
]

Export["D:\Data\PROJECT\NLC PAPERS & TALKS\MSc
   Thesis - Porro Project\Graphics\StabilityLens 10_2_2.wmf", %]
```

7.4 GLAD code – Porro prism resonator

```
c##
write/screen/off

variab/dec/int step pass f1 f2 totalsteps arraysize pass plotcount
ffNoSteps ffstepcount
variab/dec/real angle ResonLength Apertur
variab/dec/real Dfitxcent Dfitycent Dfitxomega Dfityomega Dfitxrad
Dfityrad Dfitxsig Dfitysig Dfitxsigf Dfitysigf Dfitysig Dmsqx Dmsqy
DdelThetax DdelThetay Dwx Dwy loss
variables/monitor/show
variables/monitor/add angle step totalsteps f1 f2 Apertur Dwx Dwy
Dmsqx Dmsqy loss

# Invariable
arraysize = 256
fieldsize = 0.4
totalsteps = 2000
WaveL = 1.064                              # microns
prism_lens_dist1 = 0
prism_lens_dist2 = 0
inter_lens_dist = 10
ResonLength = prism_lens_dist1 + prism_lens_dist2 + inter_lens_dist
f=20                                       # Far-field lens, cm
#ApStep=0.005                              # set in ResStep

# Variable
f1 = 4*ResonLength                    # set in ResStep
f2 = 4*ResonLength                    # set in ResStep
#InitApertur = 0.04
# Starting Apertur, reset in ResLoop, incr. with 0.002 each loop
Apertur=0.16
ObsWidth = 0.002
angle=30.0

NoCycle = 14
avg_go = totalsteps - 5*NoCycle

# System
plotcount = 1000
set/density 128 128                        # NB This is the largest
setting
                                           # that works for wmf
histpltx=0.12
maxIplt=1



# -------------------------------------------------------

macro/def plot_history/o
   copy/c 1 2
   copy/row 2 3 1 step                   # copy X-section
macro/end

# -------------------------------------------------------
```

```
macro/def reson/o
   step = step + 1 list                          # increment step
number
   step1000=1000+step
   pass = pass + 1 list                          # increment pass
counter
   prop prism_lens_dist1                         # prism to cv lens
   lens/sph/element 1 f1                         # ideal cv (+) lens #2
   clap/cir/no 1 Apertur
   prop inter_lens_dist                          # to cx lens
   clap/cir/no 1 Apertur
   lens/sph/element 1 f2                         # - # ideal cx (-)
lens #1
   prop prism_lens_dist2                         # to prism
   obs/rec 1 1 ObsWidth 0 0 90-step*2*angle      # rotating of obs
mirror/flat 1

   prop prism_lens_dist2                         # to lens
   lens/sph/element 1 f2                         # ideal cx lens #1
   clap/cir/no 1 Apertur
   prop inter_lens_dist                          # to rod
   clap/cir/no 1 Apertur
   lens/sph/element 1 f1                         # ideal cv lens #2
   prop prism_lens_dist1                         # to prism
   obs/rec 1 1 ObsWidth 0 0 -90+angle+step*2*angle
   mirror/flat 1

   pass = pass + 1 list                          # increment pass
counter

   variab/set energy1 1 energy         # energy1 is energy after round
trip
   loss = (1 - energy1)*100            # determine loss (%) before
normalising peak I=1

   peak/norm 1
   term1=step/plotcount
   term2=floor(step/plotcount)

   if step > avg_go then
   #if [abs(term1-term2)<0.0201] then     # Select 1st 20/1000
   ##if step > totalsteps-100 then        # Select last 100
     set/window/center-width Apertur
     title L=@ResonLength f1=@f1 f2=@f2 at @step steps
     plot/watch
AP_NFmode_@angle_deg_f1=@f1_f2=@f2_Ap=@Apertur_Step=@step1000.plt
     plot/bitmap/intensity/burnpattern 1 max=maxIplt 0
     plot/meta/wmf
     pause 2
     plot/plot_log/clear
     watch/close
     watch/start
   endif

   macro/run diagnostix

  # Output data to text file
```

```
  write/disk/on
'AP_dev_data_@angle_deg_f1=@f1_f2=@f2_Ap=@Apertur.txt'/nooverwrite
  C
  Apertur=
  Dfitxomega=
  Dfityomega=
  Dmsqx=
  Dmsqy=

   udata/set step pass loss            # store loss (%)
   energy/norm 1 1
   variab/set energy1 1 energy         # reset energy1 to 1

  loss=
  write/disk/off

  if step > avg_go then
    add/incoherent 4 1
  endif
macro/end

# -------------------------------------------------------

macro/def ApLoop
  pass = 0                             # initialize variables
  step = 0                             # for pass counters
  resonator/name reson
  resonator/eigen/test 1
  resonator/eigen/set 1                # set beam 2 to eigen mode
  clear 1 1                            # start with a plane wave in
beam 1
  #noise 1 1                           # start with a plane wave in
beam 1
  noise/deltacorrelated 1 .1
  energy/norm 1 1

  plot/plot_log/clear

  reson/run totalsteps-1

  title Loss per pass
  plot/watch
AP_loss_@angle_deg_f1=@f1_f2=@f2_Ap=@Apertur_Step=@step.plt
  plot/udata 1 left=10 right=totalsteps min=0 max=5
  plot/meta/wmf

  # Plot Beam Average
  title Beam Tail Average
  set/window/center-width .2 .2
  plot/watch AP_NFmode_@angle_deg_f1=@f1_f2=@f2_Ap=@Apertur_avg.plt
  plot/bitmap/intensity 4 # 1 0
  plot/meta/wmf

  # Lens & propagate
  lens/sph/element 1 f
  prop f
  peak/norm 1
  title FF Beam Pattern
  set/window/center-width .2 .2
```

```
  plot/watch
AP_FFmode_@angle_deg_f1=@f1_f2=@f2_Ap=@Apertur_Step=@step.plt
  plot/bitmap/intensity/burnpattern 1
  plot/meta/wmf

  watch/close
  watch/start

#  Apertur=Apertur+ApStep
macro/end

# ------------------------------------------------------

macro/def diagnostix/o
  fitmsquared/both/nocorrection 1       # Diagnostics of Beam #1
  variables/set Dfitxcent fitxcent      # X-beam center
  variables/set Dfitycent fitycent      # Y-beam center
  variables/set Dfitxomega fitxomega    # X-radius of equivalent
gaussian
  variables/set Dfityomega fityomega    # Y-radius of equivalent
gaussian
  variables/set Dfitxrad fitxrad        # X-transverse radius
  variables/set Dfityrad fityrad        # Y-transverse radius
  variables/set Dfitxsig fitxsig        # X-standard deviation
  variables/set Dfitysig fitysig        # Y-standard deviation
  variables/set Dfitxsigf fitxsigf      # X-standard deviation, freq
space
  variables/set Dfitysigf fitysigf      # Y-standard deviation, freq
space
  variables/set Dmsqx msqx              # M2 in the x-direction
  variables/set Dmsqy msqy              # M2 in the y-direction
  Dwx=2*Dfitxsig
  Dwy=2*Dfitysig
macro/end

# ------------------------------------------------------

#  write/screen/off
  nbeam 4                                  # establish 1 beam
  array/set 1 arraysize
  #array/set 2 arraysize 1 data
  #array/set 3 arraysize totalsteps data
  array/set 4 arraysize arraysize data                  # avg

  units/field 0 fieldsize
  variab/set Units 1 units
  units/s 2 Units
  units/s 3 Units 1
  units/s 4 Units

  wavelength/set 1 WaveL                    # set wavelengths

  write/disk/on
'AP_dev_data_@angle_deg_f1=@f1_f2=@f2_Ap=@Apertur.txt'/overwrite
  write/disk/off
  macro/run ApLoop/1
```

7.5 Verification of GLAD beam size calculations

7.5.1 Generate and save GLAD beam data

```
c## outfile

variab/dec/int n m arraysize

arraysize=1024  #512
fieldsize = 1
wavelength/set 1 1.064
set/density 128 128                          # NB This is the largest
setting that works for wmf   #256 256                         # 512 512

w=0.20
n=2
m=1

# ------------------------------------------------------

macro/def writebeam
  peak/norm 1 1
  #outfile/intensity 'I_beam@n@mh.csv'/noheader/comma 1
  outfile/intensity
'I_H@n@m_fieldsize_@fieldsize_ArraySize_@arraysize.csv'/noheader/comma
1
  #outfile/phase 'P_beam@n@mh.csv'/noheader/comma 1

  set/window/center-width fieldsize/2 fieldsize/2
  title "test infile, outfile"
  plot/w I_H@n@m_fieldsize_@fieldsize_ArraySize_@arraysize.plt
  plot/bitmap/intensity 1 1 0

  fitgeo/msquared 1
  variables/set Ffitxcent 1 fitxcent
  variables/set Ffitycent 1 fitycent
  variables/set Ffitxomega 1 fitxomega
  variables/set Ffityomega 1 fityomega
  variables/set Ffitxrad 1 fitxrad
  variables/set Ffityrad 1 fityrad
  variables/set Ffitxsig 1 fitxsig
  variables/set Ffitysig 1 fitysig
  variables/set Ffitxsigf 1 fitxsigf
  variables/set Ffitysigf 1 fitysigf
  variables/set Fmsqx 1 msqx
  variables/set Fmsqy 1 msq
  C
  C FITGEO/MSQUARED
  C
  write/disk/on
'I_H@n@m_fieldsize_@fieldsize_ArraySize_@arraysize.txt'/nooverwrite
  C
  Ffitxcent=
  Ffitycent=
  Ffitxomega=
  Ffityomega=
  C
```

```
  C
  write/disk/off
macro/end

# ------------------------------------------------------

nbeam 1
array/set 1 arraysize
units/field 1 fieldsize/2 fieldsize/2

#gaussian/cir 1 1 w
hermite 1 1 w w n m

macro/run writebeam
```

7.5.2 Read beam and calculate spot size in Mathematica for comparison

GLAD beam centroid and size 02.nb

This file reads the csv output of a beam from a GLAD program, and calculates the:

- centroid

- beam radius (omega)

eg.From "AP model 03.... .inp"

```
fileno = 1;
(* select appropriate number here according to file you want to analyse *)
filename = fileset[[fileno]];
Imatrix = Import[filename, "csv"];
MatrixPlot[Imatrix, ColorFunction → "Rainbow"(*"CMYKColors"*) ]
Export["I_H00_fieldsize_1.000_ArraySize_1024_MM.wmf", %]
Imatrix = Transpose[Imatrix];
{n, m} = Dimensions[Imatrix];

field = 1;                    (* 1; *)
xx[i_] := field (i - 1)/n - 1/2
yy[j_] := field (j - 1)/m - 1/2


P_H = (Sum_{i=1}^{n} Sum_{j=1}^{m} Imatrix[[i, j]]);
{Centrx, Centry} = {(Sum_{i=1}^{n} Sum_{j=1}^{m} xx[i] Imatrix[[i, j]])/P_H, (Sum_{i=1}^{n} Sum_{j=1}^{m} yy[j] Imatrix[[i, j]])/P_H};
{Sigx, Sigy} = {Sqrt[(Sum_{i=1}^{n} Sum_{j=1}^{m} (xx[i] - Centrx)^2 Imatrix[[i, j]])/P_H],
  Sqrt[(Sum_{i=1}^{n} Sum_{j=1}^{m} (yy[j] - Centry)^2 Imatrix[[i, j]])/P_H]};
{Omegax, Omegay} = {2 Sigx, 2 Sigy};

Print["File :  ", filename]
Print["Centroid(x,y) = ", Centrx, ",  ", Centry]
(* Print["Sigma(x,y)    = ",Sigx,",  ",Sigy]  *)
Print["Omega(x,y)    = ", Omegax, ",  ", Omegay]
```

7.6 Mathematica code - periodicity of a Porro prism resonator

- **Variables**

```
Clear[m, Mlens, Δ0, θ0, λ1, λ2, v1, v2, β1, β2, L, f, f1, f2, g, p]
```

- **ABCD Matrix for a Lens Resonator**

```
lens[f_] := {{1, 0}, {-1/f, 1}};
mirror[R_] := {{1, 0}, {-2/R, 1}};
flatmirror := {{1, 0}, {0, 1}};
gap[d_] := {{1, d}, {0, 1}};
Mlens[f1_, f2_] := gap[L/2].lens[f1].gap[d1].flatmirror.gap[d1].lens[f1].
   gap[L].lens[f2].gap[d2].flatmirror.gap[d2].lens[f2].gap[L/2] // Simplify
MatrixForm[Mlens[f1, f2]];
```

- **Use simplified case**

```
d1 = d2 = d;
f1 = f2 = f;
```

- **Lens Resonator Analysis**

```
m = 1/2 (Mlens[f1, f2][[1, 1]] + Mlens[f1, f2][[2, 2]]) // Factor;
{evals, evecs} = Eigensystem[Mlens[f1, f2]];

λ1 = evals[[1]] // Simplify;
λ2 = evals[[2]] // Simplify;

v1 = evecs[[1]] // Simplify;
v2 = evecs[[2]] // Simplify;
```

- **FInd coefficients**

```
Clear[β1, β2]
PP0 = β1 v1 + β2 v2;
(* Δ0=P0[[1]] ; θ0=P0[[2]] *)
sol = Solve[{Δ0 == PP0[[1]], θ0 == PP0[[2]]}, {β1, β2}];
β1 = β1 /. sol[[1, 1]] // Simplify;
β2 = β2 /. sol[[1, 2]] // Simplify;
```

- **Define Ray Propagation function**

```
PP[p_] := β1 λ1^p v1 + β2 λ2^p v2
PP[0] // Simplify;
MatrixForm[PP[p]] // Simplify;
```

- **Set known variables**

```
Δ0 = 1;
θ0 = 0;
d = 2;
L = 10;
```

- **Option 1: Given f, find periodicity P (d1=d2=0 case only)**

```
f = 100;
g = 1 - L/f;
m = 2 g^2 - 1;
θ = N[ArcCos[m]];
periodicity = 2 π/θ;
```

- **Option 2: Given periodicity P, find f (d1=d2=0 case only)**

```
periodicity = 8;
θ = 2 π/periodicity;
m = Cos[θ];
g = N[Sqrt[(m + 1)/2]];      (* g=-Sqrt[(m+1)/2] *)
f = N[L/(1 - g)];
```

- **Output**

```
Print["--  Eigen Output for Lens Resonator  --"]
Print["Mlens = ", MatrixForm[Mlens[f1, f2]], Bold]
Print["PP[0] = ", PP[0]]
Print["PP[p] = ", MatrixForm[PP[p]]]

Print["d1    = ", d1]
Print["d2    = ", d2]
Print["L     = ", L]
Print["f1    = ", f1]
Print["f2    = ", f2]

Print["λ1    = ", λ1]
Print["λ2    = ", λ2]
Print["v1    = ", v1]
Print["v2    = ", v2]
Print["β1    = ", β1]
Print["β2    = ", β2]


Print["f     = ", f]
Print["g     = ", g]
Print["m     = ", m]
Print["θ     = ", θ]
Print["P     = ", periodicity]

Show[
 Graphics[Plot[{PP[p][[1]]}, {p, 0, 10},
   PlotStyle→ {Blue, Thick},
   PlotRange→ 1.13,
   Frame→ True,
   FrameStyle→ Directive[Thick, 12],
   FrameLabel→ {"# round trips p", "y"},
   Ticks→ {None, None},
   LabelStyle→ {12, FontFamily→ "Arial"},
   GridLines→ {(*x*){},
     {(*y*){-1.0, LightGray}, {-0.5, LightGray}, {0.5, LightGray}, {1.0, LightGray}}}]],

 Graphics[{PointSize[0.03],
   Blue, Point[{θ0, Δ0}], Point[{0., 1}], Point[{periodicity, 1}], Point[{2 periodicity, 1}]}
 ]]

Export["D:\Data\PROJECT\NLC PAPERS &
   TALKS\MSc Thesis - Porro Project\Graphics\periodicity_P=8.wmf", %]
```